# Molecular architecture of meiotic multiprotein complexes

**Dissertation**

zur Erlangung des naturwissenschaftlichen Doktorgrades der

Julius-Maximilians-Universität Würzburg

vorgelegt von

**Marie-Christin Spindler**

geboren in Lüdenscheid

Würzburg, 2020

Eingereicht am: ……..……..

**Mitglieder der Promotionskommission:**

Vorsitzender: ……..

Erstgutachter: Prof. Dr. Ricardo Benavente

Zweitgutachter: Prof. Dr. Markus Sauer

Tag des Promotionskolloquiums: ……..…

Doktorurkunde ausgehändigt am: …….

# Molecular architecture of meiotic multiprotein complexes

Dissertation
zur Erlangung des naturwissenschaftlichen
Doktorgrades
der Julius-Maximilians-Universität Würzburg

vorgelegt von

**Marie-Christin Spindler**

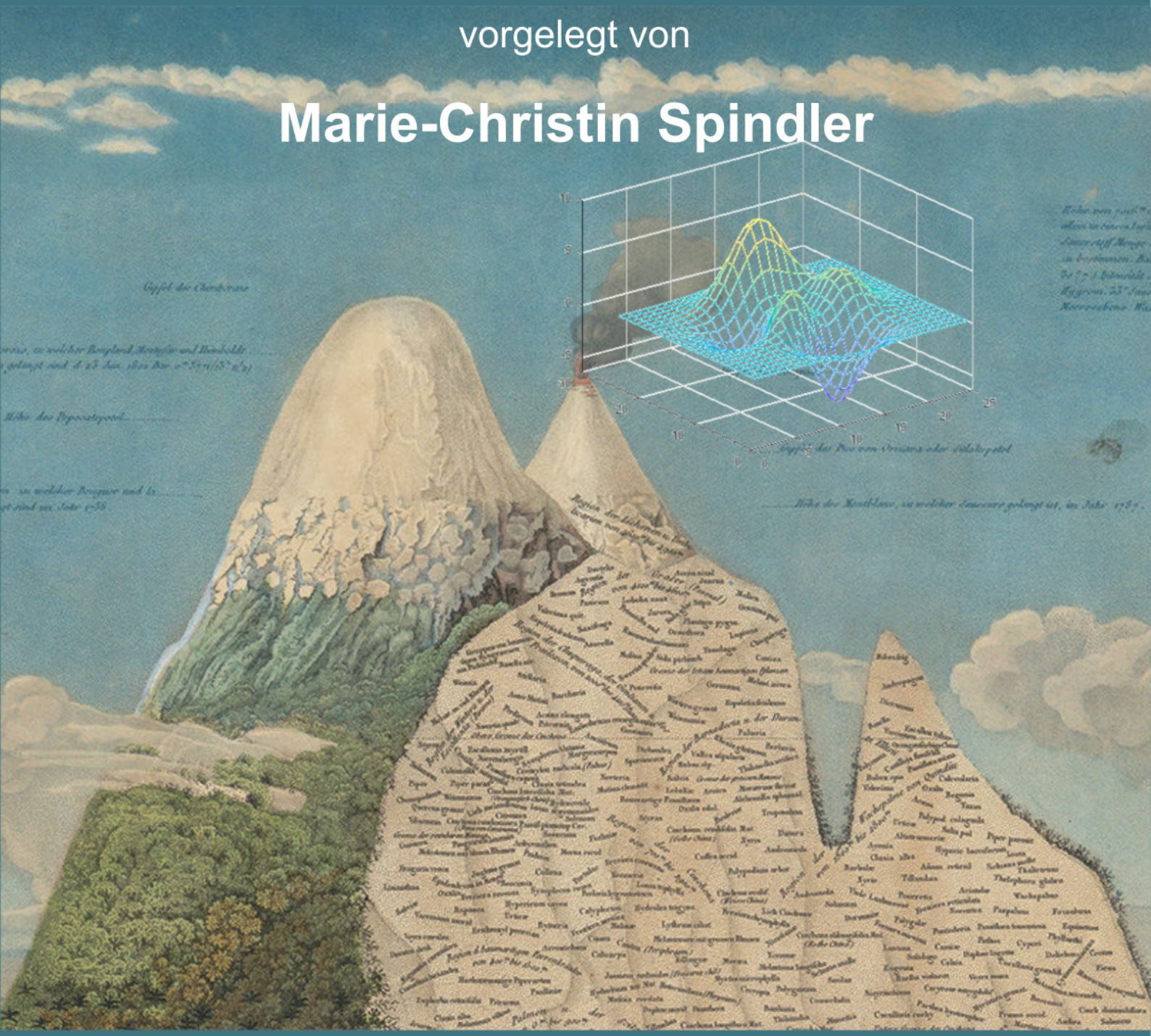

Würzburg 2020

*Illustrated cover page: Alexander von Humboldt's 1807 Tableau Physique mapped vegetation onto fanciful versions of the volcanoes Chimborazo and Cotopaxi. DESIGNED BY A. VON HUMBOLDT/DRAWN BY SCHÖNBERGER AND TURPIN/ENGRAVED BY BOUQUET/TYPEFACE BY L. AUBERT/PRINTED BY LANGLOIS/WIKIMEDIA COMMONS.*

# Summary

Sexually reproducing organisms depend on meiosis for the generation of haploid, genetically diverse gametes to maintain genome stability and the potential to adapt to changing environments. Haploidization is achieved through two successive rounds of cell division after a single initial pre-meiotic DNA replication. Meiosis I segregates the homologous chromosomes, followed by the segregation of the sister chromatids in meiosis II. Genetic diversity is achieved through the process of recombination that describes the exchange of genetic material between the maternal and paternal homolog. Recombination and the initial steps of haploidization are executed already early on in prophase I. Both essential processes depend on a variety of multiprotein complexes, such as the linker of nucleo- and cytoplasm (LINC) complex and the synaptonemal complex (SC). The LINC complexes facilitate telomere-led chromosome movements that persist throughout prophase I by transducing force generated in the cytoplasm onto the meiotic telomeres, thereby driving the pairing, synapsis, recombination, and segregation of the homologous chromosomes. The SC serves as a scaffold that synapses the homologs and is involved in recombination. The structure of multiprotein complexes is adjusted according to their function, environment, and the forces they are subjected to. Coiled-coil domains typical in load-bearing proteins characterize the meiotic mechanotransducing LINC complexes. SCs resemble ladder-like structures that are highly conserved amongst eukaryotes, while the primary sequence of the proteins that form the complex display very little if any sequence homology. Despite the apparent significance of the structure to their function, little quantitative and topological data existed on the LINC complexes and the SC within their morphological context prior to the present work. Here, the molecular architecture of the meiotic telomere attachment site where LINC complexes reside and the SC have been analyzed in depth, mainly on the basis of electron microscope tomography derived 3D models complemented by super-resolution light microscopic acquisitions of the respective protein components. The present work determines the stoichiometry, topology, and organization of the LINC complexes and the transverse filaments of the SC. The key findings include an asymmetric monolayered arrangement of the transverse filaments within the SC, which disproves the common assumption of a highly symmetric and bilayered organization and a first estimate of the forces required for telomere-led prophase movements transduced by LINC complexes.

# Zusammenfassung

Sich sexuell fortpflanzende Organismen sind auf die Meiose angewiesen, um haploide, genetisch vielfältige Keimzellen zu erzeugen, die die Stabilität des Genoms und die Fähigkeit zur Anpassung an sich verändernde Umgebungen erhalten. Die Haploidisierung wird durch zwei aufeinanderfolgende Runden der Zellteilung nach einer einzigen anfänglichen prä-meiotischen DNA Replikation erreicht. In der Meiose I werden die homologen Chromosomen getrennt, gefolgt von der Trennung der Schwesterchromatiden während der Meiose II. Genetische Diversität wird durch den Prozess der Rekombination erreicht, der den Austausch von genetischem Material zwischen den mütterlichen und väterlichen Homologen beschreibt. Die Rekombination und die ersten Schritte der Haploidisierung werden bereits früh in der Prophase I durchgeführt. Beide essentiellen Prozesse hängen von einer Vielzahl von Multiproteinkomplexen ab, wie z.B. dem Linker of Nucleo- and Cytoplasm (LINC)-Komplex und dem synaptonemalen Komplex (SC). Die LINC-Komplexe erleichtern telomergeführte Chromosomenbewegungen, die während der gesamten Prophase I fortbestehen, indem sie die im Zytoplasma erzeugte Kraft auf die meiotischen Telomere übertragen und dadurch die Paarung, Synapsenbildung, Rekombination und Segregation der homologen Chromosomen vorantreiben. Der SC dient als ein Gerüst, das die Homologen eng verbindet und ist an der Rekombination beteiligt. Die Struktur von Multiproteinkomplexen wird je nach ihrer Funktion, ihrer Umgebung und den Kräften, denen sie ausgesetzt sind, angepasst. Coiled-coil-Domänen, die für tragende Proteine typisch sind, charakterisieren die meiotischen, mechanotransduzierenden LINC-Komplexe. SCs ähneln leiterähnlichen Strukturen, die unter Eukaryonten hoch konserviert sind, während die Primärsequenz der Proteine, die den Komplex bilden, sehr wenig bis gar keine Sequenzhomologie aufweist. Trotz der offensichtlichen Bedeutung der Struktur für ihre Funktion gab es vor der vorliegenden Arbeit nur wenige quantitative und topologische Daten über die LINC-Komplexe und den SC in ihrem morphologischen Kontext. Hier wurde die molekulare Architektur der Telomeranheftungsstellen, an denen sich die LINC-Komplexe befinden, und die des SCs eingehend analysiert, hauptsächlich auf der Grundlage von auf der Elektronenmikroskop-Tomographie basierenden 3D-Modellen, ergänzt durch hochauflösende lichtmikroskopische Aufnahmen der jeweiligen Proteinkomponenten. Die vorliegende Arbeit bestimmt die Stöchiometrie, Topologie und Organisation der LINC-

Komplexe und der Transversalfilamente des SCs. Zu den wichtigsten Ergebnissen gehört eine asymmetrische monolagige Anordnung der Transversalfilamente innerhalb des SCs, die die gängige Annahme einer hochsymmetrischen und zweischichtigen Organisation widerlegt, sowie eine erste Abschätzung der Kräfte, die für telomergeführte Prophasenbewegungen erforderlich sind, die von LINC-Komplexen übertragen werden.

# Contents

# 1 Introduction

The prerequisite to sexual reproduction is the generation of haploid gametes. The haploidization of the set of chromosomes in gametocytes avoids the doubling of genetic material with every generation and thus maintains the genetic stability in the offspring upon fusion of the mature egg and sperm cell during fertilization. The process that generates the haploid gametes from diploid germ cell precursor cells is referred to as meiosis.

In 1876, Oskar Hertwig observed the fusion of the sperm and egg for the first time in transparent sea urchin eggs [1] and deduced that in the process maternal and paternal traits would be passed down to the offspring. Only seven years later, Eduard Van Beneden described the phenomenon of haploidization in *Ascaris megalocephala* samples. He almost did not make this ground-breaking discovering since the samples in which he observed the chromosome reduction were on the brink of being discarded. Eggs of female worms that had been fixated in alcohol months earlier had continued to develop in the meantime and now showed a clear reduction of the germ cell chromosomes [2, 3]. The fact that the haploidization of gametocytes requires two rounds of cell division was determined another seven years later, in 1890, by August Weismann [4]. In early 1900, Theodor Boveri and Walter Sutton originated the chromosome theory of inheritance [5, 6, 7], a biological milestone, stating that the chromosomes are the medium for genetic inheritance. The term meiosis used for the haploidization step of gametogenesis today was first introduced in 1905 as "maiosis" by J.B. Farmer and J.E.S. Moore [8]. The origin of the word stems from the Greek word με´ωσις that translates into "lessening". The spelling was promptly adapted to meiosis by Koernicke as well as Pantel and De Sinety for linguistic reasons [9]. In 1911, Thomas Hunt Morgan recognized that, on occasion, closely linked "traits" were passed on independently to progeny. Based on this observation, he inferred that genes can be exchanged between chromosomes through "cross over" [10]. Exactly 20 years later, Barbara McClintock and Harriet Creighton visualized crossing over in maize and showed that it is accompanied by gene exchange [11]. At this point, the two key concepts of meiosis, haploidization, and recombination that grant the generation of genetically diverse gametes while ensuring genome stability upon fertilization had been uncovered.

Since then, a lot of research has been conducted to understand the intricate processes of meiosis. A wide range of proteins that are involved in these processes have been identified and characterized. The mechanisms behind the meiotic program are however still not fully understood. There is no doubt of the importance of meiosis for sexually reproducing organisms. Even early-branching eukaryotes, such as protists, undergo the canonical meiotic program [12, 13, 14]. Disruptions of this program often lead to severe birth defects caused by aneuploidies (e.g., Down syndrome), spontaneous abortions, and infertility. Due to the importance of meiosis for haploidization, it is crucial to continue unraveling its mechanisms.

Infertility is a global issue that affects around 15% of all couples, which equals about 48.5 million couples worldwide [15]. According to the WHO, in developing countries, 1 in 4 couples struggles in terms of reproductive health. Roughly 40% of infertility cases overall can be attributed to the male [16]. Though mostly classified as idiopathic, increasing evidence points to genetic defects as the cause for infertility in a large number of cases [17, 18, 19, 20, 21, 22, 23, 24]. The number of genes that regulate the complex human fertility is vast. Consequently, an equally large number of different errors could occur that perturb gene function [25]. The diversity of defects and the fact that many cases remain undetected lead to a low number of potential test subjects for human infertility studies. A pivotal alternative for respective studies are animal models, especially mouse models due to the high degree of similarity between the mammals and the availability of large genetic toolbox [26].

## 1.1 Meiosis

Unlike mitosis in which the chromosomes are separated in a single division, chromosome segregation during meiosis depends on two consecutive cell divisions referred to as meiosis I and meiosis II. Following a single round of DNA replication, meiosis I separates the maternal and paternal copy of the chromosomes, referred to as homologous chromosomes. Without an intermediate duplication of genetic material, meiosis I transitions into the equational cell division meiosis II that is similar to mitosis and results in the segregation of the sister chromatids. Consequently, meiosis leads to the

generation of four haploid cells. In females, only one of these cells matures into an oocyte, while the other three degenerate into polar bodies. In the male, all four meiotic products mature into sperm in the process that is referred to as spermiogenesis in connection to meiosis.

Meiosis I is unique as it leads to the haploidization of the germ cell precursors through the segregation of the homologs. Since it reduces the ploidy of the meiocytes, meiosis I is referred to as the reductional cell division. It further harbors the exchange of DNA between the homologs, known as recombination, that results in what is cytologically observable as crossing-over. Meiosis I is subdivided into four stages: prophase, metaphase, anaphase, and telophase by the end of which cytokinesis takes place. Prophase I is by far the longest of the meiotic phases and is characterized by the two key meiotic events haploidization and recombination. It is divided into five substages, namely leptonema, zygonema, pachynema, diplonema, and diakinesis, that host specific meiotic events as shown in Figure 1. At the onset of meiosis, in leptotene, DNA double strand breaks (DSBs) are induced along the chromosomes in preparation for recombination at a later prophase stage. After DNA double strand breaks are established, the chromosomes condense with the help of condensins. The duplicated chromatids of the condensed chromosomes are held together by sister chromatid cohesion. In mammals, four different cohesin complexes have been characterized in meiocytes that organize into a ring-like structure that encloses the sister chromatids. Each cohesin complex consists of a heterodimer of structural maintenance of chromosomes (SMC) proteins SMC1$\alpha/\beta$ (predominantly SMC1$\beta$) and SMC3, an alpha kleisin (RAD21, RAD21L, REC8) and the stromal antigen 3 (STAG3) [27]. Sister chromatid cohesion is maintained along the whole chromosome until the metaphase I/anaphase I transition, at the centromeres even until the metaphase II/ anaphase II transition. The expression of SMC1$\beta$ and STAG3 is accompanied by the expression of SYCP3 and SYCP2 during leptotene [28, 29]. SYCP3 and SYCP2 are proteins of the so-called axial elements. The axial elements are distinct longitudinal protein scaffolds that form the early chromosome axis by associating with the condensin and cohesin complexes that organize the meiotic chromosomes into regular loops alongside the scaffolds. Right at the onset of meiosis, the telomeres of the chromosomes attach to the nuclear envelope (NE; see Figure 1), a prerequisite to rapid telomere-led prophase movements that will be discussed

in Section 1.2. Chromosome movements persist beyond leptonema, lasting throughout the whole of prophase I, as they are the driving force behind the pairing of the homologs in preparation for DNA exchange at a later stage, referred to as homologous recombination as well as segregation. In order for the homologs to pair, they have to find each other in the crowded nucleus. With the presumed goal of reducing the area in which the homologous chromosomes search for their partner to 2D [30], their telomeres move along the plane of the nuclear envelope, clustering in a distinct region of the nuclear envelope close to the microtubule organizing center (MTOC) in the short-lived bouquet configuration at leptonema/zygonema transition [31]. Aside from facilitating telomere pairing, telomere-led movements during bouquet are i.e., also presumed to solve non-homologous entanglements [32]. Once homolog pairing is established, the homologous chromosomes begin to align along their entire length. The alignment is stabilized by the formation of a proteinous scaffold, the synaptonemal complex (SC), between the homologs. The SC forms on the basis of the axial elements, now referred to as lateral elements through the continuous addition of numerous perpendicularly organized filamentous proteins that together with proteins at the center of the complex connect the homologs gradually like the teeth of a zipper. In pachytene, the synaptonemal complex is fully assembled and telomeres are re-dispersed over the nuclear envelope. As the main event at this stage, one to three, even five, recombination events occur per chromosome. During recombination, double strand breaks that were introduced to one of the homologs at the onset of meiosis are resolved using the other homolog as a reference/template. At the site of double strand breaks, an exonuclease creates $3'$ single-stranded overhangs that pair with the homologous region of the other parental chromosome through strand invasion into the respective sister chromatid for DNA synthesis. The joint molecule that results from the process of strand invasion is eventually resolved, re-establishing two separate, recombined chromosomes [33]. After successful recombination, the synaptonemal complex disassembles in diplonema. The homologs remain connected solely at the newly formed chiasmata, where recombination occurred while becoming fully condensed in preparation for the further progression of meiosis. The main events of each prophase stage from chromosome condensation and telomere attachment (**leptotene**) to finding and pairing (**zygotene**) of the homologs and the start of SC formation, to complete SC assembly and recombination (**pachytene**) and finally SC dissociation under chiasmata maintenance (**diplotene**) before segregation

all driven by continuous chromosome movements are visually summarized in Figure 1 for reference.

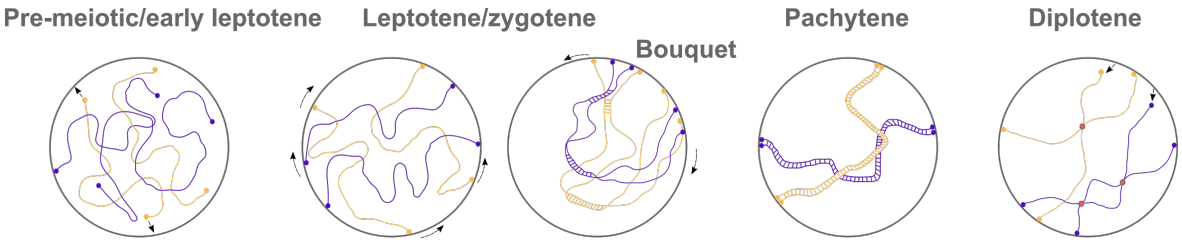


**Figure 1: Mammalian prophase I.** Prophase I of meiosis is subdivided into five stages: leptonema, zygonema, pachynema, diplonema and diakinesis (not depicted). At the transition from pre-meiotic S-phase to leptotene, the homologous chromosomes condense and the axial elements (purple, yellow) associate with the sister chromatids. The telomeres (purple and yellow circles) begin to attach to the nuclear envelope (nuclear arrows) and start moving along its plane (cytoplasmic arrows) once firmly attached. Leptotene and the subsequent zygotene are characterized by rapid telomere movements that drive the recognition and pairing of the homologous chromosomes. At leptonema/zygonema transition, the telomeres cluster in what is referred to as bouquet configuration at a distinct membrane region close to the microtubule organizing center. The proximity of the telomeres likely facilitates homolog detection, which initiates the synapsis along the entire length of the homologs. Synapsis is reinforced by the local association of the transverse filaments with the former axial elements, now referred to as lateral elements and the subsequent incorporation of the central element proteins that completes the formation of the synaptonemal complex (SC). Prior to the transition into pachytene, the telomeres are re-dispersed over the nuclear envelope. In pachytene, synapsis is complete and the SC is fully assembled between the homologs. At this stage, recombination occurs, which is cytologically represented by the formation of chiasmata. After successful recombination, the SC starts to disassemble and nuclei progress to diplotene. During diplotene, SC dissociation is completed with the homologs only remaining connected at the chiasmata (red circles0). Finally, the telomeres begin to detach from the nuclear envelope (nuclear arrows) before the meiotic nuclei transition to the last stage of prophase I, diakinesis (not shown), where the nuclear envelope disintegrates and spindle formation is initiated in preparation for metaphase I. Figure adapted from Kracklauer et al. [34].

## 1.2 The meiotic LINC complex

As mentioned earlier, prophase I is characterized by continuous chromosome movements. The first recollection of these movements dates back to 1976 when oscillatory migration of chromosomes was detected in time-lapse acquisitions of rat spermatocytes [35]. Over forty years later, a wide range of studies have been conducted in a variety of model organisms to understand the chromosome movements and their role in meiosis [36, 37, 38, 39, 40, 41, 42, 43, 44, 45, 46, 35, 47, 48, 49]. These studies have revealed a common principle of how the chromosome movements are orchestrated. They are led by the chromosome ends and depend on the cytoplasmic motor machinery whose generated force is transduced onto the chromosome ends by linker proteins that connect the cyto- and the nucleoplasm. Chromosome movements have a prominent role in homolog pairing as they facilitate the clustering of the chromosome ends at a distinct

region of the nuclear envelope. The physical proximity attained through the clustering promotes the mutual recognition of homologs. In the event of non-homologous pairings, the chromosome movements seem to separate the undesired unions. Aside from pairing, chromosome motion is further required for the assembly of the synaptonemal complex, thereby promoting recombination, and also seems to be involved in segregation.

The prerequisite to chromosome end movements during meiotic prophase I is the attachment of the chromosome ends to the nuclear envelope at the onset of meiosis. Both the anchorage of the chromosome ends as well as the continuous chromosome end-led movements are highly conserved and are potentially a universal feature to eukaryotes [50]. While the protein complexes that are responsible for the attachment and movement of chromosome ends carry out the same or at least highly similar functions, the protein components of the complexes and the chromosome regions that mediate attachment differ between organisms. In yeast (*Schizosaccharomyces pombe/ S.pombe* and *Saccharomyces cerevisiae/ S.cerevisiae*) and mouse the telomeres attach to the nuclear envelope, while in worms like *Caenorhabditis elegans/ C.elegans* so called the pairing centers, specific regions near one end of the worms' chromosomes, attach the meiotic chromosomes to the nuclear periphery. The attachment of the telomeres or pairing centers is mediated by a complex of chromosomal scaffold proteins: Bqt1/2/3/4, Rap1 and Taz1 in *S.pombe*, Ndj1 and Csm4 (*S.cerevisiae*) in S.cerevisiae, HIM8 and ZIM-1/2/3 in *C.elegans* and TERB1, TERB2, transitorily TRF1 and MAJIN in mouse [51]. These telomere and pairing center binding proteins anchor the meiotic chromosome ends within the nuclear envelope by (predominantly) embedding them within the nuclear lamina. The latter consists of Ce-lamin [52], a B-type lamin isoform in *C.elegans* and lamin B1 as well as meiosis-specific A-type lamin isoform lamin C2 in mouse [53, 54, 55]. Yeasts, on the other hand, do not have a lamina. The meiotic lamina has been shown to be vital for the success of meiosis, as it facilitates the rapid prophase movements (RPMs) required especially for pairing and synapsis [56]. The meiosis-specific lamin C2 was shown to exceed the mobility of other A-type lamins [57]. The reason for the increased mobility of Lamin C2 is the inherent lack of the N-terminal domain, which mediates lamin polymerization in the other A-type lamins [58, 59]. Lamin C2 is thought to alter the nuclear envelope in a site-specific manner that aid in the at-

tachment and movement of the meiotic telomeres [60]. An essential requirement to facilitate movement of the anchored telomeres/pairing centers is a protein bridge that links the chromosome ends with the force-generating cytoplasmic motor machinery. According to their function of linking the nucleo- and cytoplasm, these protein bridges are referred to as linker of nucleo- and cytoplasm, or for short, LINC complexes. LINC complexes consist of the inner nuclear membrane SUN-domain proteins and the outer nuclear membrane KASH-domain proteins. Table 1 shows an overview of the LINC complex compositions in the different model organisms.

**Table 1:** Composition of the meiotic LINC complexes in different model organisms.

| | SUN domain proteins | KASH domain proteins |
|---|---|---|
| *S.pombe* | Sad1 | Ksm1 |
| *S.cerevisiae* | Msp3 | ? |
| *C.elegans* | SUN-1 | ZYG-12 |
| *Mus musculus* | SUN1/2 | KASH5 |

The force transduced by the LINC complexes is predominantly generated by the microtubule-dependent motor system. In *C.elegans*, *S.pombe* and mouse, the force is produced by dynein, which is additionally supported by dynactin in mouse or dynactin and kinesin in *S.pombe*. Interestingly, *S.cerevisiae* is the only system in which the meiotic chromosome movements are propelled by actin motors [61].

Indifferent of species-related differences in chromosome attachment (telomeres vs pairing centers, species-specific composition of chromosomal scaffold proteins), the function of the motile attachments in supporting pairing and synapsis by moving the telomeres into bouquet formation or into transient clusters of a few pairing centers in case of *C.elegans* [44] is equivalent between organisms.

Despite the similarities in ortholog function and the availability of simple model organisms for the study of meiotic processes, a deeper understanding of these complex processes requires the investigation of higher eukaryotes [62]. For this purpose, the mouse has become a suited and well-established model organism. The present study intends the characterization of mammalian, multiprotein complexes involved in meiotic processes and was thus conducted in the mouse.

On the ultrastructural level, the murine telomere attachment is characterized by two electron-dense plates that seem almost continuous with the nuclear envelope and with the ends of the tripartite synaptonemal complex, the latter of which will be discussed in Section 1.3. The first reports of the morphology of the meiotic telomere attachments go back to electron microscopic reports of Moses in 1956 [63, 64]. The attachment plates contain telomeric repeat sequences [65], which makes it likely that also the murine telomeric binding proteins localize to these sites. In mouse, the meiosis-specific complex of telomere binding proteins consists of TERB1, TERB2, and MAJIN. The complex takes over the telomeres from the somatic shelterin complex in a process referred to as cap exchange. While the cap exchange is in progress, the telomere binding proteins form a chimeric complex with the shelterin core component TRF1. The chimeric complex persists until the cap exchange is complete, cytologically observed as the sequestering of TRF1 in a ring-like shape that peripherally circumscribes the telomere binding proteins mid-prophase [66]. Whether the meiotic telomere binding proteins localize to the attachment plates has not been shown to date. Depending on the enrichment of proteins, the attachment plates appear to blend with the lateral elements of the SC. They are however independent structures, devoid of SYCP3, as shown in SYCP3 knockout mice where the attachment plates persist despite the lack in expression of SYCP3 [65]. Towards the nuclear envelope, the electron-dense attachment plates are seemingly in continuity with a mesh of cytoplasmatic filaments that originate from each of the two plates at a telomere attachment (see Figure 2). The filaments appear to span the perinuclear space and reach into the cytoplasm [67, 68, 69]. Based on their topology, they are assumed to be LINC complexes. The localization of the inner nuclear components of the LINC complexes, SUN1 and SUN2, to the perinuclear part of the filaments support this notion [70, 71].

LINC complexes are ubiquitously expressed and fulfill a wide range of functions related to force transduction, such as nuclear positioning, migration, and anchoring [73, 34]. They consist of Sad1/UNC-84 homology (SUN) domain proteins and Klarsicht, Anc1 and Syne 1 homology (KASH) domain proteins that interact via their eponymous C-terminal domains. A minimum of five SUN and six KASH domain proteins are expressed in mammals, which arrange into hetero-hexameric complexes. SUN domain proteins carry a perinuclear coiled-coil domain that is central to the protein's structural

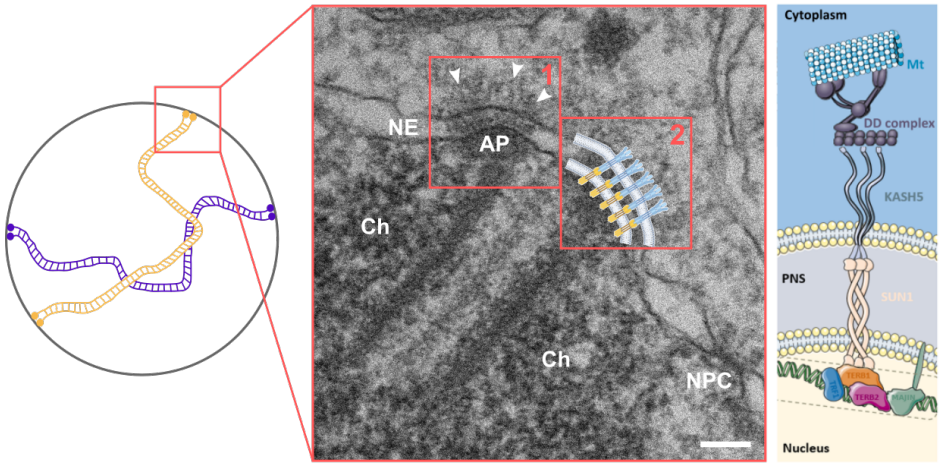


**Figure 2: The murine telomere attachment site.** Schematic representation showing the pachytene nucleus on the left with the telomere attachment site framed in red. In electron micrographs of these attachment sites (middle frame), the tripartite synaptonemal complex is associated with the nuclear envelope whose two lateral elements each seemingly transition into an electron-dense attachment plate (AP). A multitude of filamentous proteins (arrowheads) emanate from the attachment plates into the cytoplasm (1). The localization of these filaments to the meiotic telomere attachment sites and their connecting role of the nucleo- and cytoplasm suggests that these proteins are assemblies of meiotic LINC complexes (2). The composition of a single murine LINC complex at an attachment site is shown on the right. LINC complexes consist of a trimer of the inner nuclear membrane protein SUN1/2, whose N-terminus interacts with the proteins of the telomere binding complex (TERB1/2, MAJIN that are initially in a chimeric complex with TRF1) and the nuclear lamina (not shown). The C-terminal eponymous domain of SUN1/2 interacts with the short C-terminal eponymous domains of three outer nuclear membrane KASH5 peptides. The N-terminus of KASH5 terminates in the cytoplasm and carries a dynein binding domain that mediates the interaction between the LINC complex and the microtubule-dependent motor system. NE: nuclear envelope, AP: attachment plate, Ch: Chromatin, NPC: nuclear pore complex, DD-complex: dynein-dynactin complex, Mt: microtubule. Scale bar: 100 nm. Figure adapted from [72].

and regulatory functions. Firstly, the domain is characteristic of load-bearing proteins as it enhances the flexibility of the proteins. Coiled-coils can further act as molecular spacers. In HeLa cells devoid of SUN proteins, the physiological spacing of the nuclear envelope of 40-50 nm was lost [74]. Hence, LINC complexes likely contribute to the maintenance of a regular nuclear envelope spacing. The coiled-coil domain also provides the structural basis for the proteins' oligomerization potential. Crystallographic data of human SUN2 ($SUN2_{522\text{-}717}$) has shown that the protein organizes into a trimer via a short preceding coiled-coil domain of trimeric $\alpha$ helix 3 ($\alpha 3$) [75, 76]. In 2016, the solving of a slightly larger crystal of the SUN2 protein resolved the two additional alpha helices ($\alpha 1$ and $\alpha 2$) that precede the short $\alpha 3$ helix [77]. The three alpha helices form the coiled-coil 2 (CC2) adjacent to the SUN domain. Distal to CC2, another large coiled coil is adjoined referred to as coiled-coil 1 (CC1). In solution, CC2 is monomeric, translating into the presence of one of each alpha helices. In the monomeric state, the three helices form a bundle that prohibits the SUN domain from interacting with the

eponymous domain of a respective KASH domain protein. To transition from this inactive conformation into an active one, or in other words, enable the formation of a LINC complex, the trimerization of CC1 is required to release the SUN domain. Consequently, the data hints at the regulation of the LINC complex formation on the basis of the oligomerization state of the coiled-coil domains of SUN [77]. Whether only $\alpha 3$ or all three of the CC2 helices arrange into a trimer remains elusive. The crystal structures of the monomeric and trimeric SUN2 were solved in different species. In 2018, Jahed et al. used computational based analyses to model the behavior of the SUN1 molecule in comparison to SUN2 [78]. The analyses support the plausibility of the model of an inactive monomer that gets activated upon conformational changes induces by trimerization, thereby enabling the binding of KASH peptides that had been proposed for SUN2 also for SUN1. Based on the simulations, the authors further introduce a model of SUN multimerization via the eponymous domains of neighboring SUN domain proteins [78]. Multimerization of LINC complexes has been discussed intensively since multimerization of certain KASH domain proteins has been observed [79, 80, 81]. The crystallographic data of SUN2 does not support oligomerization of the transmembrane helices of KASH domain proteins of the same LINC complex. The cloverleaf-like SUN domain forms an ideal threefold symmetry into which the KASH peptides insert at a distance of 50 Å. The predefined distance of the KASH peptides prohibits their interaction at these sites. Sosa et al., who conducted the crystallographic study of SUN2, instead proposed the possibility of the interaction between KASH domain proteins of neighboring LINC complexes [75]. Unpublished crystallographic and biophysical data of the lab of Owen Davies supports the multimerization of LINC complexes into a branched network of SUN-KASH 6:6 assemblies [82].

In mouse meiocytes, the LINC complex consists of SUN1/2 and KASH5. Unlike in somatic cells, where the LINC complexes cover the entire nuclear periphery, LINC complex localization is confined to telomere attachment sites in meiocytes. SUN1 and SUN2 appear to have redundant roles during meiosis. SUN2 localizes to the meiotic telomere attachment site in mouse [70]. While the protein is not essential to meiosis, since its depletion does not interfere with meiotic progression in the way that SUN1 does, SUN2 has a rescue effect on telomere attachment and movement upon loss of SUN1. In SUN1 knockout mice, SUN2/KASH5 LINC complexes provide telomere at-

tachment to the nuclear envelope and facilitate the formation of bouquet-like clusters and even recombination events [83].

At the onset of meiosis, SUN1 is recruited to the telomere attachment sites by TERB1 and TRF1 of the chimeric complex of chromosomal scaffold proteins TERB1/2, MAJIN and TRF1. At these sites, SUN1 further interacts with the meiotic lamina consisting of lamin B1 and the unique, meiosis-specific A-type lamin isoform lamin C2 [53, 54, 55]. Lamin C2 is unique as it lacks an N-terminal domain that mediates lamin polymerization in other A-type lamins and provides the protein with increased mobility [58, 59]. Lamin C2 further concentrates solely in distinct domains with which the attached meiotic telomeres associate during prophase I [60], likely redecorating the telomere attachment sites in support of prophase telomere movements [60]. SUN1 recruits the tail-anchored KASH5 protein to the telomere attachment sites. While the C-terminus of KASH5 carries the KASH domain that is characterized by a sequence of 30 conserved amino acids ending with a highly conserved PPPX motif (in mouse the most common PPPT), the large N-terminus of KASH5 is characterized by a dynein-binding domain. As mentioned earlier, dynein in complex with dynactin generates the microtubule-dependent force required for prophase telomere movements in mouse [84]. Figure 2 shows an overview of the known protein components that define a motile telomere attachment site (with the exception of the meiotic lamina). Depletion of the individual components of the LINC complexes leads to a severe reduction of telomere motion in case of *Sun1*$^{-/-}$ or complete immobility of attachments in KASH5 knockout mice [32]. Residual movement in SUN1 knockout mice might be related to the redundancy between SUN1 and SUN2. Overall, LINC complexes are clearly essential to meiotic telomere movement and therefore for the progression and success of meiosis.

Despite its essential role in meiosis and the apparent significance of the LINC complex structure to its function, little is known about the stoichiometry and distribution of LINC complexes at telomere attachment sites that would enrich our understanding of the mechanisms behind their force transduction properties. The limited topological information that exists on the meiotic LINC complex is based on immunolocalization of SUN1 and KASH5 in relation to the synaptonemal complex protein SYCP3. In wide-field acquisitions of SUN1 and KASH5 immunolocalizations, the proteins are visualized

as two respective foci for each protein distal to the ends of SYCP3. In comparative structured illumination microscopic acquisitions at roughly twice the lateral resolution of diffraction-limited acquisitions, the respective SUN1 and KASH5 signals locate accordingly distal to SYCP3, yet with a ring-like opposed to a focal signal shape [46, 85]. Within its morphological complex, the equivalence of the filamentous proteins that emanate from the attachment plates into the cytoplasm with the meiotic LINC complexes is not yet fully proven. Moreover, the two-dimensional nature of the electron microscopy micrographs of telomere attachment sites shows the presumed LINC complexes superimposed and thus does not allow a quantitative or topological analysis of the presumed LINC complexes at these sites [68, 65]. In order to elucidate the molecular architecture of meiotic telomere attachment sites with a special focus on the LINC complexes at these sites, a three-dimensional, quantitative model of the sites is required.

## 1.3 SC

Maybe the most prominent multiprotein complex of meiosis is the synaptonemal complex (SC). It was first described in 1956 in the paper of Moses et al. that also contains the first recollection of the presumed filamentous meiotic LINC complexes emanating from the inner nuclear membrane [63] as well as by Fawcett [86]. The structure associates with the nuclear envelope at both ends and twists around the own axis through the meiotic nucleus, exposing alternating frontal and lateral view sections. In electron microscope micrographs, the synaptonemal complex appears as a tripartite structure that resembles a ladder. The rails of the ladder are referred to as lateral elements, connected by a multitude of perpendicular transverse filaments as rungs of the ladder. The rungs span only half of the region between the two lateral elements terminating in a central element that is right in the middle between the lateral elements, as shown in Figure 3. Synaptonemal complexes are a common feature of sexually reproducing organisms [87, 88]. The complex was lost on several occasions during evolution, thus it remains elusive whether it is a primordial feature of eukaryotes or was acquired later [50]. The SC has a central role in the synapsis and recombination of homologous chromosomes. During synapsis, it serves as a scaffold that connects the homologs at a distance that presumably suits the recombination process where the SC is thought to provide a platform for the loading of the recombination machinery. While the size

of the synaptonemal complex differs amongst species, the distance between the two lateral elements, also referred to as the central region, underlies little species related fluctuations and ranges from 90–150 nm [89].

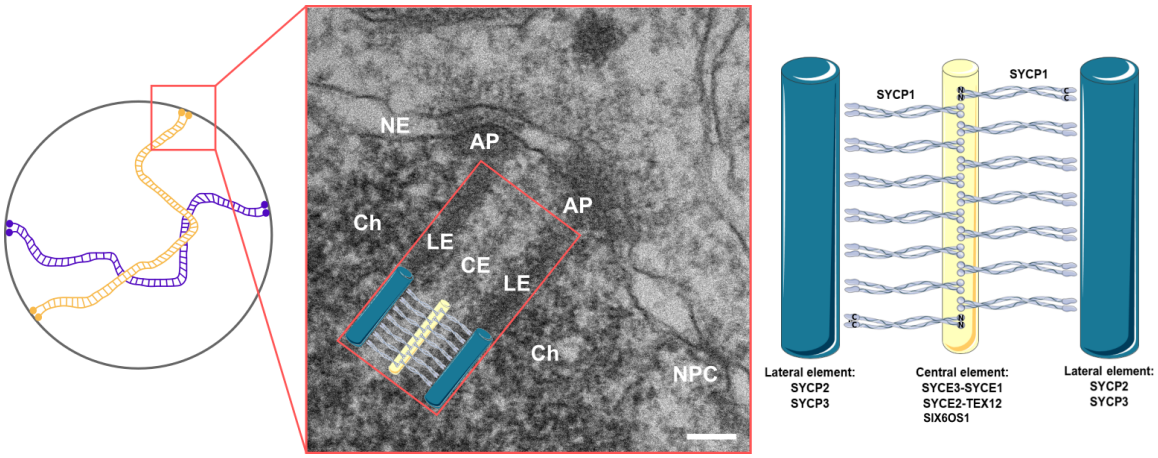


**Figure 3: The murine synaptonemal complex (SC).** Schematic representation showing the pachytene nucleus on the left with the telomere attachment site framed in red. At the telomere attachment site, the synaptonemal complex that turns around its own axis through the meiotic nucleus is represented as a prominent tripartite structure of two lateral elements (LEs) and a central element (CE) that are connected by a number of transverse filaments. Here, the ends of the lateral elements are characterized by conical thickenings that are seemingly continuous with the electron attachment plates (AP), which are closely associated with the nuclear envelope (NE). The composition of the SC, which serves to connect the homologous chromosomes, is schematically depicted on the right. The lateral elements consist of SYCP2 and SYCP3, the central element of SYCE1-3, TEX12, and SIX6OS1. The transverse filament consists of dimers of SYCP1 whose C- and N-terminus are associated with the lateral and central element. Ch: Chromatin. Scale bar: 100 nm. Figure adapted from [90].

The structure of the synaptonemal complex is widely conserved and consists almost entirely of protein (>90%) [91]. Interestingly, the analogous protein components that form the SC have however little sequency homology despite serving as the same building blocks in SC assembly [92, 93]. The analogy between the lack of sequency homology of the SC proteins amongst the organisms but the similarity in the scaffold they form and house building was drawn [94]. While the houses differ in size and materials used for construction, the general architectural composition of walls, windows, and a roof. The different components that make up the lateral elements, the central element, and the transverse filaments are summarized in Table 2. *S.pombe* does not form synaptonemal complexes. Here, synapsis and recombination depends on the formation of so-called linear elements (LinEs) [95].

SYCP3, SYCP2, and SYCP1 were the first three mammalian SC proteins that were discovered. They were initially identified by the lab of Christa Heyting through the gener-

**Table 2:** Composition of the synaptonemal complex in different model organisms.

| | Axial/lateral element proteins | Central element proteins | Transverse filaments/ central region proteins |
|---|---|---|---|
| *S.pombe* | - | - | - |
| *S.cerevisiae* | Red1, Hop1, Mek1 | Ecm11, Gmc2 | Zip1 |
| *C.elegans* | HTP-1/2/3, HIM-3 | SYP-2 | SYP-1, SYP-3, SYP-4 |
| *Mus musculus* | SYCP2, SYCP3 | SYCE1-3, TEX12, SIX6OS1 | SYCP1 |

ation of monoclonal antibodies against purified SCs from rat spermatocytes [96, 97, 98]. About a decade later, the proteins of the central element were discovered. In 2004, Costa et al. first identified SYCE1 and SYCE2 [99]. Two years later, Hamer et al. uncovered the existence of a third central element protein, TEX12 [100]. Two additional central element proteins are known to date, SYCE3 discovered by Schramm et al. in 2011 [101] and SIX6OS1 in 2016 by Gómez-H [102]. Consequently, eight SC proteins are known so far.

At the onset of meiosis, the meiotic chromosomes condense and organize into a chromosome axis of regular loops. As mentioned earlier, the organization of the chromosomes is supported by the ring-like cohesin complexes that encircle the sister chromatids along the length of the chromosomes. Initially, Rec8 establishes the axial elements between the sister chromatids during pre-meiotic S-phase [28] before the rest of the cohesins (SMC1$\alpha/\beta$,SMC3,RAD21, and later RAD21L) decorate the meiotic chromosome axis. At the same time, SYCP2 and SYCP3 are loaded onto the axis, completing the assembly of the axial elements, at a later stage referred to as lateral elements. Both SYCP2 and SYCP3 contain coiled-coil domains. The central coiled-coil of the short SYCP3 mediates the oligomerization of the protein or the self-assembly into multi-stranded fibers when expressed ectopically [103, 104]. The coiled-coil at the C-terminus of SYCP2 is essential for the interaction between SYCP2 and SYCP3 [105]. Crystallographic data of SYCP3 has revealed an antiparallel tetrameric assembly of the protein, where the N-termini are exposed at either side. The SYCP3 N-termini are characterized by basic residues, which are likely DNA binding sites and were proposed to function as molecular spacers in chromatin organization [106]. SYCP3 can be SUMOylated, the function of the protein modification however remains elusive [107]. In SYCP3 knockout mice, telomeric repeats dissociate from the nuclear envelope, which coincides with a lack in SC initiation [65]. Telomere movements in these mice are significantly reduced [32].

The depletion of both SYCP2 and SYCP3 leads to pre-meiotic arrest [105, 108], which confirms their essential role in SC formation and meiotic progression. Patients that are heterozygous for a mutation in SYCP3 are affected by azoospermia [109]. The loss of SYCP3 is, aside from the loss of the double strand inducing SPO11, the only identified mutation confirmed to be linked to infertility [25].

During bouquet, pairing is established between the homologous chromosomes. The pairing is reinforced by the initiation of the synaptonemal complex assembly along the entire lengths of the homologs. For this purpose, the transverse filament protein and subsequently the central element proteins are recruited to the axial elements, now referred to as lateral elements. The main protein component of the transverse filaments is SYCP1. The protein consists of a long central coiled-coil required for dimerization. The unstructured N- and C-terminus of SYCP1 are presumably anchored within the lateral element (SYCP1 C-terminus) and the central element (SYCP1 N-terminus) [110, 111], spanning half the central region. When expressed ectopically, the molecule arranges into polycomplexes that resemble stacks of SCs [112]. These polymerization studies further infer that the central coiled-coil of SYCP1 is likely the main mediator of the SC width. The C-termini of SYCP1 contain basic patches that are separated by approx. 30Å and are likely DNA binding sites [113]. SYCP2 interacts with SYCP3 and SYCP1, while the latter do not interact directly [103, 110, 104, 114]. Only in the presence of SYCP1 are the proteins of the central element recruited to the synaptonemal complex [115]. Initially, SYCE3 and SYCE1 associate with the transverse filament protein, before SYCE2 and TEX12 are recruited [116, 99]. SIX6OS1 associates with SYCE1 [102]. By pachytene, the mature SC is fully assembled. The SC in yeast has shown that the mature complex remains dynamic by continuous incorporation and loss of SC components [117]. With the progression of meiosis, the incorporation of components exceeds their dissociation from the complex. The dynamic state of the synaptonemal complex that lasts from assembly to disassembly is likely the result of an interplay of multiple regulatory instances [89] that are interconnected with meiotic progression. These include common transcriptional and translational controls, post-translational modifications and influences on the life span of the proteins [118, 119, 120, 89, 121, 122]. They further encompass the unique layer of regulation by the meiotic cytoskeleton-driven chromosome movements [123, 85, 124, 42]

which depend on the telomere attachment to the nuclear envelope [125].

In late prophase, the SC is required to disassemble in preparation for segregation. The SC disassembly is mediated by Aurora B and Polo-like kinase 1 (PLK1), the latter of which phosphorylates SYCP1, TEX1, and SYCE1 as a prerequisite for central and lateral element disassembly under chiasmata maintainance [126] concluding the life span of the SC.

A lot of progress has been made in terms of identification and characterization of the SC components. The most striking feature of the complex however is the essential nature of the complex's structure. Our understanding of the molecular architecture of the SC still remains limited. The advent of super-resolution microscopy has enabled the resolution of the topology of individual proteins in mouse, enhancing our understanding of the distribution of the protein components within the complex. In 2015, Schuecker et al. performed protein distribution analyses of SC proteins in frontal and lateral view sections on murine spreadings that were acquired with *d*STORM [127]. The analyses provided further evidence that the N- and C-termini are embedded within the central and lateral element of the SC as previously proposed on the basis of EM data [110, 111]. Interestingly, the central element proteins SYCE1-3 and SYCP1-N appeared bimodally distributed in lateral views of the SC, which hints at a bilayered organization of the complex [127]. The notion of a bilayered organization of the SC was refined by immunoelectron microscope (immuno-EM) localizations of the respective central element proteins in lateral views a year later. In agreement with the *d*STORM data, SYCP1 and SYCE3 were distributed bimodally. The immuno-EM based distributions of SYCE1 and SYCE2 on the other hand reflected a monolayered organization. The findings were integrated into a model where two outer layers that consist of SYCP1-N and SYCE3 enclose a central layer composed of SYCE1, SYCE2, and TEX12 [128]. Label-free approaches intended to uncover the molecular architecture of the SC are limited to early electron microscope tomography studies conducted in insects. Electron tomograms of the beetle *Blabs cribrosa* and *Drosophila melanogaster* revealed a multilayered organization of the SC in insects [129, 130]. The inherently diffuse nature of the central element in mouse and the limited technical and computational means at the time have prohibited the generation of according electron tomograms of the murine

SC. As a result, the current simplistic model of the SC only considers two-dimensional morphological data based on electron micrographs and portrays the SC as a tripartite structure of orderly arranged opposing transverse filaments. The actual stoichiometry and distribution of the transverse filaments are not known since the molecules appear superimposed in the respective 2D acquisitions. The present work seeks to close the gap of a missing quantitative model of the SC, with a special focus on the stoichiometry and topology of transverse filaments, based on actual morphological data. Here, advantage was taken of the technological progress by acquiring electron microscope tomograms of the murine synaptonemal complex and manually segmented them to generate 3D models as a basis for the quantitative analyses to gain a deeper understanding of the complex's function.

Multiprotein complexes are central platforms driving essential cellular processes to which the meiosis-specific LINC complexes and the synaptonemal complex are no exception. Their structure is hereby tightly linked to their function. Consequently, understanding the molecular architecture of the multiprotein complexes is a pivotal step to fully understanding their function in meiosis.

## 1.4 Aims

Most essential cellular processes are orchestrated by the interplay of several proteins arranged in multiprotein complexes, often in combination with other biomolecules such as DNA or RNA. The function of individual complexes depends on the "functional units" of biomolecules present in the respective complex, as well as their stochiometry and copy number. Consequently, a way of unraveling the function of a multiprotein complex is studying the spatio-temporal organization of the interacting components within the complex, in other words, their "molecular sociology" within the cell.

The resolution of the molecular architecture of the synaptonemal complex requires 3D nanoscale resolution. Suitable imaging tools are electron tomography, super-resolution light microscopic techniques, and X-ray crystallography. Each of these techniques has advantages and limitations. A comprehensive understanding of the SC structure that enriches our understanding of its function can only be achieved by integrating the insights of different imaging techniques.

With regard to the architecture of the SC, the aim of this thesis was to answer the following open questions using electron tomography complemented by expansion microscopy:

1. **Stoichiometry of transverse filaments** Little quantitative data on the transverse filaments, specifically their stoichiometry, has been acquired so far. An early study on the structure of the central region of hamster and house crickets reported 50-80 transverse filaments per micrometer and a width of the filaments of 1.6-1.8 nm. The results were derived in the two-dimensional context of whole-mount spreadings and the quantification was carried out manually. However, a comprehensive quantification of transverse filaments requires their three-dimensional resolution. Therefore, one of the aims of this thesis was the generation of an electron tomography-based 3D model that allows for the automated quantification of the transverse filaments in their morphological context. In succeeding to generate this model, key metrics of the transverse filaments such as their number, density, length, and diameter were derived.

2. **The transverse filaments within the context of the lateral and central element** Transverse filaments consist of dimers of the protein SYCP1 in mammals. In mouse, SYCP1 consists of 979 amino acids that arrange into a central $\alpha$-helical coil and an unstructured tail at either site, i.e., at the N- and the C-terminus. The C-terminus localizes to the lateral element, while the N-terminus localizes to the central element. Since the entire central region spans only approximately 100 nm, the corresponding ends of the transverse filaments are hypothesized to be embedded within a lateral element and the central element. The localization of the N-termini of SYCP1 to the central element further imply a head-to-head assemble of the SYCP1 dimers that are associated with SYCP2 and SYCP3 of opposing lateral elements. So far, neither the degree to which the transverse filaments are embedded in the central and lateral element nor the precise arrangement of opposing transverse filaments in the central element have been resolved. The characterization of these topological aspects of the transverse filaments has the potential to enrich our understanding of the functional interaction of the transverse filament protein SYCP1 and the proteins

of the central and lateral element. Therefore, the 3D resolution and moreover quantification of the TFs' parts embedded within the LE and the CE on the basis of the ET derived 3D model of the SC was defined as an additional aim of this thesis.

3. **Multilayered organization of the transverse filaments** Early electron tomographic studies in *Blabs cribrosa*, *Drosophila melanogaster* and rat suggested a multilayered organization of the central element and the transverse filaments associated with it. In mouse, immuno-EM localizations of the transverse filament protein SYCP1 and the central element proteins SYCE1, SYCE2, SYCE3, and Tex12 suggested a bilayered organization of SYCP1 and SYCE3 with a single layer of SYCE1, SYCE2, and Tex12 in between. This hypothesis is supported by immunolocalizations of the respective proteins on murine spreadings imaged with *d*STORM. However, doubts remain about the layered organization of the CE and associated TFs due to limited epitope accessibility in the crowded environment of the multiprotein complex. As a third and final aim regarding the molecular architecture of the SC, this thesis attempts to address the hypothesis of a bilayered organization of the TFs in mouse by a computational analysis of the TFs organization in the 3D ET derived model of the SC. As the analysis did not show a layered organization, the TF organization was additionally examined using expansion microscopy, which confirmed the absence of a layered organization.

With regard to the architecture of the telomere attachments sites, the aim of this thesis was to answer the following open questions using electron tomography:

1. **Stoichiometry of LINC complexes at telomere attachment sites** LINC complexes in meiocytes concentrate at telomere attachment sites. Here, they transduce the forces generated by cytoplasmic motor proteins into the nucleus to move meiotic telomeres throughout prophase I. Their function and subcellular location suggest that they morphologically correspond to accumulations of filaments at telomere attachment sites that emanate from the inner nuclear membrane into the cytoplasm seen in EM micrographs. To enrich our understanding of the mechanisms through which LINC complexes contribute to the telomere movements essential to meiosis, again their 3D resolution and moreover quan-

tification is required. In the work presented here, the molecular identity of the superimposed filaments at telomere attachment sites was first confirmed to correspond to LINC complexes through immuno-EM. Next, to bridge the gap of missing 3D information on the LINC complexes, an ET derived model at telomere attachment sites of pachytene spermatocytes was generated. Based on this model, essential quantitative information on the LINC complexes, such as their number, length, and diameter were deciphered.

2. **LINC complex distribution at moving and steady telomere attachment sites** Meiotic telomeres move throughout prophase I at different velocities. Pachytene is characterized by a reduced rate of telomere movement compared to earlier meiotic stages. While the different rates of telomere movement and the types of motor proteins responsible for the movement have been investigated, little is known about the mechanisms behind the movement. Inferences about the mechanism behind telomere movement can be drawn from the molecular architecture of the telomere attachment site, specifically the distribution of the LINC complexes at these sites. Therefore, this work aimed to shed light on the distribution of LINC complexes at telomere attachment sites associated with the microtubule motor system using ET. The tomograms revealed the presence of a microtubule at certain telomere attachment sites and the corresponding absence at others, implying that the latter were immobile at the time of fixation while the attachment sites associated with a microtubule were moving. The tomograms of the presumably motile and immobile attachment sites were analyzed separately in order to detect differences in the number, shape, and distribution of the respective associated LINC complexes.

3. **First estimation of forces necessary to move a telomere attachment site** In mouse, the force necessary to move a telomere attachment site is generated in the cytoplasm by the microtubule motor system. Whilst, the speed and the types of telomere movement have been investigated, nothing is known about the amount of force that is required to move a telomere attachment site. In this work, the upper limit of the force required to actively move a telomere attachment sites was estimated by determining the maximum of dynein-dynactin complexes fitting on the section of a microtubule able to associate with the LINC complexes at a

telomere attachment site. As a result, this thesis provides the first estimation of the effective forces at telomere attachment sites.

# 2 Material and Methods

## 2.1 Animals

### 2.1.1 Mouse strains

Testis tissue samples used in this study were obtained from wildtype C57.6/J mice. The animals were either purchased directly from Charles River or were wildtype littermates of the *Sun1*$^{-/-}$ strain bred in the animal facility of the Biocenter of the University of the Biocenter of Würzburg. Animal care and experiments were conducted in accordance with the guidelines of the German Animal Welfare Act (German Ministry of Agriculture, Health and Economic Cooperation). Animal housing and breeding was approved by the regulatory agency of the city of Würzburg (Reference 821-8760.00-10/90 approved 05.06.1992; according to §11/1 No. 1 of the German Animal Welfare Act). The *Sun1*$^{-/-}$ strain originated from heterozygous mice kindly provided by K.T. Jeang [131]. Immunogold localizations were conducted either on 12-day-old C57.6/J mice or wildtype littermates of SPAG4 [132] housed and bred in the animal facility of the Biocenter of the University of Würzburg. Adult wildtype animals used in expansion microscopy experiments. Electron microscope tomograms were acquired of testes resected from 14-day-old mice.

## 2.2 Material

### 2.2.1 Chemicals

The chemicals used in this study were obtained from Merck, Sigma-Aldrich, Roth, Applichem, or Serva if not stated otherwise.

### 2.2.2 Antibodies

See Table 3 and Table 4.

### 2.2.3 Equipment

See Table 5, Table 6 and Table 7.

**Table 3:** Primary Antibodies

| Antibody | Host animal | Epitope | Manufacturer | Frozen sections | Chromosome spreads |
|---|---|---|---|---|---|
| SUN1 | guinea pig | 427-722 (mouse) | Seqlab, Goettingen | 1:150 | 1:300 |
| KASH5 | rabbit | N-terminal (mouse) 71-83 + 89-104 | Biotem, Apprieu | 1:100 | 1:200 |
| SYCP3 | mouse | full-length (gold hamster) | Abcam, Cambridge | - | 1:100 |
| SYCP3 | rabbit | C-terminal (human) | Novus, Wiesbaden | - | 1:200 |
| SYCP1 | guinea pig | N-terminal (rat) 1-124 | Seqlab, Goettingen | - | 1:100-150 |
| SYCP1 | rabbit | N-terminal (rat) 1-124 | Seqlab, Goettingen | - | 1:100-150 |
| SYCE3 | rabbit | full-length (mouse) | Seqlab, Goettingen | - | 1:150 |
| DCTN | rabbit | 140-210 (human) | Abcam, Cambridge | 1:50-1:300 | - |
| Dynein | mouse | - | Merck, Darmstadt | 1:50-100 | - |

**Table 4:** Secondary Antibodies. Diluted 1:200 in immunofluorescence localizations and 1:10 in immunoelectron microscopic localizations.

| Antibody | Antibody form | Host animal | Manufacturer | Product number | Experiment |
|---|---|---|---|---|---|
| SeTau anti-mouse | F(ab')2 Fragment | goat | - | - | U-ExM, MAP-ExM, MAP-RCM, triple localization LINC complex |
| Alexa568 anti-rabbit | Whole Antibody | goat | ThermoFisher | A-11036 | MAP-SIM, U-ExM, Unexpanded SIM, triple localization of LINC complex |
| Alexa488 anti-guinea pig | F(ab')2 Fragment | goat | Dianova | 106-546-003 | MAP-SIM, U-ExM, triple localization of LINC complex |
| Alexa568 anti-guinea pig | Whole Antibody | goat | ThermoFisher | A-11075 | Expansion LINC complex |
| Alexa488 anti-rabbit | F(ab')2 Fragment | goat | ThermoFisher | A-11070 | Expansion LINC complex |
| Alexa488 anti-mouse | F(ab')2 Fragment | goat | ThermoFisher | A-11017 | Pro-ExM, Unexpanded RCM |
| Alexa647 anti-rabbit | F(ab')2 Fragment | goat | ThermoFisher | A-21246 | Pro-ExM |
| 6 nm colloidal gold anti-guinea pig | Whole Antibody | donkey | Dianova | 706-195-148 | Immunogold localization |
| 6 nm colloidal gold anti-rabbit | Whole Antibody | goat | Dianova | 111-195-144 | Immunogold localization |

**Table 5:** Microscopes

| Microscope | Manufacturer | Camera | Laser lines | Objectives |
|---|---|---|---|---|
| Light microscope Laborlux S | Leica | - | - | - |
| TEM JEOL JEM-2100 | JEOL | TVIPS F416 4k x 4k,<br>Olympus Veleta 2k x 2k | - | - |
| SIM Elyra S.1 | Zeiss | sCMOS-Camera: PCO Edge 5.5 | UV: 405 nm,<br>VIS: 488 nm, 561 nm, 642 nm | 10x Dry, 63x Oil |
| Re-scan Confocal Microscope (RCM) | Nikon TiE | sCMOS, Andor Zyla 4.2P | Cobolt Skyra: 405 nm, 488 nm, 561 nm, 640 nm: 50 mW | 100x Oil, NA 1.49 Apo-TIR,<br>60x Water, NA 1.27<br>100x Siliconoil, 1.3 |

**Table 6:** Microscope slides and coverslips

| Microscope Slides, Coverslips | Manufacturer |
|---|---|
| Poly-lysine Slides | Menzel |
| Superfrost Plus | Menzel |
| Adhesive microscope slides HistoBond | Marienfeld |
| Microscopy Slides | Hecht |
| Coverslips 24 x 60 mm | Hartenstein |
| Precision cover slips 18 mm round | Roth |

**Table 7:** Equipment

| Equipment | Manufacturer |
|---|---|
| High Pressure Freezer EM HPM100 | Leica |
| Freeze substitution system EM AFS 2 | Leica |
| Multi Well Embedding Mold | Leica |
| Histo Jumbo Diatome | Diatome Ltd |
| Microtome EM UC7 | Leica |
| Razor blades | Wilkinson |
| Sputter coater Med 010 | Balzers Union |
| Centrifuge MIKRO 200/ MIKRO 200R | Hettich |
| Cryomicrotome 2800 Frigocut E | Reichert-Jung |
| Electrophoresis Power Supply | Peqlab |
| Gradient Thermocycler T100 | Bio-Rad |
| Heating block | Liebisch |
| Hybridisation Oven Mini 10 | MWG Biotech |
| Infinite M200 | Tecan |
| Peel-a-way tissue embedding molds | Plano |
| Stainless steel moisture chamber | Hartenstein |
| Dumont high precision tweezer No.7 | Dumont |

### 2.2.4 Primer

See Table 8.

**Table 8:** Primer for genotyping

| Identifier | Sequence (5'-3') | Annealing [°C] |
|---|---|---|
| Sun1KOP_1 | GGCAAGTGGATCTCTTGTGAATTCTTGAC | 62.2 |
| Sun1KOP_2 | GTAGCACCCACCTTGGTGAGCTGGTAC | 63.7 |
| Sun1KOP_3 | CAGGAGAAGAGTGAATGCCACCAGCTAC | 63.2 |
| Sun1KOP_4 | GGTGTGCACCACCACTGCTCCAAC | 64.3 |

### 2.2.5 Software

See Table 9.

**Table 9:** Software

| Software | Application |
|---|---|
| SerialEM | Tomogram acquisition |
| Etomo | Tomogram reconstruction |
| 3dmod | Tomogram segmentation |
| Zen | Image acquisition |
| Fiji | Image analysis |
| Inkscape | Illustration |
| Matlab | Data analysis |
| CLC Main Workbench | Data analysis |
| Solid Edge | Model generation |
| Virtualdub | Video generation |

## 2.3 Methods

### 2.3.1 Molecular methods

#### Genomic DNA preparation

- SDS Mix (pH 7.5)

  17 mM Tris/HCl
  17 mM EDTA
  170 mM Sodium chloride
  0.85% SDS

- Proteinase K

  20 mg/ml in 10 mM $CaCl_2$

- 6M sodium chloride solution
- 100% EtOH p.a., ice cold
- 80% EtOH p.a.

For the genotyping of wildtype, heterozygous and knockout mice, genomic DNA was extracted from ear punches. The latter were transferred to an Eppendorf tube containing 500 $\mu$l of SDS-Mix and 50 $\mu$l of Proteinase K per ear punch. The tissue digest was carried out in a hybridization oven overnight at 56°C while rotating. 250 $\mu$l of 6 M sodium chloride solution was added to each digest, followed by a rotation at room temperature for 10 minutes. The salted out digest was then incubated on ice for at least 15 minutes and subsequently cell debris, proteins and impurifications were pelleted for 8 minutes at 9000 rpm. 500 $\mu$l of the supernatant were transferred to a fresh Eppendorf tube. Next, the double amount of ice-cold 100% of EtOH (here: 1ml) was added in order to precipitate the DNA from the solution. The DNA was then pelleted at 14,000 rpm for 10 minutes. The supernatant was discarded and the DNA pellet washed two times with 80% EtOH. Washing steps were carried out by centrifugating the DNA in 1 ml 80% EtOH for 10 minutes at 14,000 rpm. After the second washing step, the DNA was dried at room temperature for several hours. Finally, the DNA was resuspended in 20 $\mu$l of water for 10 minutes at 60°C and stored at 4°C. The DNA concentration was determined from the ratio of absorbance at 260/280 nm using the Infinite M200

(Tecan).

**PCR amplification of genomic DNA**

In order to determine the genotypes of the SUN1 knockout strain offspring, wildtype or knockout alleles were amplified by polymerase chain reaction (PCR). The wildtype alleles were amplified using primers SUN1KOP_1 and SUN1KOP_3, resulting in an amplificate of 713 nt. For the knockout PCR Sun1KOP_2 and SUN1KOP_4 were used, resulting in an amplificate of 484 nt. Suitable annealing temperatures of the respective primers had been calculated prior to the present work with the $T_m$ Calculator web tool. The Phusion DNA polymerase was used because of its proofreading properties (5'-3' exonuclease activity) and its fast amplification speed (1000 bp per 15-30 s).

Phusion PCR reaction:

| | |
|---|---|
| 300 ng | genomic DNA |
| 1 $\mu$l | 5' primer (10 pmol/$\mu$l) |
| 1 $\mu$l | 3' primer (10 pmol/$\mu$l) |
| 10 $\mu$l | dNTPs (10 mM each) |
| 1.5 $\mu$l | DMSO |
| 0.3 $\mu$l | Phusion DNA polymerase |
| Add. | 50 $\mu$l $H_2O$ |

Thermocycler program for Phusion PCR:

| | |
|---|---|
| 2 min | 98°C |
| 20 sec | 98°C |
| 15 sec | 64°C |
| 40 sec | 72°C |
| 7 min | 72°C |
| $\infty$ | 12°C |

The number of cycles for denaturation, annealing, and elongation was 35x.

### 2.3.2 DNA electrophoresis

- 20x SB buffer (pH 8)

  200 mM NaOH

  pH adjusted to 8 using Borate

- Ethidium bromide (10 mg/ml)
- GeneRuler DNA Ladder Mix (Thermo Scientific)
- 6x DNA loading dye (Thermo Scientific)

PCR products were separated by size through DNA electrophoresis. Gels of 1% agarose gel (weight/volume) in 1x SB buffer containing 0.1 $\mu$g/ml ethidium bromide were cast. DNA samples were prepared for loading of the agarose gels by adding the respective amount of 6x DNA loading dye. The GeneRuler Mix from Thermo Scientific was used as a DNA size standard for electrophoresis. Gels were run at 190 V for 15-30 minutes in 1x SB buffer and DNA bands visualized under UV light for documentation.

### 2.3.3 KASH5 N-terminus peptide antibody design

In order to localize the N-terminus of KASH5, two short N-terminal sequences (around 15 amino acids) of the murine protein were selected as peptide epitopes for antibody generation. Peptide immunogens were hereby selected with the aid of CLC Workbench by taking several parameters into consideration. Domains potentially increasing cross reactivity through presence in other proteins as well as inaccessible regions occupied by alpha-helices and ß-sheets were avoided. A pool of the two respective peptides was used for the immunization of two rabbits. The antibody generation and purification was carried out by Biotem (Apprieu, France). The purity of the antibody was controlled in an SDS-PAGE by the company. It showed a single band around 50kDa in accordance with a rabbit IgG control that was run in the same gel.

### 2.3.4 Conjugation of SeTau-647-di-NHS to mouse F(ab)$_2$ fragment

F(ab)$_2$ fragments lack the constant region (F$_c$) of an IgG antibody due to digestion with Pepsin. Due to their smaller size, F(ab)$_2$ fragments provide increased localization precision, e.g., for immunolocalization. Fluorophores in this study were chosen

based on their photostability and brightness and their microscopic application. For structured illumination microscopy (SIM), Alexa 488 and Alexa 568 were chosen. A common red-emitting dye is Alexa 647. However, it is unsuited for photobleaching prone SIM, since it has poor photostability properties. A good alternative is ATTO 647N that has been shown to retain over 50% of fluorescence in expansion microscopy approaches compared to 10% of Alexa 647. ATTO 647N however introduced significant background due to unspecific binding. The best results of a red-emitting dye were achieved with the squaraine rotaxane dye SeTau 647 (SETA BioMedicals). At a very high photostability, SeTau 647 has extremely high quantum yields in aqueous buffers of up to 65% while introducing only little to no background. Therefore, SeTau 647 was conjugated to an anti mouse $F(ab)_2$ fragment. The $F(ab)_2$ fragment was incubated for 2 hours at 37°C with a 20x excess of SeTau 647 dye in 100 mM Borax buffer (pH 8.2) with gentle agitation. Since the $F(ab)_2$ fragment has an approximate size of 50kDa, 0.5ml 40kDaMWCO Zeba Spin desalting columns (ThermoScientific) were used for buffer exchange and removing small molecules ($<$ 2000 Da). After removing the column's bottom closure, the cap was loosened and the column transferred to a collection tube. The column was then centrifuged once at 1500xg in order to remove the storage solution. The flow-through was discarded and the column placed back into the collection tube. The 100 mM Borate buffer was added to the resin for equilibration of the column. Centrifugation at 1500xg and room temperature was repeated twice, the flow-throughs were discarded. After equilibration, the column was transferred to a fresh collection tube. A maximum of 200 $\mu$l of the conjugated antibody was added to the column. In order to retain the intact $F(ab)_2$ SeTau 647 conjugate, the column was centrifuged again at 1500xg. The flow-through containing the conjugated antibody was collected and the column discarded. The concentration of the protein and the degree of labeling (DOL) were calculated according to the Beer-Lambert law. The concentration of the conjugated antibody ($c_{\mathrm{Prot}}$) was calculated as follows:

$$c_{prot} = A_{prot}/\epsilon_{prot} = (A_{280} - A_{max} \times C_{280}) \times \epsilon_{max} \tag{1}$$

$$c_{Prot} = c_{prot} \times MW_{F(ab)2} \tag{2}$$

The DOL was calculated according to the following equation:

$$\mathrm{DOL} = \frac{A_{dye}/\epsilon_{dye}}{A_{prot}/\epsilon_{prot}} \tag{3}$$

with

$c_{prot}$: molar concentration of the protein

$A_{prot}$: absorbance of protein at 280 nm

$\epsilon_{prot}$: molar extinction coefficient [$M^{-1}cm^{-1}$]

$A_{280}$: absorbance at 280

$A_{max}$=$A_{dye}$: absorbance at $\lambda_{max}$ ($\lambda_{max}$: wavelength of the absorbance maximum of pure dye); SeTau 647: $A_{max}$=0.336

$C_{280}$: correction factor according to the spectral properties of the dye; SeTau 647: $C_{280}$= 0.12

$\epsilon_{max} = \epsilon_{dye}$: molar extinction coefficient [$M^{-1}cm^{-1}$] of the dye at maximum absorbance; SeTau 647: $\epsilon_{max}$=200,000 $M^{-1}$ $cm^{-1}$

$c_{Prot}$: concentration of protein [$g/l$]

$MW_{F(ab)2}$: molecular weight of the $F(ab)_2$ fragment = 110,000 g/mol

## 2.4 Microscopic Methods

### 2.4.1 Mouse tissue preparation

- 10x PBS

  1.4 M Sodium chloride

  26 mM Potassium chloride

  64 mM Disodium hydrogen phosphate

  14 mM Potassium dihydrogen phosphate

Wildtype C57BL/6 mice were euthanized using $CO_2$, followed by cervical dislocation. Testes were resected and transferred to PBS (diluted from 10x PBS throughout the study) before subsequent sample preparation was conducted.

**Frozen tissue embedding and sectioning**

Freshly resected testes were fixated for 1 hour in 1% FA either as a whole or cut in half

and afterwards washed with PBS for another hour. Testes were subsequently dehydrated in 15% sucrose until they sank to the bottom of the conical tube. Dehydration was reinforced by incubation two times with 30% sucrose, again each time until the tissue sank to the bottom of the tube. Dehydrated testes were transferred into Peel-a-way tissue embedding molds covered with a generous layer of Tissue Tek embedding medium. Testes were then quickly covered entirely with Tissue Tek and cooled to the temperature of liquid nitrogen using methylbutane as a liquid cooling fluid. The tissue was stored at -80°C, repeated thawing and freezing was avoided.

**Combined chemical fixation and high-pressure freezing for electron microscope tomography**

- Karnovsky fixative

  0.8 g Paraformaldehyde in 10 ml water
  25% Glutaraldehyde 2 ml
  0.2M Cacodylate buffer (pH 7.4) 8 ml

- Sodium cacodylate buffer 0.2M stock

  Sodium cacodylate 8.56 g
  Calcium chloride 25.0 g
  0.2N Hydrochloric acid 2.5ml
  Dilute to 200 ml with distilled water, pH 7.4

Freshly resected testes of 14-day-old mice were decapsulated and seminiferous tubules individualized. Tubules were transferred to Karnovsky fixative and fixated for 30 minutes at room temperature, followed by 30-60 minutes on ice. Individual, chemically (pre-)fixated tubules were placed in lecithin coated freezing platelets with 200 $\mu$m chamber depth (specimen carrier type A with 200 $\mu$m recess and the 0 $\mu$m side of type B carrier as a lid; Leica, Wetzlar) for subsequent high pressure freezing (HPF). The lecithin coating facilitates sample removal after HPF. Chamber recess is containing a thin layer of cryoprotectant 10% BSA in PBS. After adding the tubules to the chamber, the latter were covered with an excess amount of cryoprotectant to avoid air within the chambers. Samples were frozen to the temperature of liquid nitrogen at a cooling rate

of > 20,000 K/s and >2100 bar in an EM HPM 100 machine (Leica, Wetzlar). High pressure frozen samples were either stored in liquid nitrogen or immediately processed for electron microscope tomography by freeze substitution. Freeze substitution was carried out in an EM AFS2 freeze substitution system (Leica, Wetzlar) according to the freeze substitution protocol below (see Table 10). Care was taken that the samples never warmed up above -90°C throughout freeze substitution to avoid the formation of ice crystals that compromise the sample. Cups containing the freeze substitution mix were loosely covered with teflon lids to minimize gas exchange. All solutions were pre-cooled first to -80°C and then to the temperature of the AFS for 10-20 minutes in a spare container within the AFS before coming into contact with the samples. After freeze substitution, samples were embedded in epoxy resin within gelatine capsules or flat embedding molds and were cured for at least 48 hours at 60°C.

**Table 10:** Freeze substitution protocol

| initial temperature | final temperature | duration | solution | comment |
|---|---|---|---|---|
| -90 °C | | 96 h | 0.5 % glutaraldehyde + 0.1 % tannic acid in anhydrous acetone | exchange solution once |
| -90 °C | | 4-6 h | anhydrous acetone | 4 consecutive wash steps |
| -90 °C | | 28 h | 2 % OsO4 in anhydrous acetone | |
| -90 °C | -20 °C | 14 h | 2 % OsO4 in anhydrous acetone | |
| -20 °C | | 16 h | 2 % OsO4 in anhydrous acetone | |
| -20 °C | 4 °C | 4 h | 2 % OsO4 in anhydrous acetone | |
| 4 °C | | 2-3 h | anhydrous acetone | 4 consecutive wash steps |
| 4°C | RT | | anhydrous acetone | remove sample pellet from carrier |
| RT | | 5 h | 50 % epoxy resin in acetone | |
| 4 °C | | over night | 90 % epoxy resin in acetone | |
| RT | | 2-3 h | 100 % epoxy resin | |
| RT | | 2-3 h | 100 % epoxy resin | |
| RT | | 2-3 h | 100 % epoxy resin | |
| RT | | | 100 % epoxy resin | polymerisation for at least 48 h at 60 °C |

Prior to ultramicrotomy, spare epoxy resin covering the sample was trimmed away with a razor blade. Reaching the surface of the embedded sample, a trapeze containing the region of interest was cut into the epoxy block with the razor blade. From this section, 250 nm semi-thin sections were cut with a Diamond Knife (Diatome, Biel). Between 4-6 sections were then transferred to mesh or slot copper grids. Sections were contrasted with 2.5% uranyl acetate in dd$H_2O$ or EtOH and 50% Reynold's lead citrate. Both contrasting agents were sterile filtered (0.25 $\mu$m filter) and centrifuged for 5 minutes at 11,000 rpm prior to use. Lead citrate precipitates in the presence of carbon dioxide. Therefore, the water used to prepare the stain and used for rinsing was boiled prior to use. Additionally, the contrasting was carried out in the presence of sodium hydroxide pellets to generate a carbon dioxide-deficient environment. The grids were contrasted with 50 $\mu$l uranyl acetate (UA) for 10 minutes (2% UA in dd$H_2O$) to 15

minutes (2.5% UA in EtOH) in the dark, as UA is light sensitive. Grids were rinsed thrice with water (degassed) and left to dry before the second contrasting step with lead citrate. For the contrasting with Reynold's lead citrate, the parafilm on the glass plate was exchanged and a circle of sodium hydroxide pellets arranged in a circle. 50 $\mu$l of lead citrate per grid were placed inside the circle and grids placed on top with the sections facing down for an incubation time of 5 minutes after acqueous UA and 10 minutes following ethanolic UA. Sections were rinsed thrice with water (degassed) and left to dry completely. Grids were coated with a thin layer of carbon to avoid charging of the sections due to relatively long exposure to the electron beam during tomogram acquisition. Sections were incubated with guinea pig IgG coupled to 12-18 nm colloidal gold for 5 minutes on each side and rinsed with water in between and after the final incubation step. The antibody binds unspecifically to the mouse testes tissue and serves as fiducial marker for post acquisition tomogram reconstruction.

**Chromosome spreads**

- Hypertonic buffer (pH 8.2)

  30 mM Tris/HCl
  17 mM Sodium citrate
  5 mM EDTA
  50 mM Sucrose
  5 mM DTT (from 1M stock solution)

- 100 mM Sucrose (sterile filtered)

- 1% Formaldehyde solution (pH 9.2)

  1% (weight/volume) Paraformaldehyde solved in water through the addition of 15 $\mu$l Sodium hydroxide (sterile filtered) + 0.15% Triton X-100 (from 10% stock solution)

The content of meiotic nuclei was spread according to the dry-down method adapted from de Boer et al. [133]. Freshly resected testes were decapsulated and transferred into PBS. Seminiferous tubules were singularized in PBS and then transferred into hypotonic solution. Tubuli were left to swell in the hypotonic solution for 1-1.5 hours. Meanwhile, superfrost slides for the chromosome spreads were immersed in 1% formaldehyde

solution. On polylysine slides, a drop of 100 $\mu$l of sterile sucrose was placed, into which five tubuli were transferred. In order to retrieve the cells from the seminiferous tubules, the tubuli were minced in the sucrose with two fine tweezers. Additionally, cells were purged from the tubuli by repetitive resuspension with a 10 $\mu$l pipette. Next, the formaldehyde was drained from the superfrost slide except for a single drop that was collected at one corner of the slide. To this formaldehyde drop, 20 $\mu$l of chromosome spread was added and evenly distributed over the entire surface of the slide. Superfrost slides with fixated chromosome spreads were placed in a humidified chamber and dried down slowly first in the closed chamber for 2 hours, then overnight in the chamber left ajar and finally in the chamber without the lid until the chromosome spreads were completely dried down. Dried down slides were wrapped in tinfoil and stored at -80°C until use.

### 2.4.2 Immunolocalizations

**Immunogold localization**

For immunogold localizations, frozen sections of 6-10 $\mu$m were cut with a cryomicrotome. Sections were transferred to HistoBond slides and air dried for at least 60 minutes. Free aldehyde groups were blocked with 25 mM ammoniumchloride in PBS for 15 minutes. Sections were permeabilized with 0.05% of Triton X-100 in PBS for three minutes before unspecific epitopes were blocked in 1:1 10% goat serum and PBT for 1 hour. Incubation with the primary antibody was carried out for either one hour (KASH5) at room temperature or overnight (SUN1) at 4°C at respective concentrations. Sections were washed with PBS prior to incubation with the secondary antibody. Protocols differed whether the secondary antibody was conjugated to colloidal gold or nanogold.

For an incubation with a nanogold conjugated secondary antibody, the sections were incubated overnight at 4°C with a 1:100 dilution of the secondary antibody in PBT. After washing with PBS three times for five minutes each, the tissue was postfixed in 2% glutaraldehyde for 10 minutes. Sections were washed three times in PBS and four times in water. In order to visualize the nanogold for electron microscopy, the HQ Silver Enhancement Kit of Nanoprobes (Yaphank, New York) was used. The kit contains three components, namely an initiator (A), a moderator (B) and an activator (C), that need to be mixed at equal amounts. The nucleation of the silver enhance-

ment is temperature and time dependent. For the immunogold localizations in this study, an incubation time of 4 minutes in a 4°C climate chamber has been optimal. The reaction was stopped by washing with water (four times for five minutes each). Next, samples were further processed for electron microscopy at room temperature, if not stated otherwise. Sections were dipped in 0.05M cacodylate (diluted from 0.2M stock) in water before they were incubated with 1-2% osmium tetroxide in a moisture chamber for one hour. Samples were then washed twice for 5 minutes. Dehydration was carried out on ice in an ascending ethanol series (50%, 70%, 90%, 95% EtOH for 5 minutes each and twice with 100% EtOH for 5 minutes). In order to infiltrate the section with epoxy resin gradually, sections were incubated two times for five minutes with propylene oxide which mixes with the resin unlike ethanol. Tissue sections were incubated with a 1:1 mix of epoxy resin and propylene oxide for four hours at room temperature. Afterwards, sections were incubated with fresh undiluted epoxy resin overnight (RT). Finally, gelatine capsules without the lid were filled entirely with fresh epoxy resin, and placed inversely on the sections. Samples were cured for at least 48 hours at 60°C. Ultrathin sections of 65 to 90 nm were cut from the embedded samples with an ultramicrotome (Leica) and transferred to copper slot grids. Samples were contrasted for 15-20 minutes with 2% uranylacetate in ethanol, immersed once in 50% EtOH and thrice in water. Samples were further contrasted in 50% Reynold's citrate for 8 minutes, immersed thrice in water and dried completely prior to imaging at the electron microscope.

Immunogold localizations with a secondary antibody conjugated to colloidal gold were washed thrice with PBS after secondary antibody incubation and directly transferred to the 2.5% buffered glutaraldehyde solution. Samples were incubated with glutaraldehyde for 35 minutes and processed for electron microscopy in accordance with the steps described above.

**Immunofluorescence localization**

- Blocking solution I

  PBS

  5% milk

  5% fetal calf serum

- Blocking solution II

  1:1 10% goat serum and Blocking solution I

- Hoechst 33258 (end concentration 15 $\mu$g/ml in PBS)
- ProLong Glass Antifade Mountant

For immunofluorescence localizations, chromosome spreads were either prepared fresh or thawed from a stock stored at -80°C. In the latter case, slides were brought to room temperature before unwrapping them from tinfoil to avoid water condensation on the slide. Slides were washed thrice for five minutes in PBS within a glass cuvette. Unspecific epitopes were blocked with blocking solution I (after centrifugation at 16,000xg for 30 minutes at 4°C) or blocking solution II for localizations of a mouse derived primary antibody. For the blocking, chromosome spreads were incubated with 500 $\mu$l of blocking solution for 30 minutes in a humidified chamber. The primary antibody was diluted in blocking solution, centrifuged for 30 minutes at 16,000xg and 4°C and applied to the spreads for 1 hour at room temperature. Slides were washed three times for five minutes with PBS and again incubated with 500 $\mu$l of blocking solution I or II for 30 minutes. The secondary antibody was diluted in blocking solution I, centrifuged as described above and added to the spreads for 30 minutes. For the last 10 minutes of incubating with the secondary antibody, 50 $\mu$l of Hoechst were added to the spreads. Hoechst was not added for expansion microscopy (see below) immunofluorescence localizations. Finally, chromosome spreads were washed three times for five minutes in PBS and mounted overnight at room temperature with hard-setting ProLong Glass. After the mountant had set, slides were imaged within one week of preparation and stored at 4°C.

### 2.4.3 Expansion Microscopy Protocols

In this study, the expansion microscopy (ExM) variants protein-retention ExM (ProExM), magnified analysis of the proteome (MAP) and ultrastructure expansion microscopy (U-ExM) were performed on chromosome spreads of murine testes. Chromosome spreads were prepared as described earlier with the exception of using 18 mm cover slips instead of 60 mm x 24 mm objective slides. The smaller size of the cover slip results in a

small expanded polymer gel which in turn facilitates the localization of the synaptonemal complexes. Cover slips were cleaned with absolute ethanol and dried completely. To increase the adhesion of the chromosome spreads, cover slips were coated with 0.1 mg/ml poly-D-lysine for 1 hour and washed three times with $ddH_2O$ before chromosome spreading was carried out.

- 36.5-38% Formaldehyde (Sigma-Aldrich; F8775)
- Sodium acrylate (97-99%; Sigma-Aldrich; 408220)
- 8M Guanidine hydrochloride (Sigma-Aldrich;G7294)
- 40% Acrylamide (Sigma-Aldrich;A4058)
- 2% N,N'-methylenebisacrylamide (BIS;Sigma-Aldrich; M1533)
- PIPES (Sigma-Aldrich;P6757)
- Poly-D-lysine (Sigma-Aldrich;A-003-E)
- Proteinase K ($>$ 600U/ml;Thermo Fisher; EO0491)
- Ammonium persulfate (APS; Thermo Fisher; 17874)
- Tetramethyethylenediamine (TEMED; Thermo Fisher; 17919)
- 1-4% Formaldehyde solution
- Sodium dodecylsulfate (SDS)
- Triton X-100
- Tween-20
- Tris (Biosolve)
- Nuclease-free water (Ambion-Thermo Fisher; AM9937)
- TetraSpack Multispheres 0.1 $\mu$m fluorescent beads (T7279)
- BSA

**Table 11:** Monomer solutions for different expansion microscopy approaches

| Component | ProExM | | | MAP | | |
|---|---|---|---|---|---|---|
| | stock [%] | amount [ml] | final conc. [%] | stock [%] | amount [ml] | final conc. [%] |
| Sodium acrylate | 38 | 2.25 | 8.6 | 38 | 2.5 | 7 |
| Acrylamide | 50 | 0.5 | 2.5 | 40 | 0.921 | 20 |
| N,N'-Methylenebisacrylamide | 2 | 0.75 | 0.15 | 2 | 0.25 | 0.1 |
| Sodium chloride | 29.2 | 4 | 11.7 | 29.2 | | |
| PBS | 10x | 1 | 1x | 10x | 0.5 | |
| Water | | 0.9 | | | 0.329 | |
| **Total** | | **9.4** | | | **4.5** | |

To prepare 200 $\mu$l of gelation solution (see Table 11), 188 $\mu$l of monomer solution were mixed with 4 $\mu$l of 0.2% the accelerator TEMED and 4 $\mu$l of the initiator APS from 10% stock solutions. The gelation solution was brought up to 200 $\mu$l by adding 4 $\mu$l of water.

### Protein retention expansion microscopy (ProExM)

The ProExM approach is an adaptation of the original expansion microscopy protocol published by Boyden et al. [134]. Chromosome spreads were processed for immunofluorescence. After incubating the spreads with a conventional secondary antibody conjugated to a fluorophore instead of a DNA labeled secondary antibody for one hour in blocking buffer, spreads were washed four times for five minutes each with PBS. In order to link the antibodies into the polymer matrix, samples were subjected to an anchoring treatment. For the latter, chromosome spreads were incubated for at least 6 hours with 0.1 mg/ml AcyrloylX-SE in DMSO. After washing the spreads twice with PBS, samples were either stored at 4°C or processed for gelation. To gelate the samples, 80 $\mu$l of the respective monomer solution with 0.2% APS and 0.2% of TEMED was placed on a small plastic box covered with parafilm (in order to generate a hydrophobic surface) on ice. The chromosome spread was then quickly placed onto the gelation solution. Polymerization was carried out five minutes on ice and 1.5 hours subsequently at 37°C in the dark. After successful gelation, the polymer attached to the cover slip was transferred to a six-well plate containing 2 ml of digestion buffer supplemented with 8 unit/ml of Proteinase K. Samples were digested overnight at room temperature. In the process, polymers detach from the cover slip. The polymer was carefully transferred into large plastic culture dishes filled with $ddH_2O$ in order to wash out the digestion solution and subsequently expand the polymer. Gels were incubated in an excess of $ddH_2O$ for three to five hours whilst slightly shaking with an hourly exchange of the water. The size of the gel was determined once the gel expansion reached its plateau.

**Magnified analysis of the proteome (MAP)**

Opposed to the ProExM protocol, the magnified analysis of the proteome (MAP) variant of expansion microscopy is a post-labeling approach, meaning that immunolabeling is carried out after gelation. Chromosome spreads are prepared on 18 mm round cover slips as described in earlier. However, chromosome spreads are fixated in 4% formaldehyde (FA) in PBS supplemented with 30% acrylamide (AA). Chromosome spreads are dried down completely and either stored at -80°C or used immediately. The dried down (thawed) chromosome spreads are incubated for 4-5 hours at 37°C in an excess of fresh AA-FA solution. Without washing, samples were directly proceeded for gelation. Therefore, chromosome spreads were placed in 60 $\mu$l of MAP monomer solution supplemented with 0.5% APS and 0.5% TEMED on parafilm in a precooled humid chamber. The gelation solution was incubated for one minute on ice and an additional hour at 37°C in the dark. After successful gelation, polymers were immersed in 2 ml of denaturation buffer for 15 minutes at room temperature in a six-well plate. In case the gels did not detach from the cover slip automatically, they were carefully loosened with tweezers and transferred to a 2ml tube containing fresh denaturation buffer. Tubes were heated to 95°C for 30 minutes before gels were placed into large plastic culture dishes filled with an excess of $ddH_2O$ for washing initial expansion. Gels were washed at least twice for 30 minutes exchanging the water between washing steps. Gels were then reconstituted in blocking buffer (0.15 % BSA in PBS) twice for 30 minutes each, which resulted in them shrinking to approximately half of the expanded size before incubation with the primary antibody. A minimum of 500 $\mu$l of the respective primary antibody (mix) diluted in blocking buffer were incubated overnight at room temperature whilst shaking. Gels were washed thrice with blocking buffer for 10 minutes each and incubated with a minimum of 500 $\mu$l of the secondary antibody (mix) for at least 6 hours at room temperature while shaking. After two additional washing steps with PBST (0.1 % Tween-20 in PBS) for 30 minutes each, gels were expanded a second time by placing them in an excess of $ddH_2O$ for at least one hour, exchanging the water once after 30 minutes. Finally, gels were incubated in fresh $ddH_2O$ overnight until imaging.

**Ultrastructure expansion microscopy (U-ExM)**

The ultrastructure expansion microscopy (U-ExM) protocol is a modification of the post-labelling MAP protocol. The main difference between the two protocols is a

lower concentration of acrylamide and a higher concentration of sodium acrylate in the monomer solution (19% SA, 10% AA, 0.1% BIS-AA, 0.5% APS, 0.5% TEMED, 1× PBS). Testes cells were spread in the presence of 0.7% formaldehyde and 1% acrylamide. Dried down (thawed) chromosome spreads were incubated with 0.7% FA + 1% AA in PBS for 4-5 hours at 37°C. Afterwards, spreads were processed for gelation with the U-ExM monomer solution. Gelation, digestion, primary expansion, reconstitution and immunolabeling and final expansion were carried out in accordance with the MAP protocol with shorter primary and secondary antibody incubation times of 3 hours each.

## 2.5 Imaging

### 2.5.1 Transmission electron microscopy (TEM)

Transmission electron micrographs were acquired either at a Zeiss EM900 or a JEOL JEM-TEM2100.

The EM900 was operated at 80 kV and equipped with a 35 mm camera holding Kodak electron image SO-163 film. Since the JEM-TEM2100 used for this study is equipped with a 4k CMOS camera, photographic film provides higher sensitivity and resolution for immunogold localizations. The CMOS camera chip consists of an array of photon-counting transistors that translate into pixel. With a chip size of 63.5 x 63.5 $mm^2$ and a format of 4096 x 4096 pixel, each pixel has a size of 15.5 x 15.5 $\mu m^2$. The photographic film on the other hand consists of an emulsion of roughly 50 nm silver halide grains in a gel coating on a polymer film. Estimating an effective resolution or grain size of 3 $\mu$m, the pixel size for the 35 mm film (36 mm x 24 mm) would be equivalent to 12 000 px x 8000 px. Consequently, photographic film surpasses the resolution of a 4k CMOS camera chip. The film negatives were developed for 4 minutes in Kodak D-19 developer (diluted 1:2 with tap water). In the process, the rack was removed every 30 seconds from the developer tank and tilted slightly forward or backwards. The developer was rinsed off with tap water for one minute. Negatives were then placed in Kodak Fixer 1011 (GBXF; Hartenstein, Würzburg) for 4 minutes and washed with tap water for 5 minutes after fixation. Finally, the developed were left to dry before they were scanned with a resolution of 1000 dpi at an Epson Perfection V700 Photo Scanner using the SilverFastSE software.

Ultrastructural assessment of pachytene spermatocytes was performed at the JEM-TEM2100. Images were acquired either with the TemCam F416 (Tietz Video and Image Processing Systems, Gauting) or an Olympus Veleta 2k (Olympus, Münster) using the software EMMENU 4.0.9.31.

### 2.5.2 Electron microscope tomography (ET)

Electron microscopy tomograms were acquired at a JEM-TEM2100 transmission electron microscope (TEM) using a TemCam F416 (Tietz Video and Image Processing Systems, Gauting) with the software SerialEM. The TEM was operated at 200kV. Tilt series were acquired from -70° to 70° using the full mechanical range of the stage. For the tilt series acquisition, the limit on image shift was set to either 2 or 4 microns. After the initial tilt series was acquired, the specimen was removed from the TEM. The sample was rotated by 90° and reintroduced to the electron microscope for the acquisition of the second tilt axis.

### 2.5.3 Structured illumination microscopy (SIM)

Imaging of immunolocalizations on chromosome spreads was conducted with a Zeiss Elyra S1 microscope (Carl Zeiss Microscopy GmbH, Jena). For visualization of the fluorescence signal, the microscope was connected to an X-Cite 120PC Q Proprietary 120W Mercury Vapor Short Arc Lamp (Lumen Dynamics, Ottawa). The Elyra S1 is equipped with four laser lines: 405 nm, 488 nm, 561 nm and 642 nm. The specific instrument used for this study was connected to a PCO Edge 5.5 sCMOS camera. Imaging was carried out using a 63x/1.40 Plan Apo DICII M27 oil immersion objective for immunolocalizations on chromosome spreads that were embedded in ProLong Glass. For expansion microscopic immunolocalizations, the fluorophores are embedded in the aqueous environment of the hydrogel. In order to match the gel in refractive index, expansion microscopy samples were imaged with a C-Apochromat 63x/1.20 W Corr UV-VIS-IR M27 water immersion objective. The Elyra S1 used for this study houses a 6-position emission filter turret with single-bandpass filters. In order the turret is composed of an emission filter for transmission light, a triple-band filter, band pass filter (BP) 420-480 combined with long pass filter (LP) 750 (e.g., Hoechst), a BP 495-550/LP 750 (e.g., Alexa 488), a BP 470-620/LP 750 (e.g., Alexa 568) and a LP 655 (e.g., Alexa 647 or SeTau). Images were acquired in a scan format of 1280x1280

pixel (image size: 82.48 $\mu$m x 82.48 $\mu$m x 0.60 $\mu$m) at a camera exposure time of 100.0 ms. In order to take advantage of the post-processing improvement in resolution of SIM compared to traditional widefield microscopy and confocal microscopy, at least three planes with five rotations and five phase shifts were acquired. Gratings for the different laser lines were as follows: 405 - 34.0 $\mu$m; 488 - 28.0 $\mu$m; 561 - 34.0 $\mu$m; 642 - 23.0 $\mu$m. For image acquisition and processing, the Zeiss ZEN2 black edition 10.0 was used. After acquiring a stack of raw widefield images with the respective grating patterns, the higher frequency information in the images was reconstructed using the unmixing algorithm implemented in the ZEN software. The algorithm contains several reconstruction parameters aimed at minimizing artefacts in the reconstructed/post-processed super-resolution image. The main parameters are a Wiener filter ($w^2$=$10^{-v}$ $\equiv$ $w$=$10^{-v/2}$), apodization (frequency weighting; a distance transform $s$ is applied to the footprint $f$ of the OTF; $\tilde{A}(\overrightarrow{k})$=$[s(f(\tilde{h}(\overrightarrow{k})))]^{0.4}$, central frequency suppression (width of the Gaussian cannot be chosen) and modification of the system's optical transfer function (the user can choose between an experimentally or theoretically determined PSF; reconstructions in this study were based on a theoretical PSF). The reconstructed image was afterwards corrected for lateral drift and chromatic aberration caused by the optics of the microscope with the channel alignment tool of the ZEN software. For the channel alignment, diffraction limited multi-fluorophore beads were imaged under the same imaging conditions as the sample acquisitions (including SIM reconstruction). The underlying algorithm of the channel alignment tool is then calculating the xyz distance necessary to move each channel to line up with the assigned reference channel. Based on these distances, a correction table is generated that can be saved as a calibration file to align the channels in the sample acquisition according to the values of the correction table. The channel alignment tool of the ZEN software offers two alignment modes: lateral and affine. For this study, the affine mode was selected which corrects for linear lateral (x, y) and axuial (z) drifts, rotational offsets in the image plane in x and y (sx, sy) and the first order stretching in the image plane in x and y (sx, sy).

### 2.5.4 Re-Scan Confocal Microscopy (RCM), Direct Stochastic Optical Reconstruction Microscopy (*d*STORM)

Aside from the above mentioned structured illumination microscopy, expansion microscopy samples were also imaged with re-scan confocal microscope (RCM). SIM acquisitions were conducted by Marie-Christin Spindler and Fabian Zwettler of the Department of Biotechnology and Biophysics. LSM, RCM and *d*STORM images were acquired by Fabian Zwettler and Andreas Kurz (RCM), also from the Department of Biotechnology and Biophysics. *d*STORM reference images were acquired by Katharina Schücker and Thorge Holm. To provide background on these acquisitions, also *d*STORM will be explained briefly.

Re-scan confocal microscopy provides a resolution in between diffraction limited microscopy and SIM of 170 nm laterally. The 1.4 fold increase in resolution is achieved by re-scanning the emission light after the pinhole (optomechanical pixel reassignment; pinhole diameter: 50 $\mu$m). The rescanning unit (Confocal.nl) is hooked up to the side port of a Nikon TiE with a motorized stage. The laser unit Cobolt Skyra (Cobolt, Hübner Group) with laser lines 405 nm, 488 nm, 561 nm and 640 nm (each 50 mW) is fiber coupled and connected to the RCM unit. Imaging is performed with a 60x/1.27 CFI Plan Apo water immersion objective (Nikon, Amsterdam). The signal to noise is improved twofold in comparison to traditional confocal microscopy due to the replacement of a photomultiplier tube (PMT) with an sCMOS camera (Andor Zyla 4.2P, Oxford Instruments, Wiesbaden). The RCM was controlled with the NIS-Elements version 4.6.

*Direct* stochastic optical reconstruction microscopy (*d*STORM) was performed using an inverted Zeiss Axio Observer.Z1 (Carl Zeiss Microscopy, Jena) equipped with a 63x/1.15 W Corr M27 water immersion objective (Carl Zeiss Microscopy, Jena). The sample was illuminated with a 640 nm diode laser (iBeam smart, Toptica Photonics) in epifluorescence configuration. For 3D acquisitions, a cylindrical lense was introduced into the light path. Imaging was carried out at 20,000-40,000 frames on an EM-CCD camera (Andor Ixon Ultra DU897U-CSO) operated at a frame rate of 50-80 Hz. Zeiss's Definite focus was used to maintain focus during acquisition. In order to activate the photoswitching properties of the fluorophores, samples were imaged in an oxidizing and reducing buffer system (ROXS) consisting of 100 mM cysteamine hydrochloride in PBS (pH 7.5) that was supplemented with an oxygen scavenger system (2% glucose (w/v),

2 U/ml glucose oxidase and 200U/ml catalase) for the single color experiments. Data processing was performed either with the Fiji plugin ThunderSTORM (single plane acquisition) or the open-source software rapidSTORM3.3 (z-stack).

## 2.6 Data processing and analysis

### 2.6.1 Tomogram reconstruction

Dual-axis tilt series were reconstructed into tomograms with Etomo of the IMOD software suite. Since the program was written for Unix-like systems, such as Linux, a compatible environment is required for the program to run on a Microsoft Windows distribution while avoiding source code modifications. Cygwin contains a large collection of GNU and open-source tools that provide a Unix-like environment on Windows. Therefore, it was used as a command-line interface tool for opening etomo as well as 3dmod of the IMOD software suite. The IMOD software suite programs further require a Java run-time environment. In order to reconstruct a tomogram, Etomo was started with the command *etomo* in the command-line interface of Cygwin. This command initializes a *front page* panel with several options, of which *build tomogram* was selected that opens the *Setup tomogram* panel and a *Project Log*. The *Project Log* saves the history of actions and reports errors. After selecting the .st file of one of the axis of the dual axis tilt series, the *plasticSection.adoc* system template was selected. The IMOD template is targeted at setting optimum parameters for the reconstruction of plastic embedded sections. It activates a Sobel filter to achieve better centering when tracking fiducials and sets a default size of patch tracking. Depending on whether one or two tilt axes were recorded, either single or mostly dual axis was selected. Next, the header containing the tilt series metadata was scanned for pixel size. The tomograms were acquired at a magnification of x40,000 with a 4K camera (TVIPS TemCam F416; Tietz Video and Imaging Processing Systems; Gauting, Germany), resulting in a pixel size of 0.287 nm. Scanning of the header further defines the Image rotation, which was -2.7 for the tomograms acquired for this study. In the next step, the fidual diameter was set to either 12 nm or 18 nm, as the unspecific guinea pig IgG was coupled to either 12 nm or 18 nm colloidal gold. The Image distortion field file and Mag gradient correction were left blank for the reconstructions of this thesis. The tilt angles were extracted from the extended header of both axes. The raw image stacks were checked for image

quality before com scripts (*Create Com Scripts*) were generated which opens up the Etomo main window. The process control buttons on the left side of the main window enable the user to select the subsequent steps of tomogram reconstruction. In the first step of pre-processing, x-ray artefacts collected by the CCD camera which result in extremely high and low pixel values are corrected for by selecting *Show Min/Max for Raw Stack* which runs the program clip stats that displays the minimum and maximum densities for the individual slices of the image stack. By selecting *Create Fixed Stack* a program called ccderaser is run. Ccderaser detects x-rays by comparing pixel values with regard to a set of criteria (Peak criterion that detects extreme pixel values by means of SDs, Difference Criterion that detects pixel-to-pixel differences exceeding a background by a number of SDs both required to fall below the set Maximum radius and additionally the Extra-large difference criterion that removes artifacts exceeding the Maximum radius) which were kept at default values, corrects for the detected artifacts and generates a new fixed image stack for further processing. After examining the contrast in the fixed stack, *Use Fixed Stack* was selected to continue with the coarse alignment of the images. The initial *Calculate Cross-Correlation* command was executed to run the program Tiltxcorr which cross-correlates two successive images for an initial translational alignment. These initial alignments are transformed into a "global" set of alignments which are applied to the image data creating a prealigned stack by choosing *Generate Coarse Aligned Stack*. In the next step, a fiducial model was generated based on the positions of the colloidal gold on the section imaged at each tilt angle. To start generating the fiducial model, "Make seed and track" was selected which allows to select fiducials on one section, add undetected fiducials manually and track fiducials throughout the stack from this initial selection. For generation of the initial fiducial model, the center of the colloidal gold was refined with a Sobel filter and the total number of fiducials on the section entered. Since both sides of the section were incubated with the unspecific IgG conjugated to colloidal gold, "Select beads on two surfaces" was selected. The initial fiducial model was generated on one section upon selecting *Generate Seed Model*. The Project Log window is reporting the number of fiducials detected with the beads on the top and bottom surface marked up with different colors. In order to use this initial fiducial model as a seed to trace the fiducial marker throughout the entire stack, *Track Seed Model* is selected in the Track Beads tab which runs the Beadtrack program. The number of gaps of where

fiducials could not be automatically tracked in a continuous manner are indicated in the Project log window and were corrected for manually in the prealigned stack by selecting *Fix Fiducial Model*. Next, the prealigned stack was fine aligned. Therefore, the general alignment was computed by selecting *Compute Alignment* which runs the program Tiltalign. Tiltalign corrects displacements, rotations, tilts and differences in magnification in the stack. The best fit is computed by applying a variable metric minimization approach to the gold fiducial positions. In the Project Log Window the ratio of total measured values to all unknowns, the mean of the residual error and the respective standard deviation are reported. The residual error reflects the distance in pixel between the position of a fiducial and the prediction of this position by the alignment solution. A visual representation of the residual model vector expanded by factor 10 was assessed by pressing *View Residual Vectors*. If the model showed large displacements, local alignments were performed iteratively. Therefore, the *View/Edit Fiducial Model* was selected to open the Bead Fixer dialog box with the "Fix big residuals" option checked. Model points with big residuals were navigated by clicking on "Go to Next Big Residual" and corrected for by the recommended amount determined through a mathematical alignment model that aims at fitting all model points by selecting "Move Point by Residual". After saving the model, the total tilt angle change was obtained from the alignment log file under the "Surface Angle" tab and entered in the "Fine Alignment Volume Position Parameters" box as the "Total tilt angle offset". By selecting *Compute Alignment* again the alignment was computed considering the corrections. The fiducial model was checked by clicking the *View 3D Model* button in the Fine Alignment dialog. For models with a decent distribution of (non-clustered) fiducials on both sides, the data was solved for distortion by navigating to the "Global Variables" tab and checking the full solution option as a distortion solution type to solve for X-axis stretch and Skew distortion. An alignment solved for distortion was computed by hitting the "Compute Alignment" button again. Solving for distortion can introduce new residuals. Therefore, the mean residual error was assessed in the Project Log and residual errors corrected for as described above if necessary. As the last operation before reconstructing the tomogram the data set was sampled to create three small reconstructions that are shifted and rotated in order to reconstruct the smallest possible tomogram volume in the *Tomogram Positioning* step. The Positioning tomogram thickness was herefore set to 1000 for the 250 nm sections used in this

study and three sample tomogram slices from the top,middle and bottom of the tilt image stack were generated by pressing *Create Sample Tomograms*. In order to define the top and the bottom of the section in each of the three sample reconstructions, *Create Boundary Models* was selected. This command opens the main image display and model editing Zap window. The boundaries of the section can be set by placing two model points at opposite sites of the top surface which will be automatically connected with a line and setting the boundary for the bottom surface accordingly. After setting the boundaries for the three model reconstructions, the model was saved and the *Compute Z Shift and Pitch Angles* was selected to initiate the program tomopitch that determines parameters that will result in the smallest possible reconstructed tomogram volume. Tomopitch enters the "Final tomogram thickness" to the *Tomogram Positioning* dialog with an additional 10 pixel by adding 5 pixel on each side of the reconstruction boundaries as specified in the "Added border thickness" option. The final alignment was computed by pressing *Create Final Alignment*. The resulting alignment transforms were applied to the entire stack by selecting *Create Full Aligned Stack* and the tomogram axis was recreated by pressing *Generate Tomogram*. For the second axis, the Pre-processing step and the Coarse alignment were carried out accordingly. For the following Fiducial Model Generation the seed model was created using the program Transferfid that is run by selecting *Transfer Fiducials From Other Axis* and transfers the fiducials from the first axis to the corresponding views of the second axis. If fiducials were not transferred accordingly, they were added manually by selecting "add points to seed model automatically". The alignment was then carried out as outlined above for the first axis resulting in a reconstructed tomogram of the second axis. In the final step of tomogram generation, the two axes were combined by matching the B tomogram to the A, e.g., matching the second axis to the first in the tomogram combination panel. For the initial matching parameters "Fiducials on both sides" were selected. In the patch parameter section for refined alignment the "Use Automatic Patch Fitting" box was checked that increases the patch size based on available information. In order to only use the ranges of the volume that contain the highest quality of image data to match up the two axes, the both volumes were examined by pressing *3dmod Volume A* and *3dmod Volume B* and the x, y, and z range adjusted accordingly. In most tomograms the x and y range was left at default settings and only the z range was adjusted. Finally, tomogram assembly is initiated by first

selecting *Create Combine Scripts* and then *Start Combine*, ultimately resulting in the final reconstructed dual-axis tomogram.

### 2.6.2 Tomogram segmentation and data processing

**Tomogram segmentation** The manual segmentation of the structures of interest was carried out using the drawing tool plugin of 3dmod. The plugin offers a list of different drawing tools of which the normal and the sculpt tool were selected to carry out the segmentation of the structures of interest in this work. The normal mode allows the user to segment the structures by adding model points to a contour with a normal contour drawing behaviour. The sculpt tool is suited for quick drawings with a sculpt circle that generates a closed contour that can also be used to mold the contour from the outside or the inside. To start the segmentation, a new object was added to the model (Menubar > Edit > Object > New). Depending on the structure of interest, either a closed or an open type of contour was selected. Closed contours are suited for complex objects and consist of polygons that reside only in one virtual slice. In the present work, the nuclear envelope, the central and the lateral element were segmented as closed contours using the sculpt tool. Since the structures do not reside in a single plane, they were segmented every 10-50 slices depending on the frequency in morphological changes of the specific structure. The resulting individual segmentations in the different z-planes were interpolated by using the interpolation plugin of 3dmod to connect the manually drawn contours. Linear interpolation was chosen as an interpolation type which generates contours with straight lines between the manually drawn contours. In order to determine the three-dimensional surface of the segmented structure, the contour data was given a skin that consists of a mesh of triangles which is conducted with the help of the meshing panel which is part of the objects dialog box of 3dmod. For the filamentous LINC complexes and the transverse filaments of the SC, the open countour type was selected. Here the end of the contour is not re-connected to its beginning making it is well suited to trace filamentous structures over multiple virtual sections using the normal drawing mode. The center of the microtubules was also segmented as an open contour using the normal drawing mode. In order for the diameter of the microtuble to correspond to the commonly accepted diameter of 25 nm, they were meshed with the tube diameter set to 25 in the objects dialog box of 3dmod. The segmentation was monitored in the XYZ window which

provides additional XZ and YZ views in addition to the Zap window that displays the XY view. The leading criterion for segmentation was the continuity of structures in 3D.

**General data processing** The average length, number per tomogram and width of both LINC complex and transverse filaments was determined using 3dmod [135]. For the calculation of average length and number per tomogram, the 3dmod tool `imodinfo` was used and the width was determined using the measure option of the 3dmod `drawingtools`. Next, the `model2point` command-line tool was used to derive a file containing the segmented structures as lists of 3D points. These files were analyzed separately using custom MATLAB scripts for the LINC complex data and the transverse filament data.

**LINC complex data processing** The point of origin of each LINC complex was assigned as the point where it intersects with the inner nuclear membrane. The minimum distance between these points of origin was determined for each point of origin as the minimum of the euclidean distances to all other points of origin. To approximate the LINC complex density, for each lateral element, a plane was fit through all points of origin of the LINC complexes associated with this lateral element using principal component analysis. Based on the smallest and largest values of the translated filament x/y-coordinates, the plane was reduced to the smallest rectangle containing all points of origin. The density was defined as the number of LINC complexes in the rectangle divided by its area. The dimension of this rectangle was also used to derive the maximum number of dynein–dynactin complexes that can interact with the LINC complexes associated with a lateral element at the same time. The longer of the two sides of the rectangle was used as an approximation of the area on the microtuble on which dynein-dynactin complex can interact with the LINC complexes. To determine the maximum number of motor complex that could fit this area, the latter was divided by the dimensions of the dynein-dynaction complex. Lastly, the closest euclidian distance between LINC complexes over their entire length was calculated for each LINC complex by deriving the minimum of the distances of each point of this LINC complex to every point of every other LINC complex.

**Transverse filament data processing** In a first step, the intersection points with the lateral element and central element were defined for each transverse filament as the transverse filament point with the lowest distance to the lateral/central element. Based on these intersection points, the indentation of the transverse filaments into the lateral and central element was determined as the distance between the intersection point and transverse filament endpoint in the lateral/central element. The length of the transverse filaments in the central region was determined as the distance between the lateral element intersection point and the central element intersection point. The width of the central region, the central element width and the distance between central element and lateral element were calculated as the mean over the minimum distance between the respective intersection points. The minimum distance between transverse filaments in the lateral element was derived for each transverse filament as the minimum distance between its endpoint and the endpoints of all other transverse filaments. The minimum distance of transverse filaments in the central element and between transverse filaments of the opposite side within the central element was calculated accordingly. The density of the transverse filaments was calculated similarly to the LINC complex density. First, a plane was fitted to the end points using principal component analysis. Next, the plane was reduced to the smallest rectangle containing all end points and finally the density was calculated by dividing the number of end points in the rectangle by its area. As a test for a layered organization, two planes were fitted to the transverse filament points, so that the orthogonal distance sum of the filament points to the closest plane was minimized. This was implemented based on an open-source MATLAB function by Adrien Leygue [136], which performs the plane fitting based on the filament points eigenvectors.

# 3 Chapter I: (Ultra)structural preservation of spermatocytes for EM tomography (ET)

**According to Spindler *et al.* 2018 [137].**

The aim of this work is to unravel the molecular architecture of the SC and the LINC complexes in order to uncover their individual structure-function relationship. Electron microscope tomography (ET) is a powerful technique to resolve the molecular architecture of 3D multiprotein complexes with subnanometer lateral and 3-4 nm axial resolution within their morphological context. Yet, even under optimal imaging conditions, the prerequisite to resolving fine structural details is the preservation of the respective tissue. Testis tissue has two special characteristics that require consideration in sample preparation for ET. Firstly, the tissue connectivity in seminiferous tubules is solely maintained by cell-cell contacts of varying strength between Sertoli cells and the hierarchically organized developmental stages of germ cells. With the aim of releasing mature sperm into the lumen of the seminiferous tubule, the gradient of cell-cell contact strength is weakest near the lumen [138]. In this study, 14-day-old, wildtype C57BL/6J were used for the generation of ET derived 3D models. At this age, meiocytes of male mice undergo the first wave of spermatogenesis where the cells progress almost synchronously through the testis and early to mid-pachytene spermatocytes are enriched. As a consequence, individual tomograms of pachytene spermatocytes of respective mice are directly comparable. At the same time, the spermatocytes are the cells closest to the lumen in this context and therefore manifest the weakest cell-cell contacts with the supporting Sertoli cells in this context. The second special characteristic of meiocytes is the composition of their nuclear lamina. Here, somatic lamins A, C, and B2 are replaced by lamin B1 and, more importantly, lamin C2, a splice variant of lamin A. Lamin C2 forms a discontinuous lamina that provides higher flexibility needed for the telomere movements throughout prophase I [57]. The sum of these special characteristics of testes tissue must be taken into account in sample preparation for ET of SCs in murine pachytene spermatocytes. Therefore, as a starting point for this work, three different sample preparation approaches for ET (high-pressure freezing and freeze substitution, classical chemical fixation and dehydration at 4°C as well as a hybrid approach of chemical fixation and freeze substitution after high-pressure

freezing) were compared in order to achieve optimal (ultra)structural preservation in subsequently acquired electron tomograms of the SC and LINC complexes at meiotic telomere attachment sites.

## 3.1 Chemical fixation and freeze substitution after high-pressure freezing result in optimal structural preservation of pachytene spermatocytes of the mouse

State-of-the-art high-pressure freezing followed by freeze substitution has been documented to result in near-native structure preservation [139]. Therefore, seminiferous tubules were first processed by HPF and freeze substitution under optimized conditions for testis tissue, as described below. Although the high-pressure freezing preceding the freeze substitution theoretically allows for vitrification of samples that are up to 0.6 mm in diameter, samples should be prepared as thin as possible to prevent ice crystal formation [140]. Samples of up to 200 $\mu$m in thickness achieve acceptable results [141]. The tubule diameter of 14-day-old black six mice is only roughly 100 $\mu$m [142]. Sufficient sample tissue was placed in freezing platelets and the recess was overfilled with freeze protectant to avoid air bubbles. 10% BSA was chosen as a freeze protectant since it has a similar osmolarity to that of the rete testis fluid within the testis [143]. The high-pressure freezing settings were originally optimized for a correlative light and electron microscopy (CLEM) approach. In order to preserve the antigenicity of the samples for CLEM, a different freeze substitution mix is used and samples are embedded in LR white instead of epoxy resin after HPF. The HPF itself is however carried out in the same way for the CLEM approach and the morphology protocol used in this study [144]. Unfortunately, even under these optimized conditions, submitting the 14-day-old seminiferous tubules to high-pressure freezing, resulted in a large number of meiocytes being ejected out of the tissue (not shown). In the few remaining spermatocytes, the discontinuous lamina was (apparently) unable to withstand the high mechanical pressure of the vitrifying method, causing the nuclear content to detach from the nuclear envelope, thereby distorting the nuclear architecture (Figure 4).

In contrast, classical chemical fixation stabilizes the tissue through cross-linkage of proteins by aldehyde and glutaraldehyde fixation. Using this approach, the spermatocytes

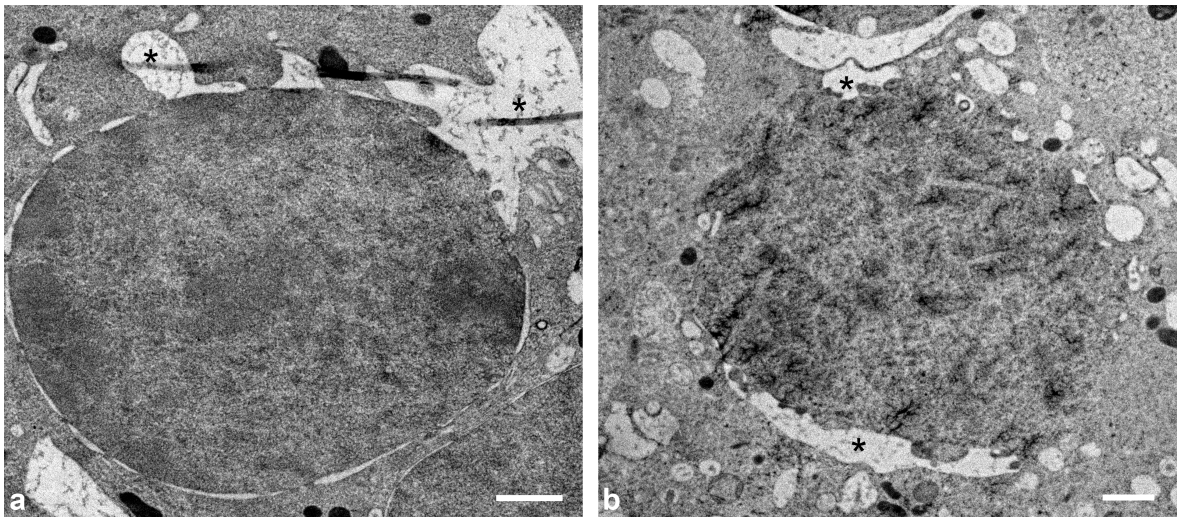


**Figure 4: Ultrastructural preservation of high-pressure frozen pachytene spermatocytes of 14-day-old wildtype mice.** a,b. Ultrathin sections of pachytene spermatocytes after high-pressure freezing and freeze substitution. Nuclei are detached from the inner nuclear membrane (asterisks) or ejected from the tissue entirely (not shown). Additionally, the chromatin is affected by ice-crystal induced artifacts. Scale bars: 1 $\mu$m. Figure adapted from [72, 90].

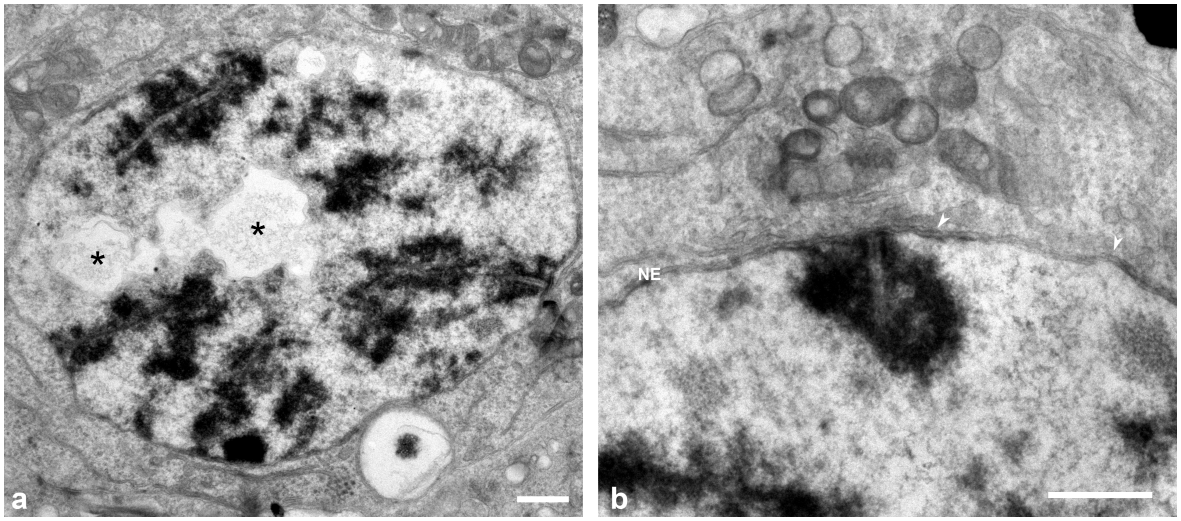


**Figure 5: Ultrastructural preservation of murine spermatocytes after chemical fixation and dehydration at room temperature.** a. Electron micrograph of pachytene spermatocyte after chemical fixation and dehydration at room temperature. The nucleus appears extracted and shows holes due to poor resin infiltration and polymerization. b. Telomere attachment site showing the synaptonemal complex of a pachytene spermatocyte after chemical fixation and dehydration at room temperature. The nuclear envelope shows an irregular spacing likely introduced by the dehydration at 4°C (arrows). Scale bars: 1 $\mu$m. [90].

were kept from being ejected out of the tissue, however at the cost of introducing shrinkage artefacts related to the dehydration at 4°C ( Figure 5). One very prominent effect of dehydration at 4°C or room temperature is the loss of physiological spacing between the nuclear envelope [145, 146]. Here, instead of a regular spacing of approximately 45 nm, the perinuclear space (PNS) of the spermatocytes showed an inconsistent spacing of the PNS due to the sample shrinkage (see Figure 5). The inconsistent spacing of the

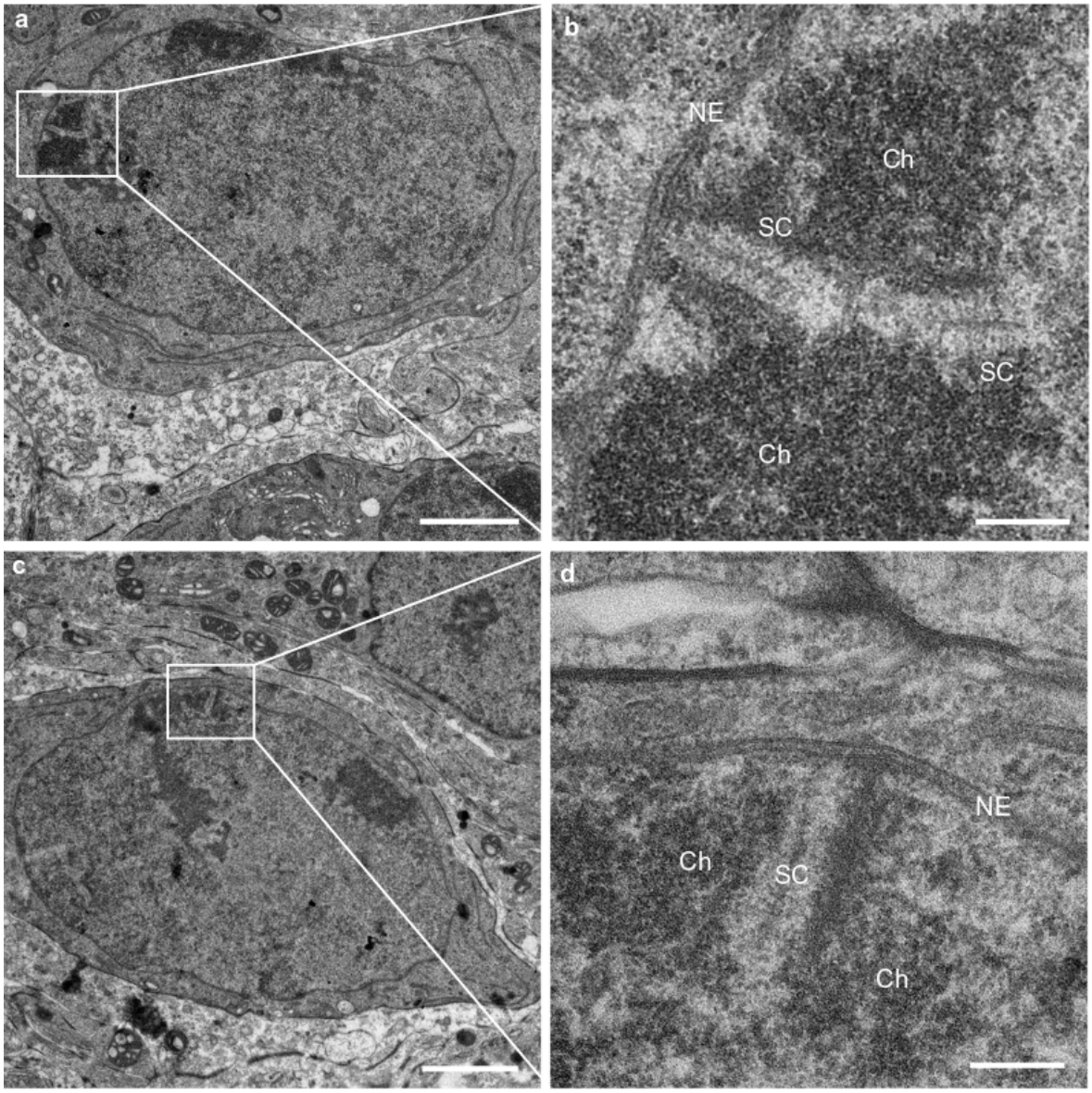


**Figure 6: Ultrathin sections of chemically fixated and freeze substituted (after HPF) testis tissue of 14-day-old mice.** a,c. Pachytene spermatocyte with synaptonemal complex (boxed region) attached to the nuclear envelope. b,d. Tripartite synaptonemal complex (SC) and associated chromatin (Ch) attached to the nuclear envelope (Magnified views of boxed regions of a and c respectively). Note the consistent spacing of the nuclear envelope. Scale bars: a,c. 2 $\mu$m, b,d. 200 nm. Figure adapted from [72, 90].

nuclear envelope inherently affects the associated multiprotein complexes and deems subsequent quantitative measurements unreliable. Consequently, classical chemical fixation was also unsuited for studying the LINC complexes (and transverse filaments of the SC).

In order to simultaneously preserve the tissue/cell integrity as well as the ultrastructure of the testis tissue, an approach of chemical fixation, followed by high-pressure freezing and freeze substitution was established in this work [137]. The protocol is based on

a similar approach published by Dhanyasi et al. [147]. Freeze substitution starting at -90°C results in far less extracted ultrastructure while the preceding chemical fixation stabilizes the tissue. Using this approach, the nuclei appeared less extracted and, moreover, the perinuclear space showed a continuous spacing (Figure 6). Since this hybrid approach of chemical fixation and freeze substitution after high-pressure freezing resulted in excellent (ultra)structural preservation, it was used for the preparation of ET samples in this study.

## 3.2 Post-processing evaluation and correction of reconstructed tomograms

For representative feature extraction and quantification, the acquisition of 5-8 tomograms is recommended [139, 148]. In the present work, six (synaptonemal complex study) to eleven (LINC complex study) tomograms were acquired. These tomograms were pre-selected for quality and completeness. They were reconstructed from dual-axis tilt series of 250 nm semi-thin sections. Synaptonemal complexes have a maximum extend of 400 nm in width and 200 nm in depth at telomere attachment sites and 200 nm by 100 nm in the interstitium. Therefore, each 250 nm section fits the dimensions of an entire synaptonemal complex (SC). To capture the entire structural information of a tissue section requires the acquisition of 360° of the volume in 1° increments. To date, the mechanical tilting stages of transmission electron microscopes are limited to 140 degrees (-70° to 70°), covering 141 angles at 1° increment acquisition. The respective information that would be provided by the missing angles is referred to as the missing wedge. The latter can be reduced to a missing pyramid by acquisition of a corresponding second tilt axis for which the sample is rotated by 90°.

A good way to evaluate artefacts or missing information in the reconstructions (caused by the "missing pyramid") is to examine the fiducial marker in xy/xz/yz. Common indicators of missing information from high-tilt angles are ray artefacts and elongation of the gold particles in the reconstruction due to unsampled high-tilt information in Fourier space [149]. Therefore, the missing pyramid artefacts of the fiducials were visually examined for halos and elongation or streaking artefacts.

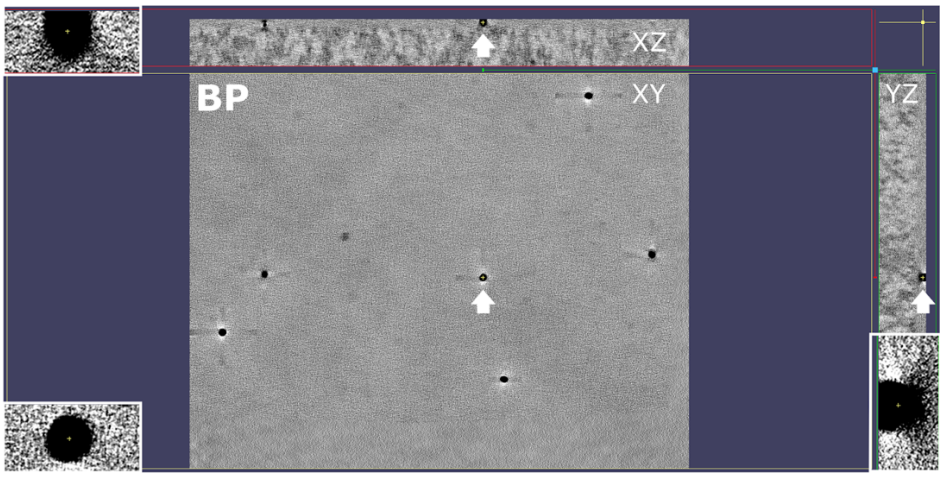


**Figure 7: XY-slice (middle plane), XZ-slice (top plane) and the YZ-slice (right plane) that intersect at the same gold marker (arrow) for one of the tomograms.** The reconstructed tomogram shows minor artefacts caused by the missing pyramid indicated by a small halo around the gold particle and an elongation in the axial direction. Minimum ray artefacts are apparent in the YZ-slice.

Figure 7 shows the XY-slice (middle plane), XZ-slice (top plane), and the YZ-slice (right plane) that intersect at the same gold marker for one of the tomograms used in this work. The gold marker shows only little halo artefacts, and appears round with the slightest elongation in the Z direction (XZ view). The YZ-slice indicates minimal ray artefacts. Overall, the reconstruction appears barely affected by the missing wedge problem. BP abbreviates back-projection, the algorithm used to reconstruct the tomogram.

During the acquisition of electron tomograms, the electron beam causes significant thinning of the sample. In order to ensure to scale feature extraction, the reconstruction was therefore corrected for the respective thinning of the specimen and additionally for potential curvature. The axial extent of the reconstructions was assessed by measuring the amount of pixel the sectioned material occupied in the axial direction (XZ view) with the measuring tool of the IMOD software suite that was used for acquisition, reconstruction, and segmentation. The measurement was repeated in different sections of the z stack and the average result was used to determine the Z-scale. As mentioned earlier, the reconstructions were based on 250 nm semi-thin sections. So, for example, for an extent of 558 pixel of the reconstructed material, and an isotropic pixel size of 0.287 nm, the program reports 160 nm. This means that what was originally 250 nm had thinned to 160 nm by the time the tilt series was taken. Hence, for this example, which is reflective of the whole set of acquired tomograms, the resulting z scale was

1.56. For the epoxy resin Quetol 812, a shrinkage along the Z axis of approximately 50% has been reported [150]. Thus the thinning observed and compensated for in this study is within the range of shrinkage expected for epoxy resin. Once the Z-scale is set, not only the quantitative output is adjusted, but also the model display, stretching it by the respective amount in Z.

To summarize, this thesis established a protocol that consists of a chemical fixation combined with high-pressure freezing and freeze substitution to enable the preservation of the ultrastructure of the synaptonemal complex and telomere attachment sites with associated LINC complexes for high 3D resolution tomography while avoiding artefacts introduced by sole chemical fixation or sole high-pressure freezing. Common artefacts of the techniques have been assessed and have been corrected for.

# 4 Chapter II: The molecular architecture of the synaptonemal complex (SC)

The synaptonemal complex (SC) is one of the key structures involved in the success of meiosis. As previously mentioned, the assembly and disassembly of the SC is tightly coordinated with essential meiotic processes such as synapsis, recombination, and segregation of the homologous chromosomes [116, 151]. A disturbed (de)construction of the complex leads to failures of the meiotic program to various degrees [152, 115, 153, 154]. Furthermore, unlike the components of the SC that are vastly divergent on the amino acid level, the overall structure of the complex is highly conserved amongst diverse organisms [87, 88]. Thus the structure of the synaptonemal complex plays an essential role in the meiotic program. Unraveling the precise molecular organization of the SC therefore enriches our understanding of its function.

The ladder-like structure of the SC is made up of two lateral elements (LEs, axial elements prior to synapsis) that frame the central element at equidistance [155, 156, 157, 158]. The chromatin of the homologous chromosomes is attached to lateral elements in regular arrays of DNA loops [159, 31]. Each of the lateral elements is connected with the central element by a multitude of transverse filaments which are oriented perpendicular to the LEs and the CE, spanning half the central region (CR) [155, 156, 157, 158].

In the last 60 years, a variety of studies have been conducted to uncover the molecular organization of the synaptonemal complex. Early studies were mostly based on electron microscopy (EM) [157]. Interestingly, these studies revealed a conserved width of the central region of approximately 100 nm (range: 90 nm – 150 nm) indifferent of varying genome sizes between species [89]. Immunolocalizations of the SC components, complemented by biochemical and genetic approaches, revealed the molecular identity of the SC proteins. In mouse, the eight SC proteins that have been identified to date are: SYCP2 and SYCP3 of the lateral element, central elements proteins SYCE1-3, TEX12 and SIXS06 as well the transverse filament protein SYCP1 [96, 97, 98, 160, 161, 99, 100, 162, 101, 102] (Figure 8).

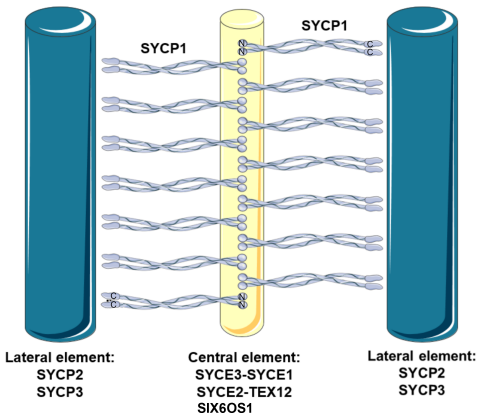


**Figure 8: The synaptonemal complex (SC) in mouse.** Schematic representation of the SC in mouse showing the morphological components of the complex and the proteins that comprise the individual components. Lateral elements (dark blue): SYCP2 and SYCP3; central element (yellow): SYCE1-3, TEX12, SIX6OS1, and TEX12; transverse filament protein SYCP1 in light blue. Figure adapted from [90].

The advent of super-resolution techniques provided the necessary nanoscale resolution to additionally study the organization of these SC proteins on the light microscopic level [127, 163]. In 2015, the above-mentioned SC proteins, except SIX6S06, were localized using 2D *d*STORM [127]. Based on the respective images of the study, localization distributions of the individual proteins were generated and integrated into a combined model of the molecular organization of the SC proteins. In frontal view sections, the two strands of the lateral element protein SYCP3 are bimodally distributed at a separation of 221.6 ± 6.1 nm [127] which is in accordance with distances measured between the two lateral elements resolved by EM [155, 156, 157, 158]. The study further reported monomodal distributions for the central element proteins in frontal view sections [127]. At 20-30 nm lateral resolution, *d*STORM further has the resolution power to detect different spatial positions of a single protein. Thus, the N- and the C-terminus of the filamentous transverse filament protein SYCP1 could be localized individually using respective antibodies in the aforementioned study. In accordance with previous immunogold localizations and biochemical approaches, the C-terminus of SYCP1 localized to the inner edge of the lateral element (visualized by SYCP3 localization), while the N-termini localized to the very center of the central element in frontal views of the SC [114, 110, 127].

Interestingly, in lateral views, the analysis of *d*STORM images revealed bimodal protein localization distributions of the N-terminus of SYCP1 and SYCE3 of the central element that suggest a bilayered organization of the central element [127]. These findings are in accordance with immuno-EM localizations of these central element proteins conducted in 2016 by Hernandez-Hernandez et al. [128]. In the respective study, SYCP1-N and SYCE3 were also distributed bimodally, while SYCE1, SYCE2, and TEX12 fol-

lowed a monomodal distribution in lateral views sections. As a result, the authors proposed a model of the central element organization where SYCP1-N and SYCE3 define two outer layers that circumscribe SYCE1, SYCE2-TEX12 [128]. A layered organization of the central element is further supported by early electron tomograms of the SC. In insects, ET has revealed the separation of the CE into three to four distinct central element components in cross-sectional views [129, 130]. The transverse filaments pass solely through these components and are absent from the spaces in between. This predetermines the organization of the central element and the transverse filaments associated with it into three to four distinct layers [129, 130]. In mammals, the central element appears amorphous which complicates a visual assignment of the transverse filaments into layers in respective tomograms [157]. Consequently, a true 3D model of the continuous course of the TFs is required that not only allows the visual but also the mathematical detection of a layered organization of the transverse filaments within the CE. However, at the time when the first ET of the SC was conducted, it was neither technically possible to perform direct 3D reconstructions of the recorded structures, nor to annotate the structures within the SC.

In the following section, this thesis introduces the first electron microscope tomography derived 3D model of the SC based on actual morphological data with a special focus on the transverse filaments. To generate this model, electron tomography and manual feature extraction were applied to murine pachytene spermatocytes. Based on this model, quantitative and topological data of the transverse filaments were derived. This work was conducted together with Sebastian Filbeck in the context of his master thesis and was published in [90]. Sebastian Filbeck assisted in the segmentation of the tomograms and performed an initial mathematical analysis.

The findings of the electron microscope tomograms were complemented by protein distribution analyses based on the novel super-resolution technique expansion microscopy in combination with structured illumination microscopy. The expansion microscopy experiments in the present work were conducted in cooperation with Fabian Zwettler [164].

## 4.1 Electron microscope tomography of the SC

**According to Spindler *et al.* 2019b [90].**

Without a 3D model of the SC, quantitative and topological data is limited to a bare minimum. In hamster, a number of 50-80 transverse filaments per micrometer have been reported [165]. Early electron tomographic studies in *Blabs cribrosa*, *Drosophila melanogaster* and rat suggested a multilayered organization of the central element, as mentioned above [129, 130]. In this thesis, electron microscope tomograms of the synaptonemal complex of 14-day-old mice have been generated to expand our knowledge on the molecular architecture of the SC with a special focus on the transverse filaments.

The force necessary to move the telomeres is generated in the cytoplasm and transduced onto the telomeres through LINC complexes that concentrate at telomere attachment sites. Consequently, the synaptonemal complex at meiotic telomere attachment sites should be subjected to a higher mechanical load compared to SCs at the center of the nucleus, referred to as interstitial SCs. In order to detect potential differences between SCs at attachment sites vs interstitial SCs, tomograms were acquired both at the nuclear envelope, as well as in the center of the cell (Figure 9).

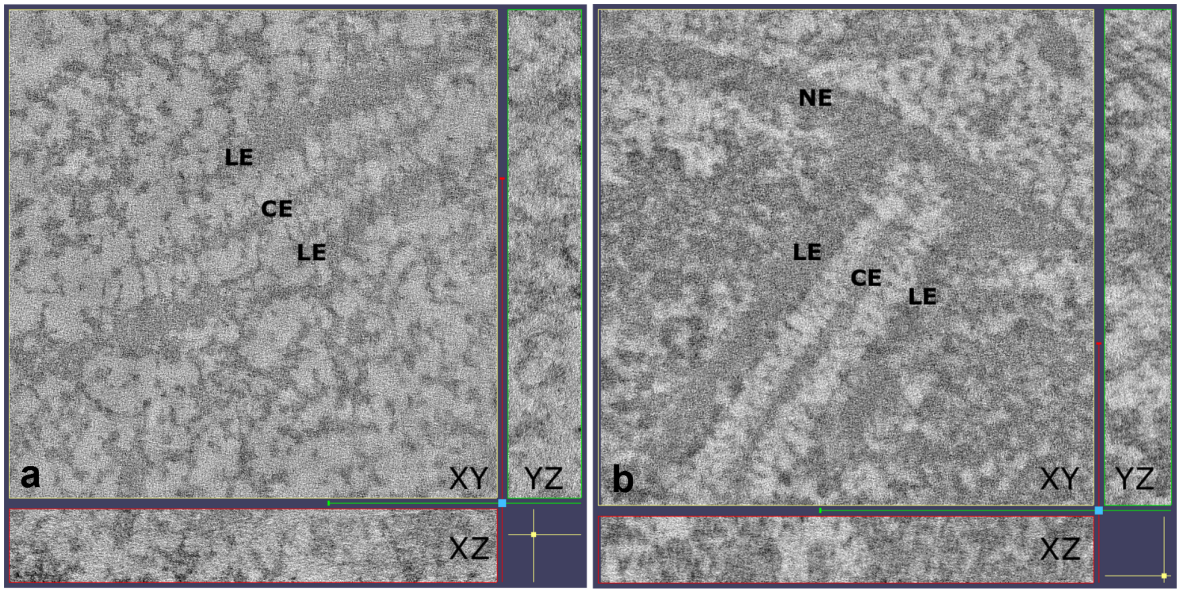


**Figure 9: Electron tomograms of the synaptonemal complex at the center of the pachytene nucleus and at the attachment of the meiotic telomeres to the nuclear envelope.** XY/XZ/YZ views of an interstitial SC (a) and an attached SC (b). LE: lateral element; CE: central element; NE: nuclear envelope. Figure adapted from [90].

Dual-axis electron tomograms of frontal view interstitial and attached SCs were ac-

quired, reconstructed and manually segmented to create 3D models (Figure 10; a movie of the 3D model is available online[1] and a high-resolution version of the movie is available in the digital appendix). In order to accurately model the course of the TFs in 3D, manual segmentation was carried out over the respective multiple z planes based on signal continuity. In order to detect potential differences between SCs at attachment sites vs interstitial SCs, the respective tomograms were initially treated as two separate groups for the data analysis.

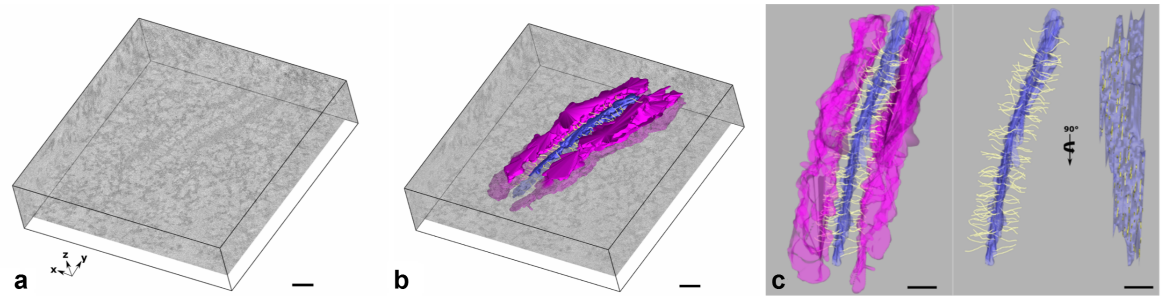


**Figure 10: Generation of the EM-derived 3D model of the synaptonemal complex.** a. Reconstructed tomogram slice showing the tripartite synaptonemal complex. LE: lateral element, CE: central element, Ch: Chromatin. Coordinate system representation indicating the three-dimensional orientation of the tomogram. b. 3D model of the SC generated through manual segmentation emerging from a virtual section of the tomogram. Magenta: lateral element; blue: central element; transverse filaments in yellow. c. Frontal (left) and lateral (right) view of the synaptonemal complex model without the lateral elements. Figure adapted from [90]. Scale bars: 100 nm.

### 4.1.1 Stoichiometry of transverse filaments

A first step in gaining insight into the molecular architecture of the SC lies in unraveling the stoichiometry of its components, specifically that of the transverse filaments. Therefore, the point data of the segmented structures was extracted from the 3D models and processed through custom Matlab scripts for quantification (see Methods). The measurement of the well-documented width of the central region (roughly 100 nm) was used to validate the accuracy of the 3D model (Figure 11, Table 12). The distance from the inner edge of one of the modeled lateral elements to the inner edge of the opposite LE is 114 nm ± 17 nm (Figure 11, Table 12). From the inner edge of one LE to the edge of the CE, the distance is 45 nm ± 10 nm and the width of the CE is 29 ± 8 nm. These metrics are in accordance with transmission electron microscopic and early EM tomographic data [155, 156, 157, 158].

[1] https://static-content.springer.com/esm/art%3A10.1038%2Fs41598-019-52455-4/MediaObjects/41598_2019_52455_MOESM2_ESM.avi

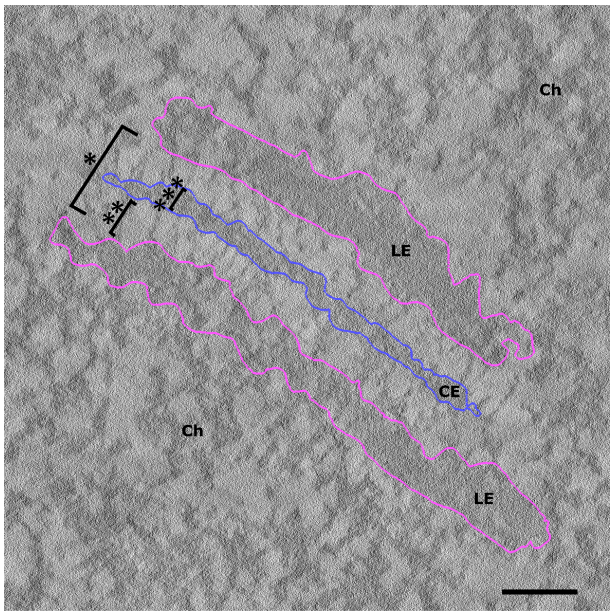


**Figure 11: Quantification of synaptonemal complex dimensions.** Virtual tomogram section with annotated components of the SC (LE: lateral element; CE: central element; Ch: chromatin). Measured distances within the SC: the width of the central region (*), the distance between the lateral and central element (***, LE-CE) and the width of the central element (***). Scale bar: 100 nm. Figure adapted from [90].

For the initial characterization of the transverse filaments, their number, diameter, and length were determined. The quantitative data presented here was derived from six SC tomograms containing 501 TFs. One micrometer of the synaptonemal complex is populated with an average of 79 transverse filaments, which matches the upper limit of the reported 50-80 TFs/$\mu$m in hamster [165]. Transverse filaments are further packed at a density of 1046 TFs/$\mu$m$^2$ $\pm$ 253 (measured at the CE insertion site of the TFs; Figure 12). Under the respective experimental conditions, the diameter of the transverse filaments is 1.9 nm ($\pm$ 0.3 nm).

**Table 12:** Central region quantification

| | Metric | Mean | Std |
|---|---|---|---|
| * | central region width | 114 | 17 |
| ** | distance from LE-CE | 45 | 10 |
| *** | central element width | 29 | 8 |

### 4.1.2 The transverse filaments within the context of the lateral and central element

Transverse filaments consist of homodimers of SYCP1 [112]. The results of previous studies have indicated that the N-termini of SYCP1 interact in the central element, while the C-termini are inserted into the lateral element [97, 110, 111]. Electron microscope tomography allows the transverse filaments, for the first time, to be traced within the environment of the central and lateral elements due to the higher axial resolution provided by the technique. The average length of the transverse filaments

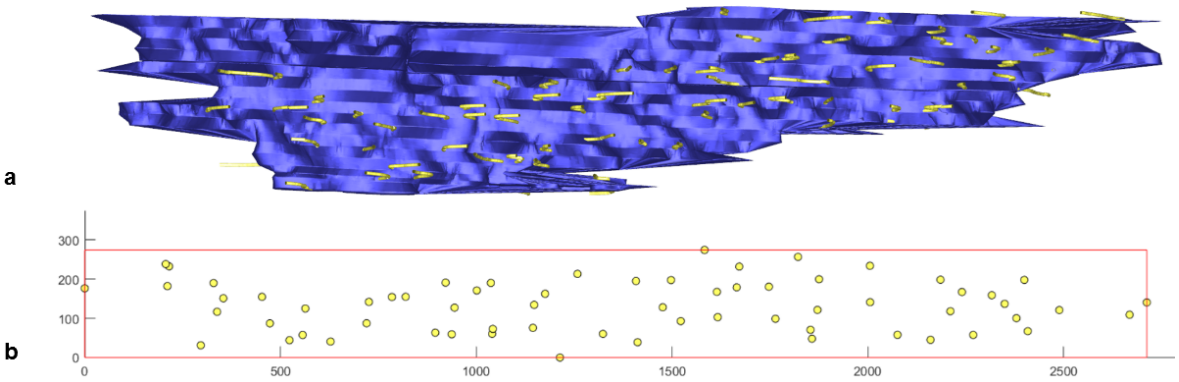


**Figure 12: Density of the transverse filaments of the synaptonemal complex.** a. Lateral view of the central element without the lateral element showing the set transverse filaments embedded in one of the lateral elements. b. 2D projection of the endpoints of the transverse filaments in the lateral element. A box is fitted through the four outer points to estimate the area of the SC that is occupied by transverse filaments (in pixel). Figure adapted from [90].

is 88 nm (± 14 nm) (see Figure 13). 14 nm (± 7 nm) of the transverse filaments are hereby embedded within the central element and 21 nm (± 9 nm) in the lateral element (see Figure 13). Correspondingly, the segment between the lateral and the central element is 53 nm (± 13 nm) long (Table 13).

**Table 13:** Quantification of transverse filaments

| | Metric | Mean | Std |
|---|---|---|---|
| I | length | 88 | 14 |
| II | insertion in LE | 21 | 9 |
| III | midsection in CR | 53 | 13 |
| IV | insertion in CE | 14 | 7 |

The shape and conformation of a protein have a major part in the protein's function. In multiprotein complexes, the interaction and distribution of the copies of a protein within the complex further contribute to the proteins individual function and the overall function of the complex. SCs are commonly represented as symmetric ladder-like structures with multiple pairs of opposing transverse filaments that interact within the central element [158]. The 3D ET based models generated in this work allow the analysis of the distribution of the transverse filaments within the SC. Counting the number of TFs in a segment of the SC revealed a difference of up to 21% between the two sides of the SC. This implicit asymmetry is causing some of the transverse filaments to lack a partner on the opposite side. Overall, three arrangements of transverse filaments, depicted in Figure 14, were frequently observed: TFs with a neighbor on the same side ("parallel"), the opposing site ("opposite") and TFs without a partner ("single").

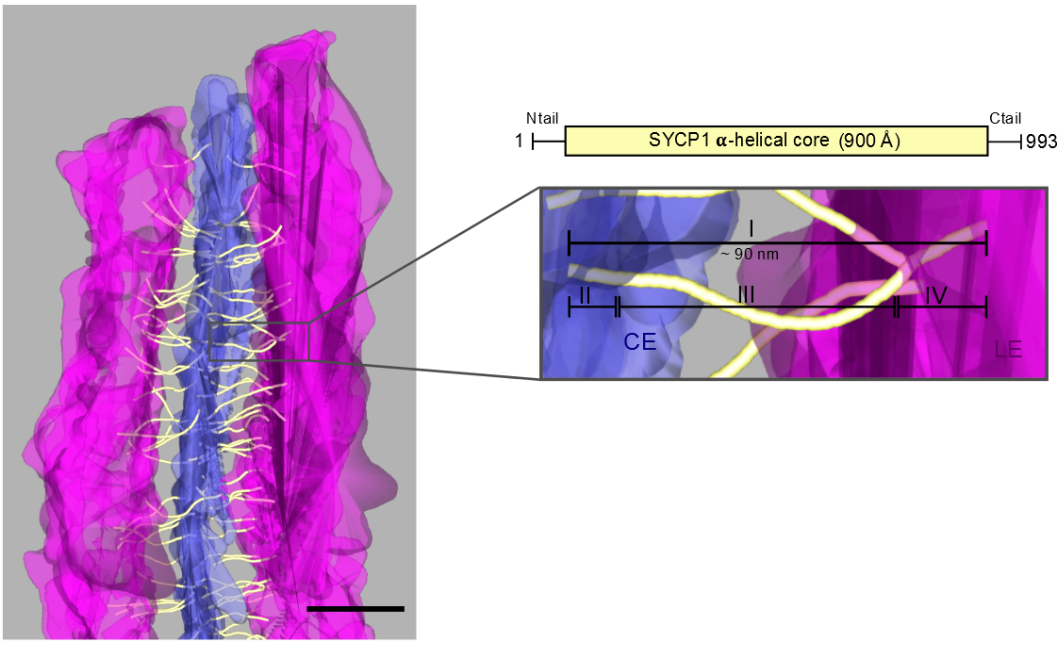


**Figure 13: The transverse filament in the lateral and central element of the synaptonemal complex.** Left: Frontal view of the ET based 3D model of the SC. Lateral elements depicted in purple, the central element in blue and transverse filaments in yellow. Scale bar: 100 nm. Right top: Simplified sequence of murine SYCP1 that is 993 amino acids long. The majority of the protein is made up of an $\alpha$-helical core protein of 900 angstroms that is flanked by short unstructured N- and C-terminal sequences. Right bottom: Magnified view of a single transverse filament shown on the left. The average length of the TFs is roughly 90 nm (I). The filaments are subdivided into three sections: a part embedded in the central element (II), a larger midsection (III) and a part embedded in the lateral element (IV). Figure adapted from [90].

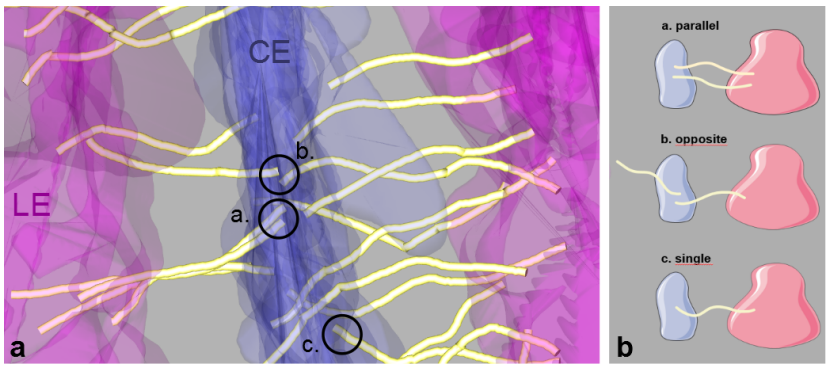


**Figure 14: Transverse filament pairings in the central element.** (A) Overview of the three frequent transverse filament pairings in the central element within one of the 3D models of the SC: a. neighboring tranverse filaments originating from the same lateral element; b. neighboring transverse filaments originating from opposite lateral elements; c. single transverse filaments without a partner on either side. (B) Model of the three frequent transverse filament pairings in the central element: a. parallel, b. opposite and c. single. Figure adapted from [90].

The apparent asymmetry of the complex gave rise to the question about minimum distances between transverse filaments. In a symmetric synaptonemal complex, the distance between opposing transverse filaments should be smaller compared to the distance between transverse filaments that are associated with the same lateral element

(parallel transverse filament pairs). To this end, the distance between the CE-endpoint of a certain TF and the endpoint of the next opposing TF (i.e., originating from the opposite LE) as well as to the endpoint of the next parallel TF (i.e., originating from the same LE) was determined. The average minimal distance was 17 nm (± 9 nm) for opposite TFs and 20 nm (± 10 nm) for parallel TFs. The exact distance distributions are shown in Figure 15. A statistically significant difference between the two data sets is observed ($p = 4.63 \times 10^{-10}$, Wilcoxon rank-sum test). The average minimal distance between TF endpoints in the lateral element was 21 nm (± 10 nm). No significant difference to parallel TFs in the CE was observed ($p = 0.0438$, Wilcoxon rank-sum test).

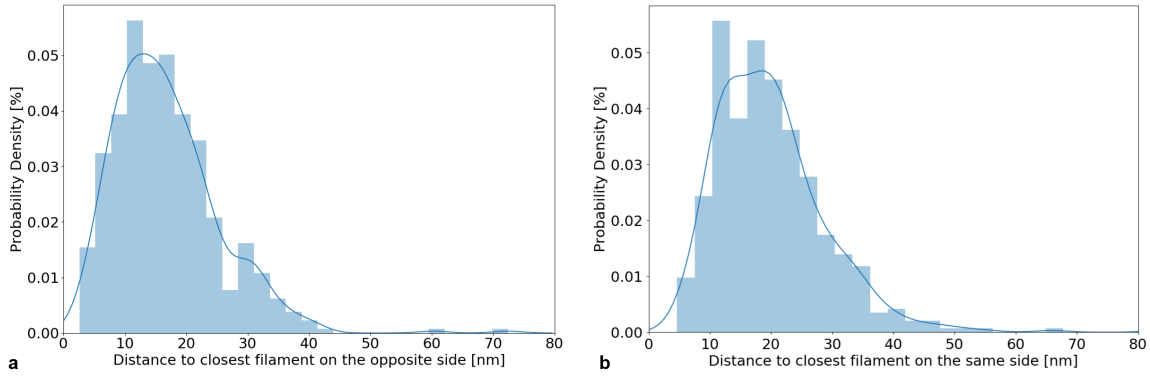


**Figure 15: Distribution plots of the CE-endpoint distance to the CE-endpoint of the closest opposing (a) and parallel (b) transverse filament (TF).** There is no significant difference in the distance between neighboring filaments compared to the distance of neighboring transverse filaments that are anchored in the same lateral element. Figure adapted from [90].

The ends of the SC are anchored in distant regions of the nuclear envelope. As mentioned earlier, they are associated with the telomere attachment sites, where cytoplasmic forces are transduced onto the meiotic telomeres. Consequently, the SC ends should be inherently exposed to greater mechanical stress compared to SC sections at the center of the nucleus (interstitial SC). In order to detect potential structural differences between the attached and interstitial SCs, the two groups were initially treated separately. Neither the mean length of the transverse filaments, nor their respective lateral and central element indent or the mean width of the central element differed significantly between attached or interstitial SCs (see Table 14). Next, the average minimum distance between the transverse filaments of attached and interstitial SCs was compared. The minimum distances of the transverse filaments did not differ for the

two groups, indicating that the organization of the transverse filaments of attached and interstitial SCs is similar. Statistical significance was assessed through the Wilcoxon rank-sum test. Overall, attached and interstitial SCs did not differ significantly and were therefore treated as a single data set in the present work.

**Table 14:** Statistical tests for significant differences between the transverse filaments of attached vs interstitial SCs. LE: lateral element, CE: central element, CR: central region.

| Metric | Significant Difference | p-value (Wilcoxon rank-sum) |
|---|---|---|
| length | no | 0.1156 |
| minimum distance | no | 0.0902 |
| insertion in LE | no | 0.5881 |
| insertion in CE | no | 0.2327 |
| width of CR | no | 0.2217 |

### 4.1.3 Monolayered organization of the transverse filaments

Several studies have proposed a multilayered organization of the synaptonemal complex. The central element of insects is characterized by three to four distinct components in a cross-sectional view. The transverse filaments are associated with these components and lacking from the spaces in between. As a result, the set of TFs of a synaptonemal complex appear organized into three to four according layers [129, 130]. The central element in mouse has an amorphous quality which complicates a visual assignment of the transverse filaments into distinct layers as mentioned earlier. Immunogold and superresolution immunofluorescence analyses however suggested a bilayered organization of the transverse filament protein SYCP1 in mouse.

This thesis directly addresses the proposed organization of transverse filaments into two layers by visual and mathematical analysis on the basis of a 3D ET model of the SC. An initial visual inspection of the SC in a cross-section view did not reveal distinct layers (Figure 16). In this view, the modeled transverse filaments are superimposed which complicates the evaluation. Therefore, the intersection points of the TFs with the central element were inspected in the lateral view. Since the central element is three dimensional, the intersection points may reside in different z-plane, which can again lead to misinterpretation due to superimposition. To avoid this, a 2D projection of the intersection points of the TFs with the CE was generated. The projection of the intersection points of the transverse filaments with the central element did not show

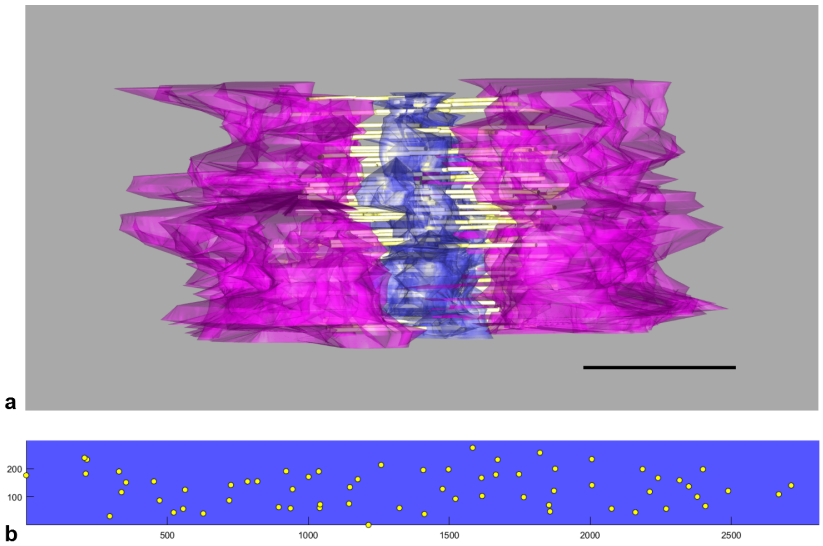


**Figure 16: Visual analysis of a potential layered organization of the transverse filaments in the 3D ET derived model.** a. Cross-sectional view of the 3D SC model. In this view, no organization of the transverse filaments in distinct layers is apparent. Magenta: lateral elements, purple: central element, yellow: transverse filaments. Scale bar: 100 nm. b. 2D projection of the intersection points of the transverse filaments with the central element (in pixel). The 2D projection does not reflect an organization of the transverse filaments into layers. The area of the central element that contains transverse filaments is depicted in purple. Figure adapted from [90].

a distinct layered organization either (Figure 16). Since visual analysis is error-prone, an additional mathematical analysis was performed. Under the assumption that mammalian TFs are organized into two layers, two planes were fitted through the endpoints of each TF. The transverse filaments were therefore assigned into two groups depending on the lateral element they were associated with. The two groups were analyzed separately. A bilayered organization of the TFs would be reflected in two parallel planes fitted to the TF endpoints. The fit however supports the organization of the TFs into a single layer for all of the six analyzed tomograms. Since the algorithm used in this study forces the fit of two planes to the data, the transverse filament points in Figure 17 are still assigned to two layers along the course of the SC through the section.

In conclusion, both the visual inspection (cross-sectional view and 2D projection of intersection points of the intersection points of the TFs with the CE) and the fitting of 3D planes to the TF data refute the organization of the transverse filaments into two distinct layers.

Since this outcome is rather surprising in light of previous results, the hypothesis of a layered TF organization was additionally challenged by the novel super-resolution

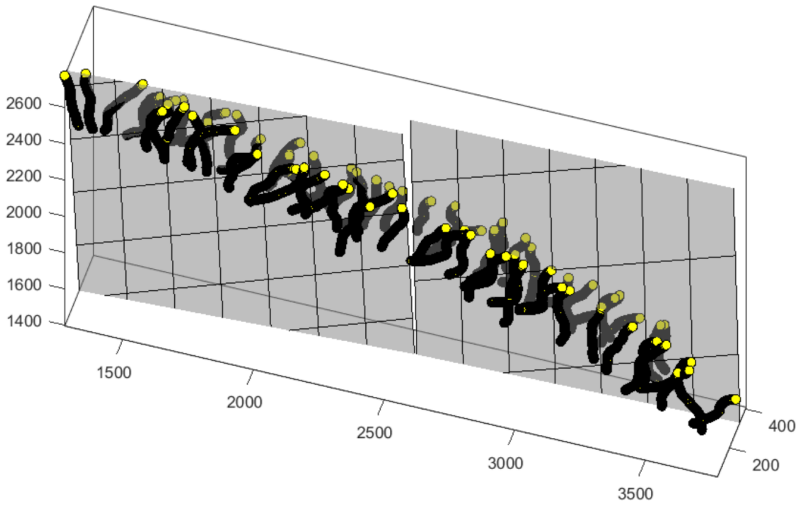


**Figure 17: Mathematical analysis of a potential layered organization of the transverse filaments in the 3D ET derived model.** Two planes were fit through the end points of the transverse filaments. A fit supporting a bilayered organization of the SC would be reflected in two roughly parallel planes. Instead, the reveals a single layer separated only due to the course of the synaptonemal complex. Yellow: point representation of the transverse filaments, gray: two fitted planes. Point coordinates in pixel.Figure adapted from [90].

technique expansion microscopy.

## 4.2 Expansion microscopy of the SC

**According to Zwettler and Spindler *et al.* 2020 [164].**

Both authors contributed equally to the expansion microscopy work. F.U.Z., M.C.S., M.S., and R.B. conceived and designed the project. M.S. and R.B. supervised the project. F.U.Z, M.C.S., A.K., and T.K. performed all experiments. S.R. developed Line Profiler. S.R. and F.U.Z. performed data analysis. All authors wrote and revised the final manuscript.

In order to probe for a multilayered organization of the synaptonemal complex, nanoscale resolution is required. The resolution limit of diffraction-limited microscopes is defined by the optics. According to Abbe, the resolution limit is defined as

$$d = \frac{\lambda}{NA_{\text{objective}}} \tag{4}$$

with $\lambda$ = wavelength of the excitation light

and $\text{NA}_{\text{objective}}$ = numerical aperture of the objective.

Strategies to surpass the diffraction limit and increase the resolution of a microscope

range from introducing additional optics into the light path of the microscope, to exploiting the physico-chemical properties of dyes to post-processing algorithms that extract high-frequency information of the sample. In 2015, a novel way of achieving resolution beyond the diffraction limit was introduced by Edward Boyden and colleagues [134]. This approach, termed expansion microscopy, is based on linking the biomolecule of interest into a swellable polymer to physically enlargen the sample instead of pushing the limit of the microscope itself. Combining expansion microscopy with, e.g., structured illumination microscopy (SIM; lateral resolution: roughly 100 nm) results in a lateral resolution of 20-30 nm comparable to that of single-molecule localization techniques, such as *d*STORM. The advantage of Expansion-SIM over *d*STORM is a comparatively higher achievable labeling density (specifically for post-labeling techniques as described below). Ex-SIM further provides the option for multi-color localizations that are solely limited by the number of available laser lines.

As mentioned earlier, protein distribution analyses performed on *d*STORM imaged murine testes spreadings revealed a bimodal distribution of the central element proteins SYCP1-N and SYCE3 in lateral view sections of the synaptonemal complex. This result suggests a bilayered organization of the SC [127]. The higher labeling density provided by Ex-SIM unlocks the potential to resolve even higher structural detail compared to *d*STORM. An initial comparison between the immunolocalization of SYCP3 on unexpanded spreadings that were imaged with *d*STORM and expanded spreadings imaged with SIM revealed a more continuous SYCP3 signal for Ex-SIM (Figure 18). Therefore, Ex-SIM was used to address the question of a layered SC in mouse on a nanoscale light microscopic level as a complementary technique to electron microscope tomography (ET). Here, Ex-SIM is performed on testes spreadings of the mouse for the (triple)immunolocalization and subsequent distribution analysis of the synaptonemal complex proteins SYCP1-N, SYCE3 and SYCP3.

To date, several expansion protocols, such as protein-retention ExM (proExM), magnified analysis of the proteome (MAP), and ultrastructure ExM (U-ExM) are available. The main difference between the approaches is whether the immunolocalization is performed prior to or after the expansion. The proExM approach is an extension of the initial expansion microscopy protocol. Here the immunolocalization is performed as a

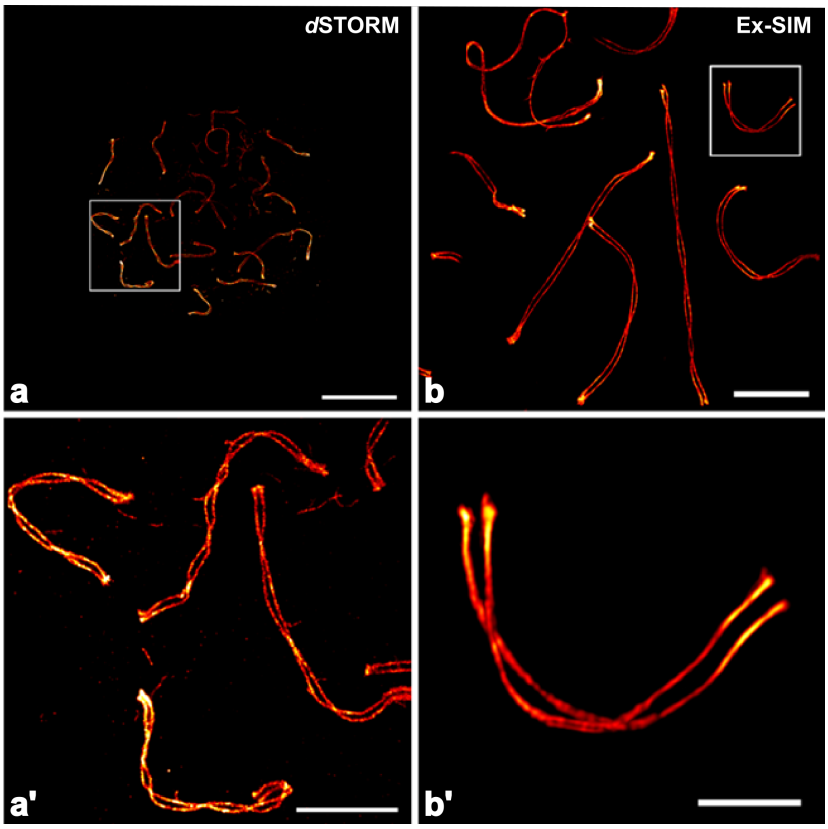


**Figure 18: Super-resolution microscopy of the lateral element protein SYCP3 localized on murine spreadings.** a. *d*STORM image of SYCP3 (acquired by Katharina Schuecker). a'. Magnified view of boxed region in (a). b. SIM image of SYCP3 localized on expanded nuclear spreadings of murine testes (post-expansion labeling approach magnified analysis of the proteome; maximum intensity projection). b' Magnified view of boxed region in (b). An initial visual comparison between the Ex-SIM and *d*STORM images suggests comparable spatial resolution of the two techniques. Note the higher labeling density of the expanded samples apparent through higher signal continuity of the SYCP3 strands in b/b'. Scale bar: (a-c) 10 $\mu$m, (d-f) 3 $\mu$m. Figure adapted from [164].

first step (pre-expansion labeling), followed by linkage of the label into the polymer and expansion of the hydrogel through immersion in water. For the MAP and U-ExM approaches, the immunolabeling is performed at a later stage, after the sample has been embedded in the hydrogel, denatured and expanded. Therefore, MAP and U-ExM are termed post-labeling (post-expansion labeling) approaches.

Depending on the protein or protein complex of interest, not all of the approaches conserve the 3D molecular architecture equally. In the context of multiprotein complexes, the number of parameters that influence the success of isotropic expansion increases. For centrioles, the U-ExM approach resulted in the best preservation of ultrastructural details [166]. Prior to addressing the question for a multilayered organization of the SC, in a first step, the most suited technique for the Ex-SIM of nuclear spreadings needed to be determined.

### 4.2.1 Expansion microscopy of the synaptonemal complex

In order to find the most suited protocol to expand nuclear spreadings and immunolocalize the synaptonemal complex proteins, three different expansion microscopy (ExM) protocols were compared on the basis of their respective expansion factor and their ability to preserve ultrastructural detail: the pre-expansion labeling protocol proExM, and the two post-expansion labeling protocols MAP and U-ExM. The efficiency of the different expansion techniques was initially evaluated solely on the basis of the SYCP3 channel. In Ex-SIM (and *d*STORM) images, the two SYCP3 positive strands associated with a pair of homologs twist around each other, exposing frontal and lateral views of the SC (Figure 19).

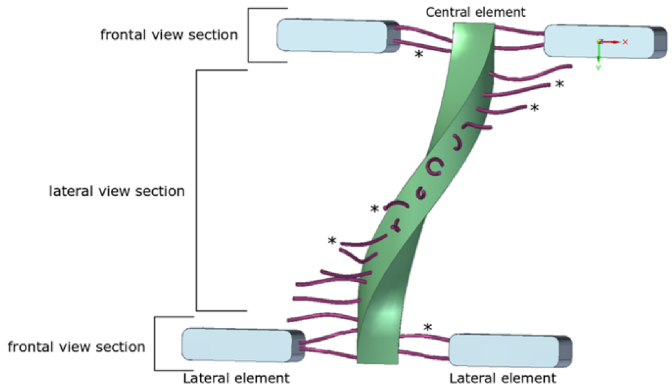


**Figure 19: Frontal and lateral view sections of the synaptonemal complex.** Due to the helical nature of the SC, frontal and lateral view sections get exposed while the complex turns around the own axis through the meiotic nucleus. The lateral element is not shown in the lateral view section to highlight the transverse filaments (∗). Figure adapted from [164].

The expansion factors of the different techniques were calculated on the basis of SYCP3 intensity profiles generated from 2D maximum intensity projections of *d*STORM and Ex-SIM. As mentioned earlier, intensity profiles of SYCP3 compiled of *d*STORM maximum intensity projections show a bimodal signal distribution in frontal views. Here the two peaks of the SYCP3 signal are separated by roughly 220 nm [127]. Since the lateral resolution of *d*STORM and Expansion-SIM are comparable (20-30 nm), this value can be used as a reference for the peak-to-peak distance of SYCP3 in unexpanded samples. To calculate the expansion factor, the peak-to-peak distance of the SYCP3 signal was determined for maximum intensity projections of the SYCP3 signal and divided by the 220 nm unexpanded reference distance.

To obtain objective and comparable data on these distances, the automated image processing software "Line Profiler"[2] was developed by Sebastian Reinhardt in the frame of

[2] `https://doi.org/10.5281/zenodo.2643213`

the collaboration. The tool uses a collection of common image-processing algorithms to detect the frontal views of the SC and to measure the distance between the two SYCP3 strands associated with each pair of homologs in these views. The calculation of the peak-to-peak distance requires the knowledge of the orientation and the maximum extent of the SC in frontal view sections. First, in order to determine the direction of the SC, the shape of the homogenized SYCP3 signal is skeletonized into one pixel wide lines using Lee's algorithm. In triple localizations, the orientation of the SC is determined on the basis of skeletonizing the signal of the central element protein SYCE3 instead of SYCP3 (two-channel mode). The pixel coordinates of each line are fitted with a c-spline that models the course of the line. This enables the calculation of its derivate. A line profile is constructed perpendicular to this derivate for each pixel of the line. In order to fit a line profile to the data that matches the extend of the SC, a floodfill algorithm is applied to the SYCP3 signal. The resulting line profiles show the bimodal distribution of the SYCP3 signal with the two peaks representing the two SYCP3 strands. In order to quantify the peak-to-peak distance, each peak was fit with a Gaussian distribution function. The difference between the means of the two Gaussian distributions determines the peak-to-peak distance. Aside from fully frontal views of the SC, the Line Profiler also determines the peak-to-peak distance at the sites where the SC transitions from frontal to lateral view section. Here the SC is narrower causing the Line Profiler to underestimate the peak-to-peak distance in fully frontal views. In distributions of the peak-to-peak distances of a single SC or several SCs (which consist of many individual line profiles), the left side of the histogram shows the underestimated distances. In order to determine the mean peak-to-peak distance of fully frontal SCs, the distributions of multiple peak-to-peak distances were therefore fit with the right half of a normal distribution.

The Line Profiler was validated by re-evaluating *d*STORM acquisitions of SYCP3 on murine nuclear spreadings conducted by Schuecker et al. in 2015 [127] (see Figure 20). Assuming the Line Profiler tool is accurate, the analysis of the *d*STORM data should result in a similar peak-to-peak distance compared to the 220 nm determined by the original analysis [127].

In the original analysis, Schuecker et al. fitted the data to a high-order polynomial

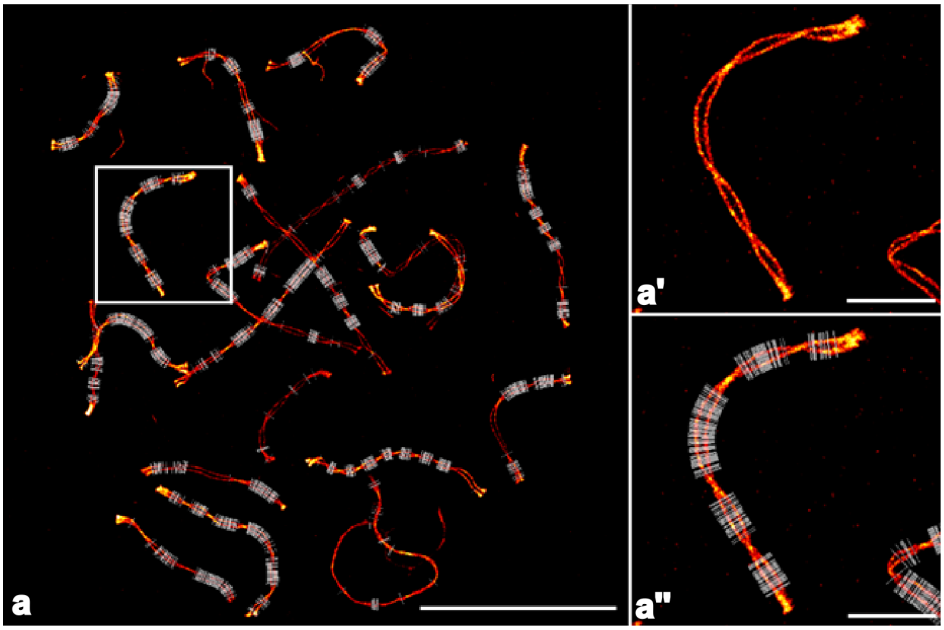


**Figure 20: Output of Line Profiler tool on maximum intensity projection of re-evaluated *d*STORM acquisitions of SYCP3 localization on murine nuclear spreadings.** a. A multitude of line profiles were fitted perpendicular to the frontal view sections of the SCs. *d*STORM acquisitions were performed by Katharina Schuecker and Thorge Holm in 2015 for their study of the molecular architecture of the SC. SYCP3 was labeled with Alexa Fluor 647. Upon visual analysis, the Line Profiler tool hereby detects the frontal view sections accurately. a'. Magnified view of the region highlighted in a. a". Magnified view of the region highlighted in a with individual line profiles. Scale bars: a. 10 $\mu$m, b-c. 2 $\mu$m. Figure adapted from [164].

(n>10). Guided by this polynomial, a sliding window algorithm was applied that facilitates the generation of an intensity histogram used to calculate the double-strand distance on the basis of a bi-Gaussian fit. For their analysis, Schuecker et al. excluded complexes unsuited for the extraction of quantitative data (non-twisting complexes, complexes with extreme curvature and overlapping complexes) from the data set in a first step using a canny edge filter or mean component analysis [127].

In accordance with the 220 nm determined by the original analysis, the peak-to-peak distance determined by the Line Profiler was 220 nm $\pm$ 21.6 nm (Figure 21).

In the first studies, the efficiency of expansion microscopy was determined mainly on the basis of the resulting expansion factor of the gel, neglecting the analysis of the preservation of ultrastructural detail. In 2018, Gambarotto et al. challenged the potential of the established original expansion microscopy approach (ExM) and the magnified analysis of the proteome (MAP) approach regarding the preservation of the ultrastructure of well-characterized isolated *Chlamydomonas* centrioles [166]. In their study, the

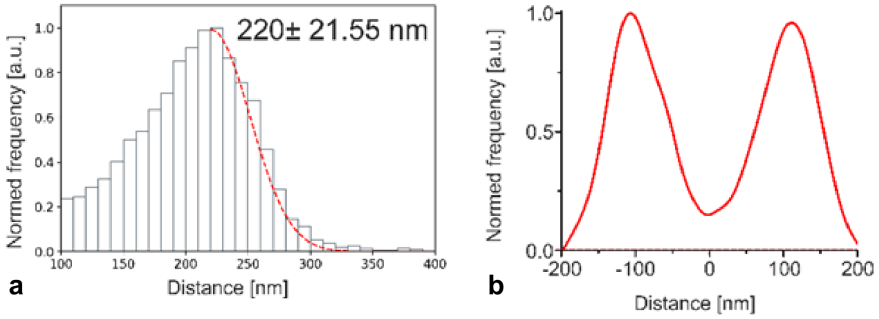


**Figure 21: Peak-to-peak distance of bimodal signal distribution of *d*STORM acquired SYCP3 signal in frontal view sections of the SC determined by the Line Profiler tool.** a. Half-normal fit of the peak-to-peak distance distributions of 7,501 line profiles. The resulting mean distance is 220 ± 21.55 nm. b. Averaged intensity line profile of 7,501 individual SYCP3 intensity profiles of six spermatocytes. Figure adapted from [164].

hydrogels expanded 4.2-fold after ExM and 3.5-fold following MAP. The diameter of the centrioles however did not match the expected expansion factor. Compared to unexpanded dimensions of the centrioles determined by *d*STORM, the diameter of the centrioles was significantly larger in relation to the gel expansion in ExM treated centrioles and significantly smaller in MAP-treated centrioles. Consequently, the results of both approaches implied the non-isotropic expansion of the centriole ultrastructure [166]. The authors therefore established a new expansion microscopy approach termed ultrastructural expansion microscopy (U-ExM) for the isotropic expansion of the molecular architecture of macromolecular complexes. U-ExM is a variant of the MAP protocol, so immunolabeling is performed after gelation and primary expansion, facilitating epitope accession. Moreover, the U-ExM approach provides the use of a weaker fixation compared to other expansion protocols. U-ExM resulted in isotropic expansion of the isolated centrioles at an improved structural preservation [166].

Since U-ExM outperformed MAP and ExM in the preservation of the molecular architecture of centrioles, the expansion potential of U-ExM for murine testes spreadings was investigated first. The expansion potential of the technique was determined on the basis of the SYCP3 inter-strand distance and on signal continuity. Surprisingly, in the context of spread spermatocyte nuclei, the U-ExM resulted in disruptions of the SYCP3 signal (Figure 22) that suggest an insufficient transfer of the protein into the hydrogel. Furthermore, U-ExM resulted in an expansion factor of only x2.4 (average distance between SYCP3 strands: 540 ± 31.29 nm in 1-channel mode; Figure 22).

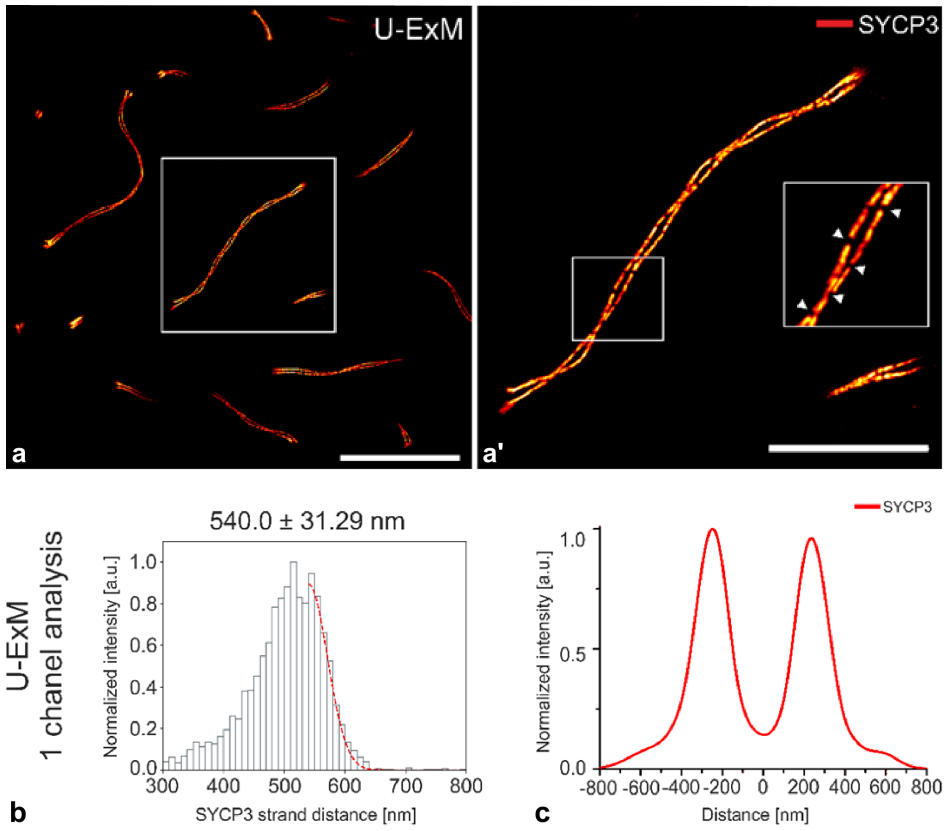


**Figure 22: SYCP3 localized on U-ExM expanded nuclear spreadings of the mouse.** a. Maximum intensity projection of SYCP3 localization on U-ExM expanded nuclear spreadings imaged with SIM. SYCP3 was labeled with SeTau647. a'. Magnified view of the boxed region in (a) showing a single SC. Note the breaks in SYCP3 signal continuity in the magnified region in (a'). b. The mean distance between the SYCP3 peaks of 25 U-ExM expanded SCs based on a half-Gaussian fit amounts to 540 ± 31.29 nm. Two separate experiments were performed for the data acquisition. c. Averaged intensity line profile of U-ExM data. Scale bars: a. 20 $\mu$m, a'. 10 $\mu$m. Figure adapted from [164].

Next, the suitability of the protein retention expansion microscopy (proExM) approach for the expansion of murine testes spreadings was explored. As mentioned earlier, proExM is an extension of the original expansion microscopy approach. Here, the proteins are directly linked into the hydrogel as opposed to the custom label being linked into the gel as required for the original approach [167]. The proExM approach resulted in a larger expansion factor of roughly x4.0 (Figure 23; 1-channel mode). However, free-radical polymerization that leads to irreversible fluorophore destruction is common in pre-expansion labeling techniques. Accordingly, the labeling density of SYCP3 was comparatively low in the proExM expanded SCs (Figure 23). Hence, also the proExM approach was unfit for the investigation of the molecular architecture of the SC.

Finally, the expansion potential of the magnified analysis of the proteome (MAP) ap-

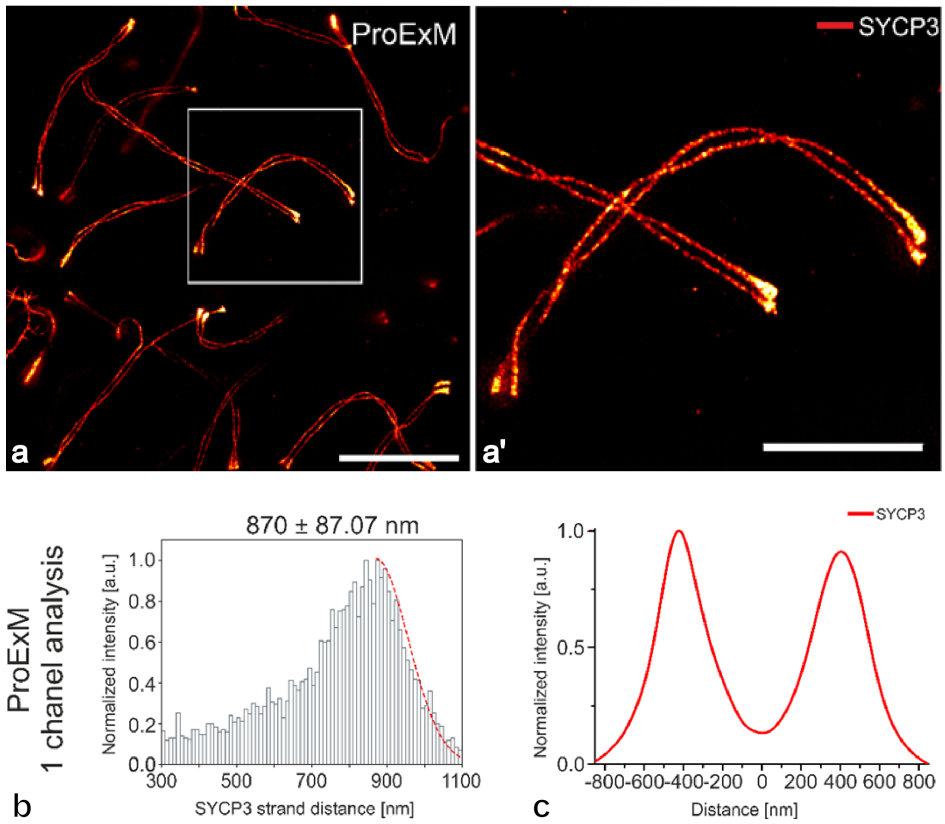


**Figure 23: SYCP3 localized on proExM expanded nuclear spreadings of the mouse.** a. Maximum intensity projection of SYCP3 localized on proExM expanded nuclear spreadings imaged with SIM. a'. Magnified view of boxed region in (a) showing a single SC. Note the low signal intensity of SYCP3 on pro-ExM expanded spreadings that is common in pre-expansion techniques, the reason being irreversible fluorophore loss due to free-radical polymerization. b. Half-normal fit of the peak-to-peak distances of the line profiles along 50 SCs. The mean SYCP3 inter-strand distance is 870 ± 87.1 nm. c. Averaged intensity line profile of the SYCP3 intensity profiles of 25 SCs. SYCP3 was labeled with Alexa Fluor 488. Figure adapted from [164].

proach was investigated. Again, as for U-ExM and proExM, SYCP3 was localized on expanded testes spreadings to determine the inter-strand distance of SYCP3 for the calculation of the expansion factor and to elaborate on the ultrastructural preservation on the ground of the signal continuity of SYCP3. Here, MAP outperformed both U-ExM and proExM. With an expansion factor of roughly x3.0 (SYCP3 inter-strand distance: 650.0 ± 50.0 nm; Figure 25) the expansion potential of MAP ranked between proExM and U-ExM. Compared to the other techniques, the SYCP3 signal did however not show any breaks which is indicative of the well preserved ultrastructure of MAP expanded SCs (Figure 24).

Since U-ExM is an extension of MAP and both approaches are post-labeling techniques, it is surprising that MAP results in a better ultrastructural preservation compared to U-ExM. As mentioned earlier, the noncontinuous signal of SYCP3 on U-ExM expanded

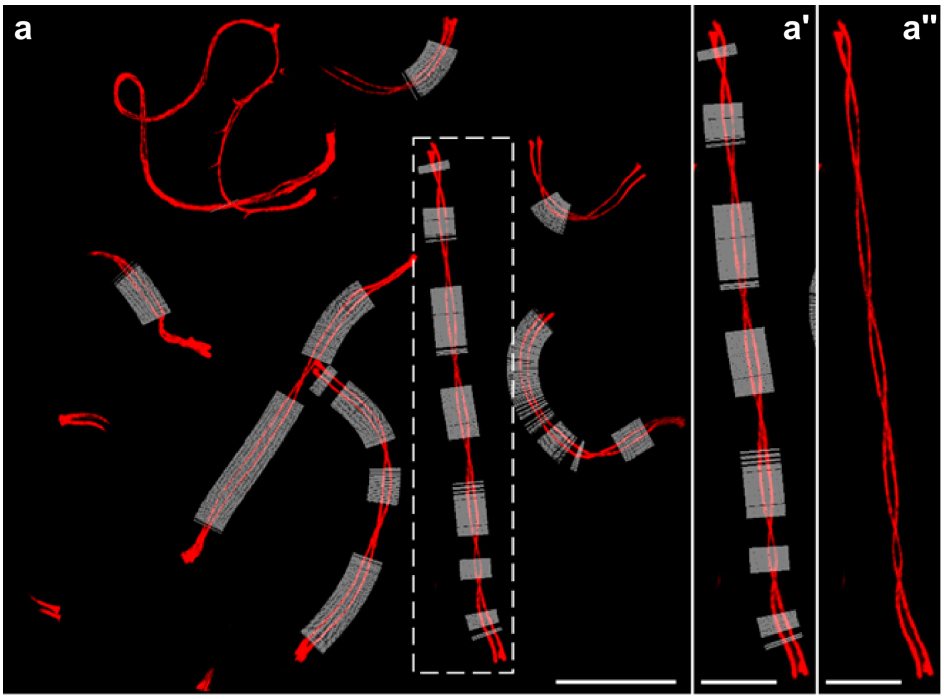


**Figure 24: SYCP3 localized on MAP expanded nuclear spreadings of the mouse.** a. Maximum intensity projection of MAP expanded SCs visualized through the localization of the lateral element protein SYCP3. SYCP3 was labeled with SeTau647. a'. Magnified view of a single SC highlighted with a dashed boxed in (a) showing the intensity profiles the Line Profiler applied perpendicular to the frontal view sections of the SC. a". Single SC highlighted by dashed box in (a) and shown in (a'). The magnified view of the SC without the line profiles reveals a continuous SYCP3 signal indicative of the well preserved ultrastructure of MAP expanded SCs. Scale bars: a. 10 $\mu$m, b-c. 5 $\mu$m. Figure adapted from [164].

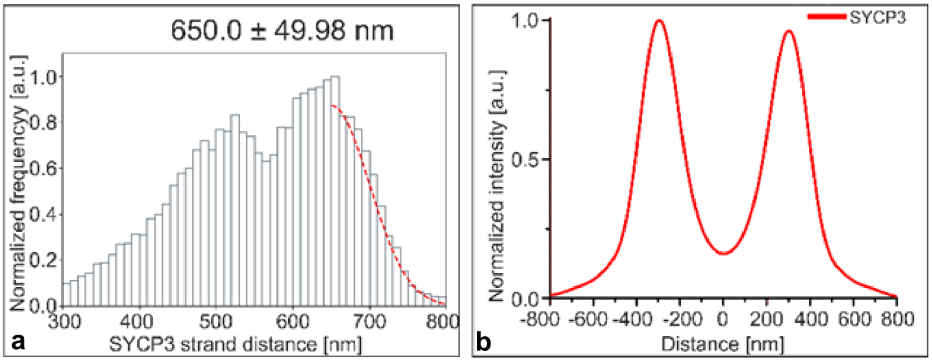


**Figure 25: Peak-to-peak distance of the SYCP3 signal on MAP expanded murine synaptonemal complexes.** a. The inter-strand distance of SYCP3 localized on MAP expanded SCs was determined to be 650.0 ± 49.98 nm by the fit of a half-normal function to 24,157 line profiles of frontal view SC sections. b. Averaged intensity line profile of the SYCP3 intensity profiles of 97 MAP-SIM SC images acquired from two independent experiments. Figure adapted from [164].

spreadings suggests an incomplete incorporation of the SC proteins into the hydrogel. Compared to U-ExM, the MAP protocol involves the use of a higher acrylamide concentration, which likely enables the detachment and full transfer of the proteins into the gel.

It is further surprising that MAP yielded a higher expansion factor compared to U-ExM, even though MAP resulted in the lowest expansion factor for centrioles [166]. The main difference between centrioles and the synaptonemal complex is their biomolecular composition. While centrioles are made up of different proteins (one category of biomolecules), the synaptonemal complex consists of both different proteins but also DNA. During MAP, proteins are denatured at high temperatures using sodium dodecyl sulfate (SDS) after gelation. Aside from the deliberate denaturation of proteins, SDS conveys an overall negative charge to the proteins. Since the DNA is too (inherently) negatively charged, the DNA-protein crosslinks repel each other within the hydrogel, which ultimately facilitates the isotropic expansion of the SC.

Overall, MAP is the most suited out of the probed protocols for the expansion for the SC proteins on murine spreadings and was therefore used to challenge the layered organization of the SC.

Aside from selecting the most suited technique for the sample, expansion microscopy presents a variety of challenges in terms of sample handling, such as gel drift, chromatic aberration, and loss of fluorescence. Therefore, an elaborate workflow for the expansion of synaptonemal complexes using the MAP protocol in combination with the Line Profiler for data analysis (shown in Figure 26) was established in the frame of this collaborative project (Figure 26).

In order to ease the handling of the samples and establish optimal conditions for the protein distribution analysis, several modifications were added to the original MAP protocol. Nuclear spreadings were generated on high-precision round 18 mm instead of rectangular 40 x 60 mm cover glasses. The smaller size of the cover slip causes the expanded hydrogel to be comparatively smaller which in turn eases the detection of the sample within the hydrogel. After an initial detection of the regions of interest with x10 objective, even smaller pieces of the hydrogels were prepared for an easy detection of the sample when using an objective that provides higher magnification. The gel pieces were transferred to poly-lysine coated cover glasses that promote adherence of the gel to the slide. Additionally, the cover glasses were incubated with fluorescent beads prior to the gel transfer. The beads were used for post-processing correction of

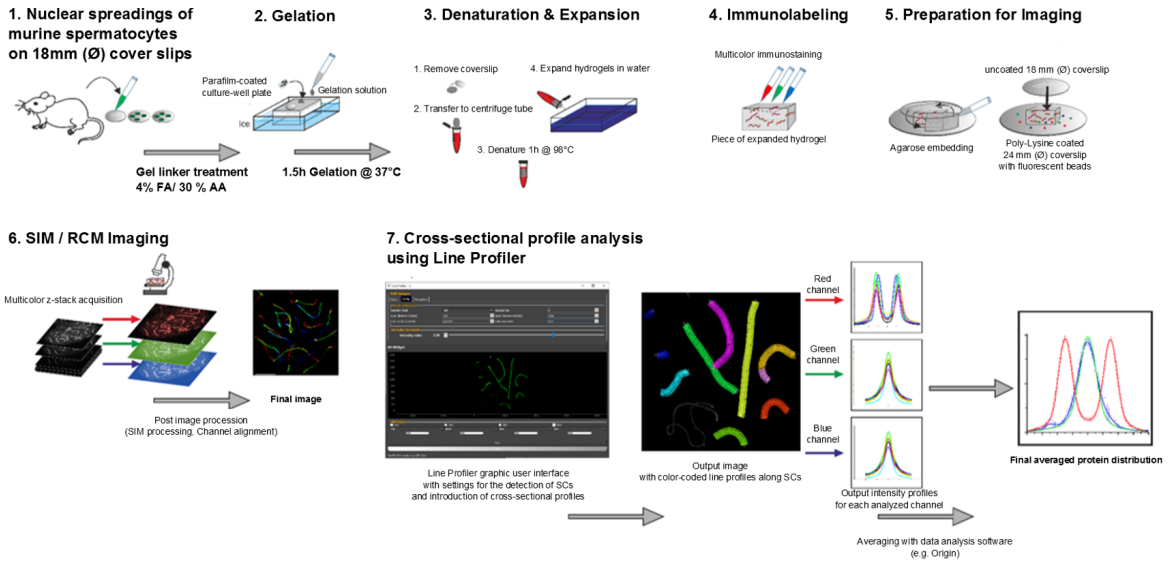


**Figure 26: Workflow of MAP-SIM expansion on SCs.** (1) Murine testis cells are spread on 18 mm round coverglasses. (2) Nuclear spreadings are then subjected to a gel linker treatment prior to gelation on a parafilm coated culture-well. Gelation is briefly initiated on ice, followed by 1.5h gelation at 37 °C. (3) Gels are carefully removed from coverglasses and transferred to pre-heated denaturation solution in which they are incubated for 1 hour at 98 °C before they are expanded in water. (4) Gels are reconstituted in PBS (not shown) before proteins of interest are immunolabeled within the gel with primary and secondary antibodies successively. Gels are then re-expanded in water. (5) Immunolabeled gels are immobilized on Poly-lysine coated coverslips and additionally embedded in agarose to prevent drift during imaging. (6) Proteins of interest are ready for imaging with preferred imaging technique (here: SIM or RCM). (7) After post-processing of the images (e.g., SIM processing, channel alignment), protein distribution analysis is performed by the custom Line Profiler tool in several channels. The line profiles of a data set are averaged to generate the global protein distribution curve. Figure adapted from [164].

chromatic aberration. During imaging, the hydrogel is submerged in water to maintain maximum expansion. Care was taken, that no water was between the adhering side of the gel and the imaging chamber. Still, due to the thermal discharge of the excitation laser, the hydrogel is prone to drift. To avoid said drift, the gel pieces were fixed in place by a thin layer of agarose framing the outer edges of the gel.

Following this elaborate workflow, triple localizations of SYCP3, SYCP1-N and SYCE3 were conducted on MAP expanded SCs. The samples were imaged with SIM to analyze the molecular architecture of the meiotic complex. Prior to generating protein signal distributions for said analysis, the efficiency and robustness of the MAP protocol was investigated in more depth. Therefore, the macromolecular expansion factor was determined and the isotropy of expanded SCs was investigated. Further, the performance of MAP expanded samples during large SIM data set acquisitions was evaluated.

In a first step, the macroscopic expansion factor of MAP-SIM was determined. Re-scan

confocal images of the same SC were acquired pre-expansion when labeled with one fluorophore (Figure 27a,d.) and post-expansion after being labeled with a different fluorophore (Figure 27b,e.). An overlay of both images was generated through rigid image registration (Figure 27c,f.). Subsequently, the image of the SC pre-expansion was transformed into the image of the SC post-expansion through similarity transformation. The dilation used in the similarity transformation is thereby used to quantify the macromolecular expansion factor. The analysis of the SCs of 7 cells from two experiments resulted in a macromolecular expansion factor of ∼x4.2 for MAP-SIM (Figure 27g.). At first glance, this macromolecular expansion factor differs significantly from the expansion factor ∼3.0 determined from the peak-to-peak distance of SYCP3 cross-sectional profiles of MAP-SIM expanded SCs compared to the peak-to-peak distance of SYCP3 of unexpanded SCs that were imaged with *d*STORM. The mismatch in expansion factors can be explained by the difference in labeling. The SC is roughly 200 nm wide with each of the two lateral elements occupying 40-50 nm in width (37.1 nm in murine spermatocytes) [168, 90]. By immunolocalizing the lateral element component SYCP3, the complex is broadened on both sides by the antibody-antibody-fluorophore complex of ∼ 17.5 nm [169] which translates into a peak-to-peak distance of ∼220 nm for SYCP3 on unexpanded samples as determined through protein distribution analysis of *d*STORM acquisitions. Under the assumption that the SC is expanded by x4.0, the SYCP3 peak-to-peak distance should scale to ∼880 nm. Since MAP is however a post-expansion labeling technique, the primary and secondary antibodies are not expanded since labeling is conducted after the expansion process. Therefore, the antibody-antibody-fluorophore complex does not contribute to the broadening of cross sectional profiles (since the unexpanded benchmark distance of ∼220 nm determined by *d*STORM already contains the additional width of the unexpanded antibody-antibody-fluorophore complex). Post-expansion labeling reduces the linkage error to a few nanometers depending on the actual expansion factor and moreover provides improved epitope accessibility [170]. As a consequence, it is likely that a higher number of epitopes at the inner edge of the lateral element can be labeled. The more balanced labeling between the inner and the outer edge of the lateral element would assign the maximum intensity of a SYCP3 strand more towards the center of the lateral element. The combined effects of the antibody-antibody-fluorophore complex not exerting a broadening effect, to the reduced linkage error and the shift of

the SYCP3 intensity maxima to the center of the lateral element therefore can explain the shorter peak-to-peak distance of 650 nm for SYCP3 on MAP-expanded spreadings.

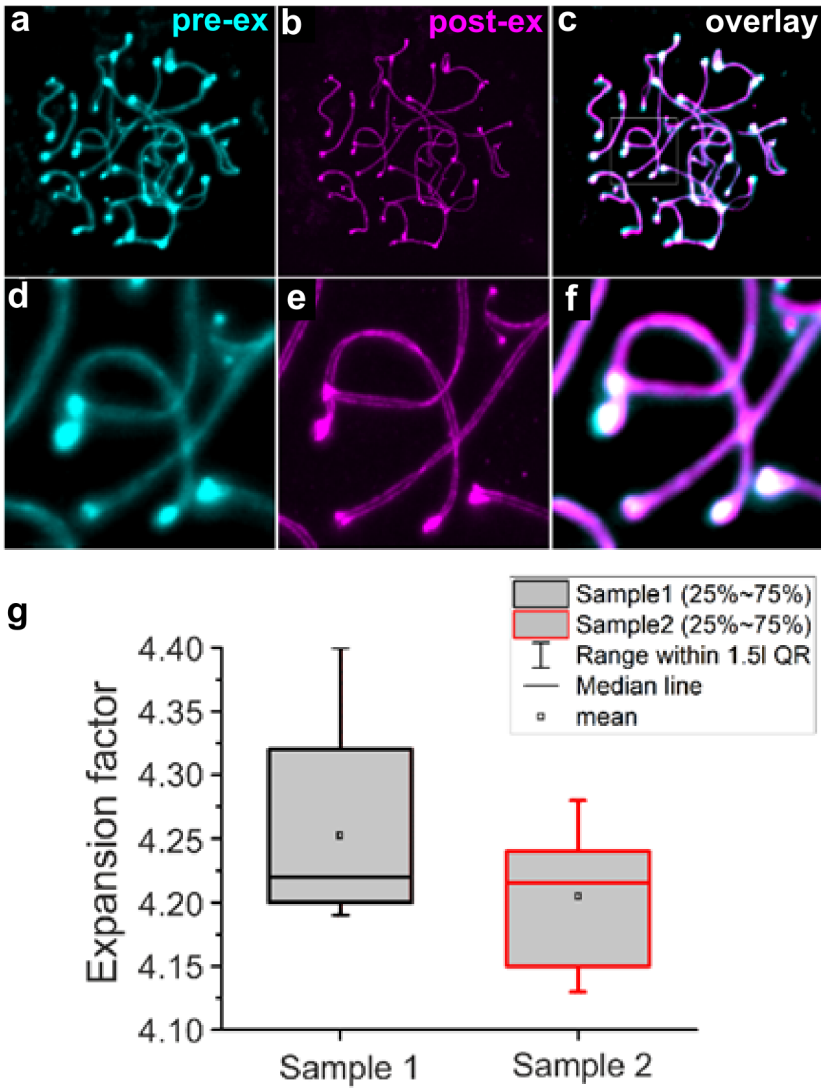


**Figure 27: Macroscopic expansion factor of MAP-SIM.** a, d. Re-scan confocal image (maximum intensity projection) of SYCP3 on unexpanded murine testes cells. The set of SCs of one spermatocyte nucleus are visualized through the detection of the lateral element protein SYCP3. SYCP3 is labeled with Alexa Fluor 488. b, e. Re-scan confocal image (maximum intensity projection) of the same set of SCs shown in (a,d) after expansion through the MAP approach. SYCP3 is labeled with SeTau647. Note the distinguishable separation of the two SYCP3 strands in the magnified post-expansion image (e). c, f. Overlay of the pre- and post-expansion images (a-b.). The overlay of the structures was achieved through rigid image registration. In the next step, the unexpanded SCs were transformed into the expanded SCs, generating an overlay image where the unexpanded and expanded SCs are indistinguishable through similarity transformation. g. The dilation that is necessary for the unexpanded SCs to match the dimension of the expanded SCs in the similarity transformation overlay determines the macroscopic expansion factor. The macroscopic expansion factor of MAP is ~x4.2. Figure adapted from [164].

A visual analysis was sufficient to detect larger discrepancies in the signal integrity, such as the apparent breaks in the SYCP3 signal resulting from U-ExM while compar-

ing the different expansion approaches. The isotropy of a method can however not be judged by visual analysis alone. A common method to quantify whether the structure of interest expanded isotropically is to generate a deformation vector field by overlaying a pre-expansion and post-expansion image of the structure through non-rigid transformation (b-spline) as shown in Figure 28. Based on the vector map, the root-mean-squared error of the expansion can be calculated. For the MAP-SIM expansion of the synaptonemal complex, this process revealed only minimal distortions introduced by the expansion process (Figure 28), validating the isotropy of the MAP-SIM experiments.

Next, the potential of MAP-SIM regarding the acquisition of larger data sets of the SC was evaluated. Indeed, the signal intensity of SYCP3 on MAP-expanded samples remained sufficiently high throughout acquisition to allow for structured illumination reconstructions of up to 80 x 80 x 15 $\mu m^3$ (110 nm axial spacing) as shown in Figure 29a. For RCM acquisition of the MAP-expanded SCs, even stacks of 100 x 100 x 30 $\mu m^3$ (200 nm z-steps) could be acquired (Figure 29b,c.).

### 4.2.2 Molecular details of the SC axes uncovered by MAP-SIM

As mentioned earlier, MAP-SIM provides a higher labeling density compared to other super-resolution techniques. The higher labeling density in post-expansion labeling approaches is linked to the expansion of the epitopes prior to immunolabeling, which improves epitope accessibility. Due to the higher labeling density, post-expansion approaches have the means to unveil greater morphological detail.

One striking morphological feature of the synaptonemal complex is the occasional splitting of the lateral elements into two or more sub-lateral elements (subLEs). The phenomenon has been observed across species from animals to yeast to plants using different electron microscopic techniques (histological sections, whole-mount preparations, spreadings) [155, 171, 172, 173, 174, 175, 176, 177]. The phenomenon could however not yet be resolved on the light microscopic level.

Murine spermatocytes contain 40 chromosomes that synapse as bivalents of the respec-

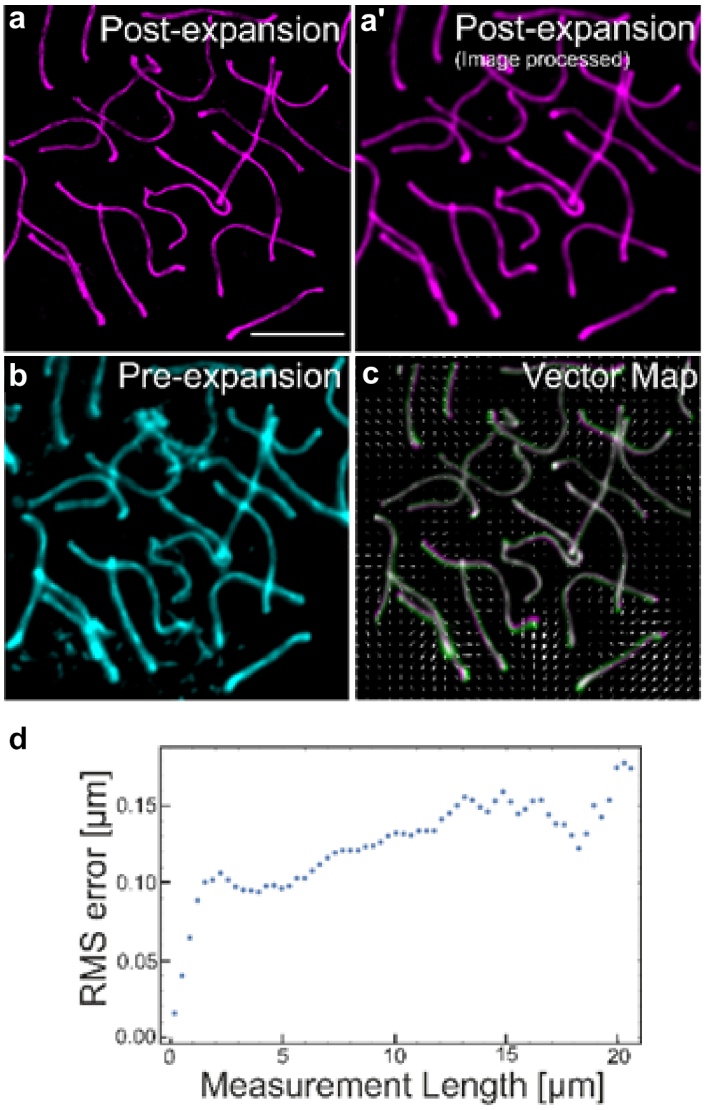


**Figure 28: Isotropy of MAP-SIM.** a. MAP-SIM image (maximum intensity projection) of SYCP3 localized on murine testes spreadings. SYCP3 was labeled with SeTau647. a'. MAP-SIM image of SYCP3 shown in (a) post-processed with a Gaussian blur for distortion analysis. b. Corresponding unexpanded image of (a, a'.). SYCP3 was initially labled with Alexa Fluor 488. c. Deformation vector field based on the overlay of (a') and (b) through non-rigid transformation (b-spline). d. The root-mean-square (RMS) of length measurements after MAP-SIM. The calculation revealed minimal distortions introduced by the expansion process. Scale bar: 20 $\mu$m. Figure adapted from [164].

tive homologs along the entire length of the synaptonemal complex in preparation for recombination. One lateral element hereby associates with one pair of sister chromatids. The observation of the occasional doubling of the lateral elements led to speculation that each subLE might associate with one sister chromatid in order to prevent recombination between sister chromatids while maintaining chromatin cohesion [178].

The lateral element consists of SYCP2 and SYCP3 fibers. In 2014, Syrjänen *et al.* resolved the crystal structure of human SYCP3 which revealed a tetrameric antiparallel assembly of the protein exposing its N-terminal DNA binding sites at either side [106].

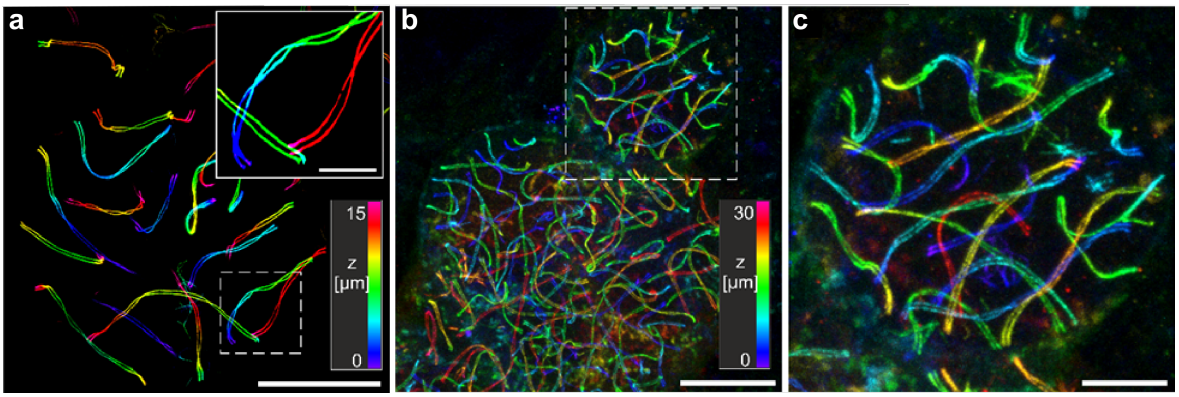


**Figure 29: Large 3D acquisitions of MAP expanded SCs imaged with SIM and re-scan confocal microscopy.** a. 3D MAP-SIM large field of view acquisition of SYCP3 on murine testes spreadings. The field of view was 80 x 80 $\mu m^3$ for a z-stack of 15 $\mu$m acquired at 110 nm axial spacing. The inlet shows a magnified view of the boxed region of (a). SYCP3 was labeled with SeTau647. b,c. 100 x 100 x 30 $\mu m^3$ 3D re-scan confocal acquisition of SYCP3 on MAP-expanded murine testes spreadings. SYCP3 was labeled with SeTau647. c. Magnified view of boxed region of (b). Scale bars: a. 15 $\mu$m (inlet: 5 $\mu$m), b. 25 $\mu$m, c. 10 $\mu$m. Figure adapted from [164].

In vitro, binding to stretches of DNA causes the 20 nm long protein to self-assemble into higher-order fibers which resemble the lateral elements [106]. Despite nanoscale resolution provided by *d*STORM, and comparable super-resolution techniques, the documentation of subLEs is limited to electron microscopic techniques.

In this work, the higher labeling density achieved by the MAP-SIM enabled the resolution of the SYCP3 signal splitting into two or more fibers per strand, which is equivalent to the observed subLEs. The degree of SYCP3 fraying hereby seems to increase with the progression of meiosis. In pachynema, the individual strands split in two, which can be observed frequently at sites where the helical SC twists (lateral view) as shown in figure Figure 30 and Figure 31 as well as at the ends of the SYCP3 strands (Figure 30a-d.). The observed bifurcation of single SYCP3 strands was validated by protein distribution analysis. A bimodal distribution of individual SYCP3 positive strands with a decreased signal intensity compared to a frontal view analysis of two SYCP3 strands confirmed the bifurcation of an individual SYCP3 strand. In late pachynema/ early diplonema the fraying appeared to increase, observable in form of multistrandedness along the length and at the ends of the SC (Figure 30e-g.).
These observations are in agreement with documentation of subLEs in murine spreadings on the EM level [176]. In this context, an organization of multiple SYCP3 strands into two compact subLEs through interaction with the two sister chromatids has been proposed [175]. EM micrographs of murine silver-stained spreadings also showed a bi-

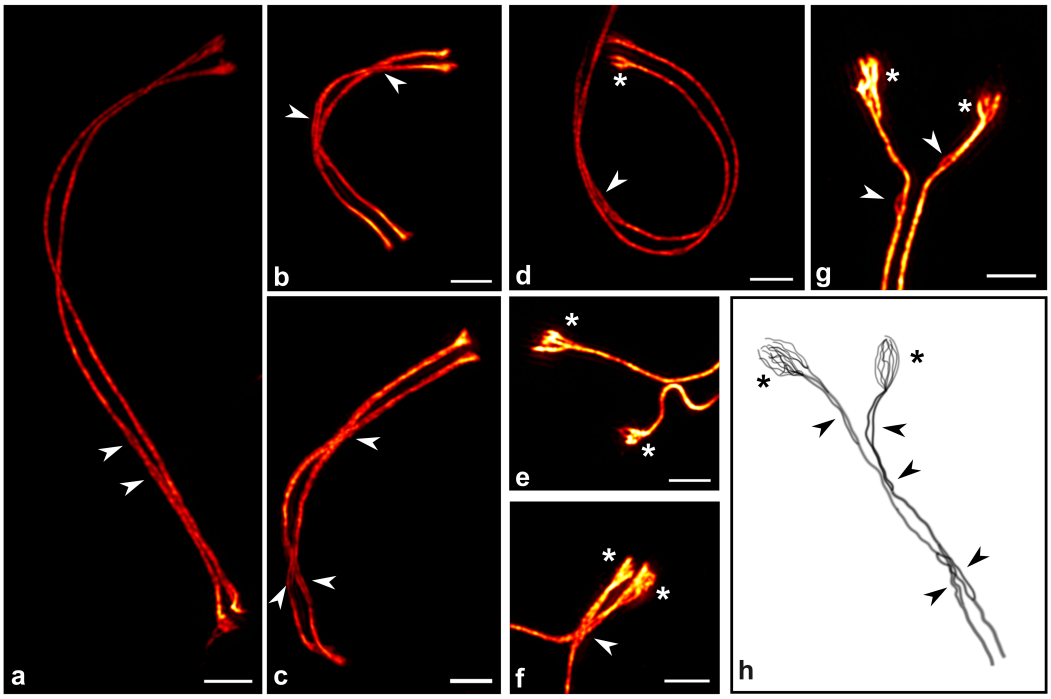


**Figure 30: Sub-lateral elements (SubLEs) visualized by immunolocalization of lateral element protein SYCP3 on MAP-SIM expanded SCs.** a-g. The SYCP3 signal shows occasional bifurcation (arrowheads) along the two strands of the SC (a-d) and various degrees of fraying at their ends (asterisks) depending on the respective pachytene stage (d-g). The fraying seems to increase with the progression of meiosis, specifically at the ends of the SCs. In mid-pachytene (d) the ends appear split in two, while in late pachytene/ early diplotene (e-g) the fraying increases beyond bifurcation. h. Representation of the lateral element strand splitting in two and fraying at its end observed as observed in electron micrographs of SCs according to Figure 4b/c of del Mazo and Gil-Alberdi,1986 [177] and Figure 10c of Dresser and Moses, 1980 [174]. Scale bars: a-g. 2 $\mu$m. Figure adapted from [164].

furcation or multistrandedness of the axes most frequently in unpaired regions [177].

In this work, the fraying of the axes was resolved for the first time by light microscopy, using MAP-SIM (Figure 30). Correlating the degree of fraying with meiotic events that occur during individual prophase stages reveals implications about the function of the axes at the respective stage. While the homologs are fully synapsed (mid-pachynema), doubling of the axes is frequently observed and potentially linked to the association of the sister chromatids with the lateral elements, preventing intrahomolog recombination. When desynapsis starts (late pachynema/ early diplonema), the lateral elements disperse into individual SYCP3 fibrils, in agreement with the overall gradual disassembly of the SC (Figure 30). In mammals, the organization of the axes into subLEs is conserved in both autosomes, as well as the XY pair [179, 180]. In the XY pair, synapsis is confined to the pseudoautosomal region. Accordingly, considerable

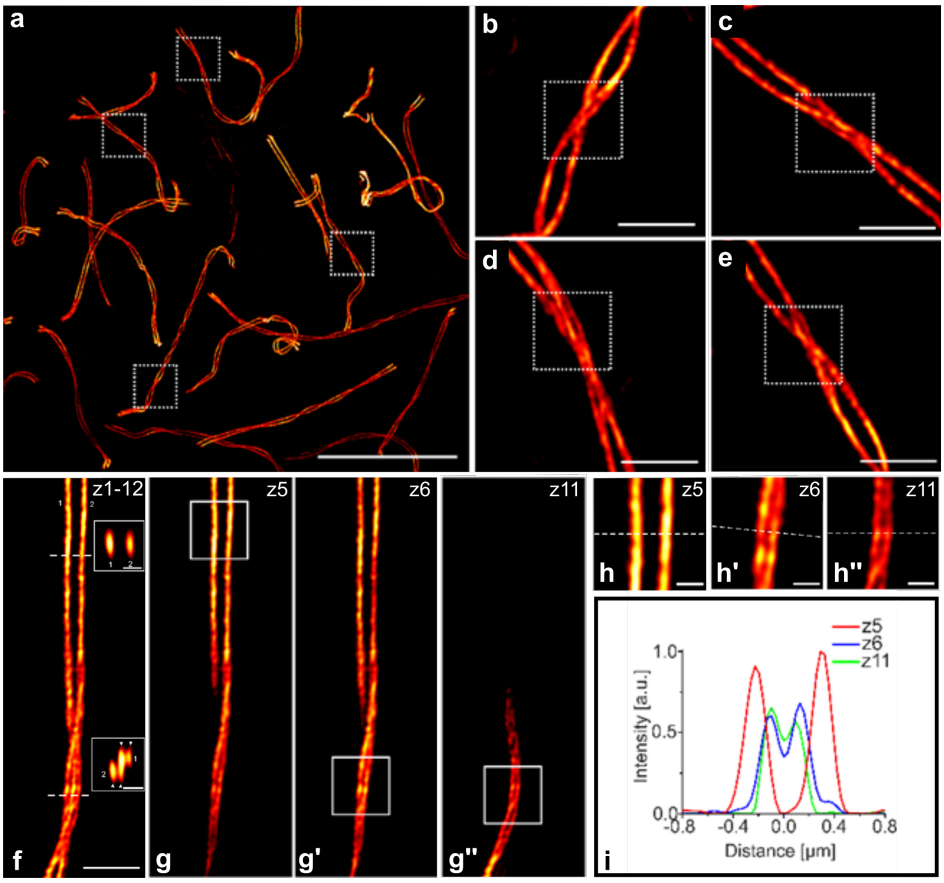


**Figure 31: Frequent observation of sub-lateral elements (subLEs) at the transitions between frontal and lateral view of the SC.** SubLEs visualized by immunolocalization of SYCP3 on MAP-SIM expanded SCs. SYCP3 was labeled with SeTau647. a. Various MAP-SIM expanded SCs. The boxed regions highlight the transitions between the frontal and the lateral view sections of the SC where the bifurcation of the individual SYCP3 strands was frequently observed. b-e. Magnified view of boxed regions of (a). f. Maximum intensity projection of a MAP-SIM z-stack (12 images; axial spacing: 110 nm) of a single SC. The two SYCP3 positive strands are numbered (1,2). In frontal view sections (upper dashed line), the two strands of the SC can be distinguished as individual signals (1,2). At the transition between the frontal and lateral view (lower dashed line), a single SYCP3 strand splits in two (arrowheads xz-view lower inlet). g,g',g". Individual z-slices of the z-stack shown in (f). Z5 shows a frontal view section of the SC visualized by the two approximately parallel SYCP3 strands. Z6 and Z11 show sites where the SC transitions between the frontal and lateral view. Here, the signal of a single SYCP3 positive strand splits in two (strand 1 for z11 and strand 2 for z6). h,h',h" show the magnified view of the boxed regions of g-g". Line profiles for the protein distribution analysis were introduced at the sites that are highlighted by the dashed lines. i. Corresponding intensity profiles of signal regions of z5-z11 (dashed lines) plotted into one histogram. Note the bimodal distribution of the signal of z6 and z11 that reflects the bifurcation of the individual SYCP3 strand at this site as well as the decrease in signal intensity compared to the bimodal distribution of the two frontal view SYCP3 strands of z5. Scale bars: a. 20 $\mu$m, b-f. 2 $\mu$m, h,h',h" 1 $\mu$m. Figure adapted from [164].

fraying in unpaired regions of the XY pair has been resolved in the present work (Figure 32).

### 4.2.3 Complex network organization of the SC central region

In the frame of this work, establishing a suitable expansion microscopy protocol for nuclear spreadings of murine spermatocytes was intended as a complementary ap-

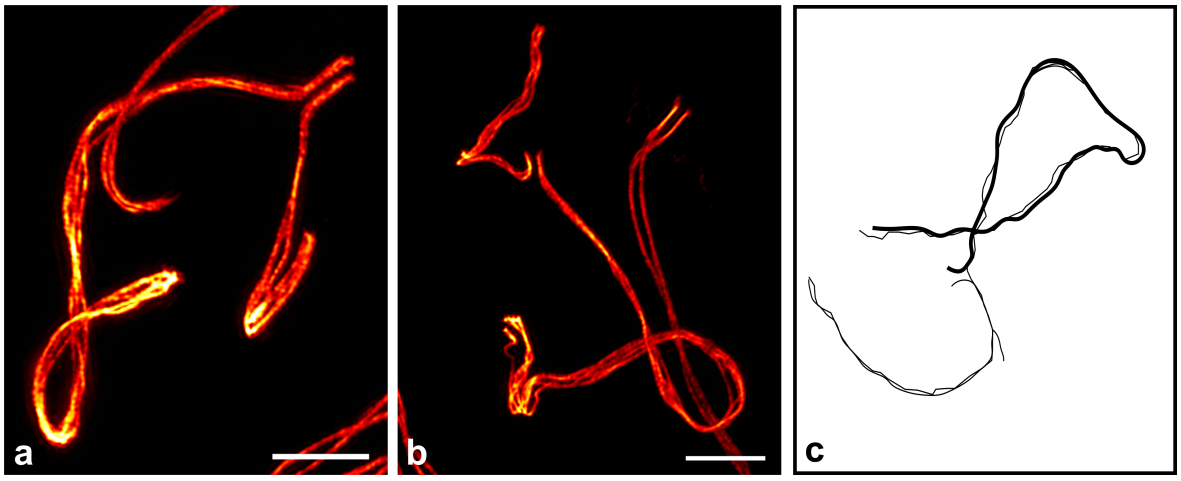


**Figure 32: Sub-lateral elements (SubLEs) of the XY pair visualized by immunolocalization of lateral element protein SYCP3 on MAP-SIM expanded SCs.** a,b. Unpaired regions of the XY pair show a strong degree of fraying in MAP-expanded SCs. c. Fraying of LEs associated with unpaired regions of the XY pair modelled after Figure 3a of del Mazo and Gil-Alberdi,1986 [177]. Scale bars: a-b. 4 $\mu$m. Figure adapted from [164].

proach to electron tomography in challenging the suggested multilayered organization of the SC. As mentioned earlier, the higher labeling density achieved by expansion microscopy can provide a more fine-grained depiction of the organization of the central element compared to other super-resolution techniques such as *d*STORM. Figure 24 and Figure 30 show that MAP-SIM provides a similar spatial resolution compared to *d*STORM. The respective images exhibit similar details of the molecular architecture of the SC previously only resolved by EM.

So far, the quality of the expanded samples had only been elucidated for the localization of a single protein, SYCP3. To analyze the organization of the central element, at least dual color experiments consisting of one component of the lateral element and one component of the central element (here: SYCP1-N and SYCE3) are required. SYCP3 visualizes the helical nature of the SC and serves to identify lateral views of the SC represented by twists in the SYCP3 (or SYCP2) signal. In these lateral views, the organization of the central element can then be evaluated.

Prior to this evaluation, the isotropic expansion and preservation of molecular detail in multicolor experiments had to be assessed. Therefore protein localization distributions of triple localizations of SYCP3, the N-terminus of SYCP1 and SYCE3 were generated and compared to localization data of the same proteins acquired by *d*STORM.

According to the dSTORM based localization map of SC proteins (see above), the central element proteins follow monomodal localization distributions with a width of 39.8 ± 1.1 nm for the SYCP1 N-terminus and 67.8 ± 2.1 nm for SYCE3 in frontal views of the SC. The broader signal distribution of SYCE3 indicates that SYCP1 is located at the center of the CE and that the proteins interact beyond the N-terminus of SYCP1. These findings are in accordance with a recent study of ExSTORM performed on nuclear spreadings [181]. In the respective study, the SYCP1 N-terminus is located approximately 110 nm from the SYCP3 labeled lateral element towards the center of the SC. The C-terminus is only localized 25 nm from the SYCP3 signal towards the CE of the SC, which corresponds to a localization of the SYCP1 C-terminus to the inner edge of the lateral element [181].

The triple localizations of SYCP3, SYCP1-N and SYCE3 on MAP-SIM expanded murine testes spreadings that were conducted in the frame of this work were initially analyzed visually and through manual protein distribution analysis in frontal views of the SC. Here, the two central element proteins localized in between the two strands of SYCP3. The SYCE3 signal appeared to localize outside of SYCP1-N, which was confirmed by the broader signal distribution of SYCE3 compared to SYCP1-N (Figure 33a-c.). An in depth line-profiler protein distribution analysis confirmed the notion of SYCP1-N being localized at the center of the central element, while SYCE3 resides more at the periphery of the CE. The analysis of 17,607 line profiles from 97 MAP-SIM SC images (2 separate experiments) revealed monomodal signal distributions of 161.5 ± 1.3 nm width for SYCP1-N and 229.3 ± 1.2 nm for SYCE3 in frontal view sections of the SC. SYCP3 was distributed bimodally with a peak-to-peak distance of 640 ± 21.6 nm (The individual intensity profiles shown in Figure 33c revealed a bimodal distribution for SYCP3 of 667.0 ± 7.1 nm width, 214 ± 6.9 nm for SYCP1-N and 258.3 ± 4.8 nm for SYCE3). These results, specifically the broader distribution of SYCE3 compared to SYCP1-N, are in accordance with the findings of the above mentioned *d*STORM study. The matching results between *d*STORM and MAP-SIM validate the suitability of the MAP expansion microscopy technique to evaluate the molecular organization of the central element in multicolor experiments.

Successful acquisition of *d*STORM images depends on efficient photoswitching of or-

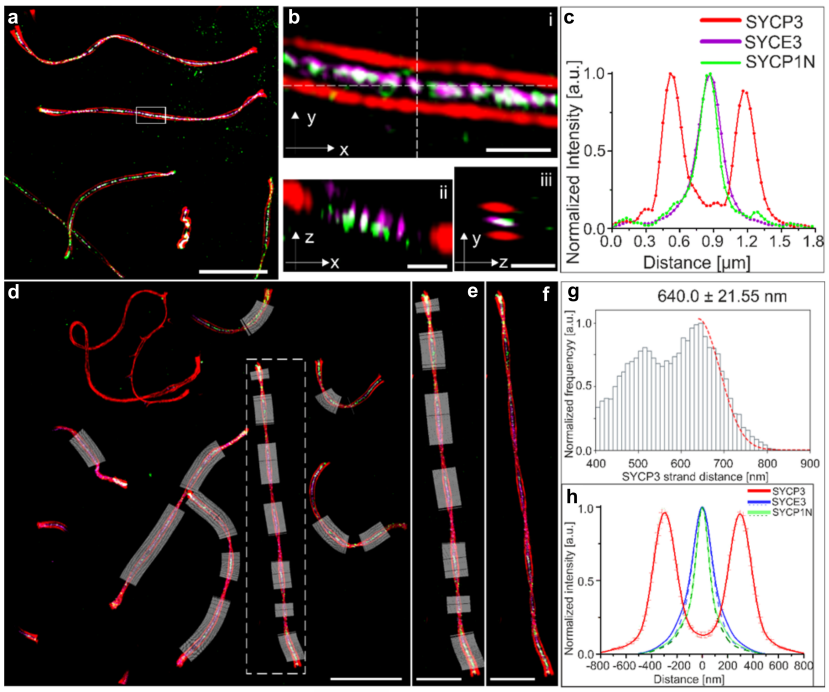


**Figure 33: Protein distribution of SYCP3, SYCP1-N and SYCE3 in frontal view sections of MAP-expanded SCs imaged with SIM.** a. Three-color-SIM image (maximum intensity projection) of SYCP3 (red), SYCP1-N (green) and SYCE3 (magenta). b.Magnified view of the boxed region in (a): (ii) Orthogonal view of horizontal white dashed line in (i). (iii) Orthogonal view of vertical white dashed line in (i). c. Transverse intensity profile perpendicular to the orientation of the SC shown in (b). The section reflects the bimodality of the SYCP3 signal separated by 667.0 nm ± 7.1 nm that circumscribes the monomodal signal of SYCP1-N (FWHM: 214.7 nm ± 6.9 nm) and SYCE3 (FWHM: 258.3 nm ± 4.8 nm). d. Maximum intensity projection of triple localization of SYCP3, SYCP1-N and SYCE3 on MAP-expanded SCs imaged with SIM. Line profiles (white) at frontal view sections along the SCs were introduced using the 2-channel mode of the Line Profiler tool where the SYCE3 signal is used as a criterion for the center and the orientation of the SC. SYCP3 is labeled with SeTau647, SYCP1-N labeled with Alexa 488 and SYCE3 with Alexa 568. e. Magnified view of boxed region shown in (d) with (e) and without (f) respective line profiles. g. Histogram of the average peak-to-peak distance of SYCP3 determined by 17,607 line profiles of 97 MAP-SIM images (2 separate experiments). The fit of a half-normal distribution function to the histogram reveals an average distance of 640.0 ± 21.55 nm for the inter-strand distance of SYCP3 in frontal view sections of the SC. h. Average intensity profiles corresponding to the data set of (g). Dashed curves show the averaged protein distribution of line profiles of SC frontal view regions. Solid lines represent the averaged protein distributions along the entire SC. SYCP1-N and SYCE3 are overall distributed in a monomodal fashion. Along the entire SC, the width of these monomodal distributions equals 161.5 ± 1.3 nm for SYCP1-N and 229.3 ± 1.2 nm. The analysis of only SC frontal views resulted in a signal width of 160.2 ± 1.1 nm for SYCP1-N and 207.5 ± 0.78 nm for SYCE3. Scale bars: a. 10 $\mu$m, b. 1 $\mu$m, d.10 $\mu$m, e,f. 5 $\mu$m. Figure adapted from [164].

ganic dyes in oxygen depleted thiol-buffer and is therefore limited to one or two-color experiments, with Cy5 and Alexa Fluor 647 as the best suited fluorophores [182, 183]. The results of the 2015 *d*STORM based study on the molecular architecture of the synaptonemal complex conducted by Schuecker et al. are therefore predominantly based on single localizations that are integrated to a joint localization map of SC proteins post-acquisition [127].

In order to address the question of a bilayered organization of the SC, the lateral view SC sections of the triple localization of SYCP1-N, SYCE3 and SYCP3 were analyzed by determining the signal distribution of the proteins. Initially, the respective intensity line profiles were introduced at only a few of the sites where the SC twists. In these lateral views, the individual signal distributions of SYCP1-N and SYCE3 had widely varying shapes. Some histograms supported a bimodal or a multimodal distribution of SYCP1-N or SYCE3, while others suggested a monomodal distribution. Overall, the signal distributions support a far more complex organization of the CE (Figure 34) in accordance with the complex CE organization revealed by ET presented earlier in this thesis.

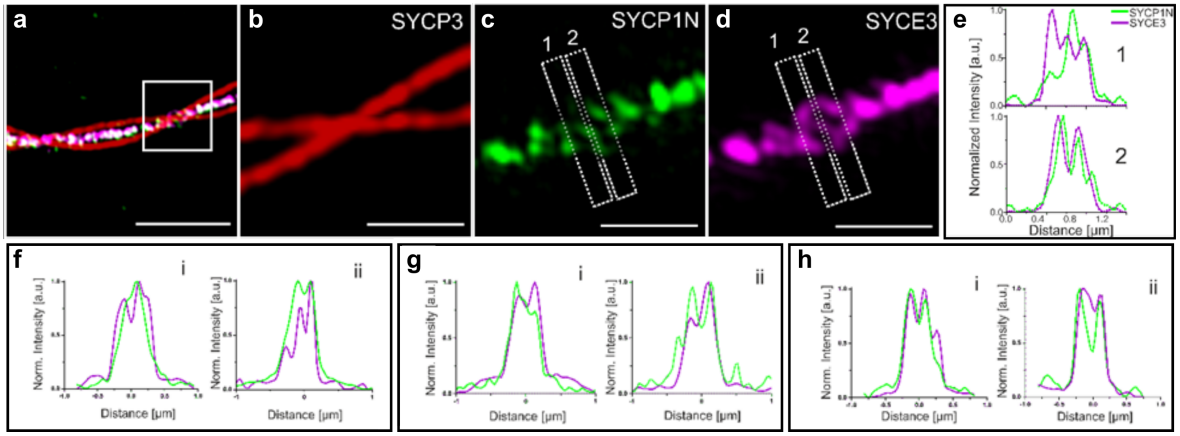


**Figure 34: Complex protein distributions of the N-terminus of SYCP1 and SYCE3 at individual sites of lateral view sections of the synaptonemal complex.** a. MAP-SIM image of SYCP3 labeled with SeTau647 (red), SYCP-1 labeled with Alexa 488 (green) and SYCE3 labeled with Alexa 568 (magenta). Boxed region highlights lateral view section of the SC. b-d. Magnified view of boxed region of (a) showing the signal of SYCP3 (b), SYCP1-N (c), and SYCE3 (d). Two sites selected for protein distribution analysis are indicated with dashed rectangular boxes (1,2). e. Cross-sectional intensity profile of the selected sites shown in (c) and (d) reveal multimodal distributions of SYCE3 and SYCP1-N. f-h. Additional normalized intensity profiles of two selected regions at lateral view sections of SCs each (i and ii; for reference see [164]) that support a bimodal, multimodal or monomodal distribution of SYCE3 and SYCP1-N. Scale bars: a. 3 $\mu$m, b-d. 1 $\mu$m. Figure adapted from [164].

To determine the average signal distribution of SYCP1-N and SYCE3, the average intensity profile across all lateral view sections of the SC was determined. The resulting intensity profile shows a clear monomodal distribution for both SYCP1-N and SYCE3.

The averaged intensity distributions of the N-terminus of SYCP1 and SYCE3 support the organization of the central element proteins of the SC into a single layer (Figure 35). The improved labeling density provided by MAP-SIM additionally reveals the

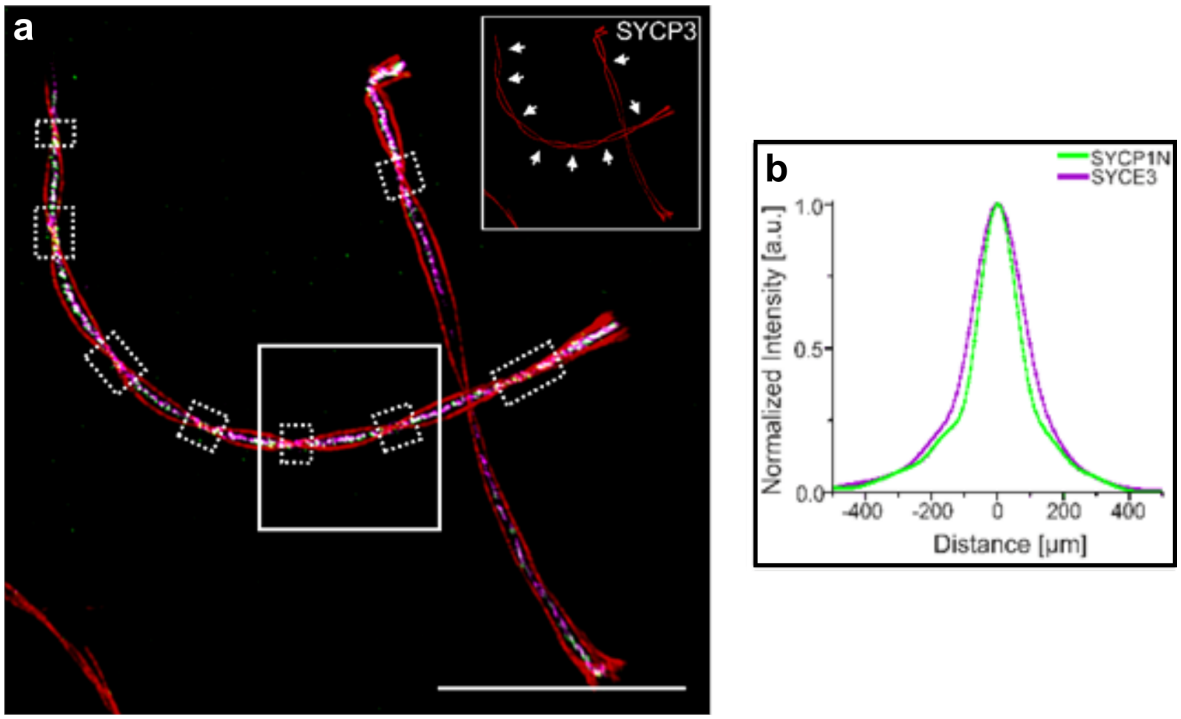


**Figure 35: Average protein distributions of the SYCP1 N-terminus and SYCE3 support a monolayered organization of the SC central region.** Triple localization of SYCP3, SYCP1-N and SYCE3 on MAP-expanded murine SCs. SYCP3 is labeled with SeTau647 (red), SYCP1-N with Alexa Fluor 488 (green) and SYCE3 with Alexa 568 (magenta). Lateral view sections of the SC are indicated by white dashed boxes. A solid white box highlights the site of the SC that was analyzed in Figure 34. The inlet shows only the SYCP3 channel. Here arrows indicate the lateral view sections of the SC. b. Averaged profile of all cross-sectional intensity distributions highlighted with dashed boxes in (a). The N-terminus of SYCP1 and SYCE3 follow monomodal distributions of 168.0 ± 1.1 nm for SYCP1-N and 211.43 ± 0.89 nm for SYCE3 (single Gaussian fitting). Scale bar: 10 $\mu$m. Figure adapted from [164].

organization of the central element proteins into a complex network at certain individual locations in lateral view sections, as shown in Figure 34. These results are in accordance with the results of the 3D ET derived data presented in this work.

## 4.3 Discussion

In the present work, the molecular architecture of the murine synaptonemal complex (SC) was resolved in order to lay a quantitative basis for the understanding of its structure-function relationship. To resolve ultrastructural detail of the SC, 3D nanoscale information is required. Therefore, in this thesis, the two nanoscale techniques electron microscope tomography (ET) and expansion microscopy (ExM-SIM) were used to acquire 3D data of the SC. Based on these data, quantitative measurements were performed to uncover the stoichiometry and the distribution of the SC proteins. ET hereby served to reveal the morphological characteristics of the SC archi-

tecture on the EM level, while expansion microscopy was used to analyze the protein distributions of the individual SC proteins on a light microscopic level.

A prerequisite for the generation of precise quantitative data lies in finding the ideal conditions for the respective approach. Therefore, as a first step, improved workflows for ET and expansion microscopy of the SC have been established in this work.

For ET, chemical pre-fixation was combined with freeze substitution (after HPF). Chemical pre-fixation stabilizes the (ultra)structure of the spermatocytes while substituting the cellular water by organic solvent in the cold results in less extraction. This improved sample preparation (see Chapter I) in combination with higher computational power allows the acquisition of tomograms with a high lateral ($< 1$ nm) and z-resolution (3-4 nm) compared to previous SC ET studies and allows for manual segmentation of the SC components [137].

For expansion microscopy, three different approaches - ultrastructure expansion microscopy (U-ExM), protein retention expansion microscopy (Pro-ExM) and magnified analysis of the proteome (MAP) - were applied to nuclear spreadings and compared based on their expansion factor and preservation of ultrastructural detail. MAP outperformed the other protocols with excellent structural preservation at an expansion factor of $\sim$x3. Expansion microscopy has already been combined with either structured illumination microscopy (SIM) or STORM to elucidate the molecular organization of the synaptonemal complex in two recent studies [163, 181]. In 2018, Cahoon et al. combined traditional expansion microscopy with structured illumination microscopy to elucidate the molecular architecture of the synaptonemal complex in *Drosophila melanogaster* [163]. The expansion protocol was conducted on germarium tip tissue and includes a dehydration step, embedding of the germarium tips in tissue freezing media, cryosectioning of the material into 10 $\mu$m sections and mounting of the sections on a coverslip. Sectioning was required to locate the sample as close to the coverslip as possible and entailed the use of an oil immersion objective. Alternative spreading of the SCs directly onto the surface of the coverslip, as performed in the frame of this work, results in the localization of the proteins close to the coverslip and allows the use of a water immersion oil that reduces chromatic aberration while imaging the hydrogel.

Spreadings further obviate the need for dehydration and cryosectioning, providing a quick and effective way to study the synaptonemal complex and nuclear proteins overall.

Combining MAP with structured illumination microscopy (SIM) achieves a spatial resolution of 20-30 nm, comparable to other super-resolution techniques, such as *d*STORM. The main difference between MAP-SIM and, e.g., *d*STORM is the higher epitope accessibility of the post-expansion labeling technique that provides a continuous staining of the proteins. Other advantages of MAP-SIM over *d*STORM are the possibility to perform multicolor super-resolution microscopy that is only limited by available laser lines and the acquisition of 3D super-resolution images of large expanded samples. During acquisition, spherical aberrations were controlled by using a water immersion objective as mentioned above. Finally, in the frame of this work, the Line Profiler[3] software was developed by Sebastian Reinhard, which enables the robust analysis of protein distributions in multiple channels, required for the calculation of the expansion factor.

The accuracy of measurements conducted on the 3D ET derived model of the SC and the MAP-expanded SC acquired by SIM were validated by measuring well-documented distances within the SC. For the ET derived 3D model, the central region width was determined as the distance between the inner edges of the lateral element. With 114 nm ± 17 nm this distance is in accordance with the ∼100 nm wide central region determined in a variety of previous studies [155, 156, 157, 158]. For reliable signal distribution analysis of SC protein localizations in MAP-expanded nuclear spreadings and expansion factor calculation, previously analyzed *d*STORM data was re-evaluated with the Line Profiler Software. The Line profiler software determined a peak-to-peak distance of 220 nm in accordance with the previously determined value based on *d*STORM [127].

For the quantitative analysis of the three-dimensional organization of the synaptonemal complex, the focus was mainly cast on the transverse filament protein SYCP1. Murine SYCP1 consists of 993 amino acids, the majority of which constitute a large central alpha-helical core, that is framed by unstructured N- and C-terminal ends [97]. The protein arranges into homodimers (same polarity of the alpha-helices) via the alpha-

[3] `https://doi.org/10.5281/zenodo.2643213`

helical core (aa 101-783) [110, 111].

Based on the 3D ET derived model of the SC, key metrics of the transverse filaments (TFs), such as the number, length and diameter of the TFs were quantified. The number of roughly 80 transverse filaments per micrometer hereby matches the 50-80 TFs/$\mu$m (upper limit) described in hamster [165]. The density of the transverse filaments (measured at the insertion site of the TFs into the central element) was determined to 1046 TFs/$\mu m^2 \pm 253$.

For the diameter of the transverse filaments, values between 2 to 10 nm with an average of 5 nm have been reported. Occasionally, splitting of the thicker filaments into fibers of 2 nm thickness was observed [129, 130, 165, 184]. In accordance with the smaller fibers, the thickness of the transverse filaments has been estimated to roughly 2 nm in this work. A single alpha helix has a diameter of 1.2 nm, which translates into 2.4 nm for the diameter of a coiled-coil domain. This value closely matches the estimated 2 nm diameter of the transverse filaments (equal to the alpha-helical core of SYCP1). The reported splitting of transverse filaments was not observed in the frame of the present work.

Based on the 3D model of the SC, the length of the transverse filaments is roughly 90 nm. Noteworthy, this value is in accordance with the length of the large SYCP1 coiled-coil core of 900 angstroms as determined in a crystallographic study conducted by Dunce et al. in 2018 [113]. The length of the coiled-coil predetermines the width of the SC, as suggested by polymerization studies of SYCP1 [112].

As for binding partners, SYCP1 interacts with SYCP2 of the lateral elements through its C-terminal domain, while the N-terminus of SYCP1 has been shown to recruit SYCE3 and SYCE1 (which also interacts with SIX6OS1), followed by SYCE2 and TEX12 (in sequential order). Accordingly, immuno-EM localizations provided evidence for the ends of SYCP1 to locate to the central and lateral element [111, 128]. Due to the well preserved ultrastructure of the testes tissue that served as the source for the generation of the tomograms acquired in this work, the entire course of the transverse filament was modeled. The resulting 3D model of the SC revealed that large parts of the transverse filaments are embedded within the central and the lateral element. In early ET studies, the transverse filaments have been reported to directly connect the two lateral elements, breaching the entire central region (with only some

filaments that terminate in the central element [129, 130, 158]. This impression would be conveyed by two opposing transverse filaments (two TFs originating from opposite lateral elements) that interact in the central element. While this constellation has been observed, two other frequent pairings of transverse filaments have been detected in the central element of the 3D model generated in the frame of this work. A subset of TFs pair with another TF that originates from the same lateral element. Furthermore, single TFs have been observed. Intuitively, the arrangements suggest an asymmetric distribution of TFs in the synaptonemal complex. Indeed, quantifying the number of transverse filaments based on their association with either of the lateral elements and comparing the total numbers between both sides of the SC resulted in a difference of roughly 21%, confirming the asymmetry of the meiotic structure.

The pairing of transverse filaments that originate from the same lateral element ties in with a model of human SYCP1 that was recently proposed by Dunce et al. [113]. Based on crystals of parts of SYCP1, the authors suggest that two parallel SYCP1 dimers congregate into a tetrameric assembly near the central element through close interaction. According to their model, branching would be observed where the tetramer decomposes into the individual TFs [113]. While coiled-coil domains indeed have the property to self-assemble in vitro (e.g., in a crystal where other proteins and nucleic acids are absent), the morphological data generated in the present study did not support a tetrameric assembly of SYCP1. The average minimum distance between pairs of parallel TFs determined on the basis of the 3D ET derived model of the SC was approximately 20 nm. This distance is too large to support the close tetrameric assembly proposed by Dunce et al. [113]. Furthermore, no branching of the TFs was observed in the present work.

The lateral element is composed of SYCP3 and SYCP2, the latter of which interacts with both SYCP1 and SYCP3 [103, 110, 104, 114]. SYCP1 and SYCP3 do however not interact directly with each other [103, 110, 104]. Similar to SYCP1, SYCP3 self-assembles in vitro via its large central alpha-helical domain. Crystallographic data revealed that SYCP3 arranges into repeating units of 20 nm length that consist of antiparallel tetramers of the protein [106]. The antiparallel conformation causes the corresponding four N-termini of a single tetrameric unit to be exposed at either side.

The N-termini carry DNA-binding domains that have been shown to bind to dsDNA through biochemical assays. These findings can be translated into a model where the SYCP3 units serve to organize the DNA of the meiotic chromosome axis into loops at a spacing of 20 nm [106]. Interestingly, the average minimum distance of the transverse filaments within the (SYCP3 positive) lateral element is also roughly 20 nm as determined in the frame of the present work. This novel insight can be integrated seamlessly into a model where individual SYCP3 units arrange into a lattice whose 20 nm long struts serve to organize the chromatin of the homologs into loops. Moreover, the SYCP3 units serve as a molecular spacer for the insertion of the transverse filament protein SYCP1 into the lateral element. In 2018, Dunce et al. proposed a similar model where each pair of neighboring SYCP1 C-termini arranges into a U-shape that coats one loop of DNA [113]. The C-termini of SYCP1 contain basic patches that are likely DNA binding sites. The asymmetric distribution of the transverse filaments uncovered in this work does however not support the pairing of neighboring SYCP1 C-termini suggested in the crystallographic study. The lack of morphological context in crystallographic studies can explain this discrepancy. On the basis of the morphological data presented here, an attractive model would consist of one SYCP1 dimer aligning with one SYCP3 tetramer. The mapping of SYCP1 to SYCP3 would be mediated by SYCP2, since SYCP1 and SYCP3 do not interact directly [103, 110, 104]. In this scenario, the repeating SYCP3 units would function as molecular spacers that present potential insertion slots for SYCP1 at a predefined minimum spacing [114, 185]. Not all slots would have to be occupied for the successful assembly of the SC. This would generate a more robust, yet flexible structure as compared to a system that demands a rigid periodic insertion of SYCP1 positive transverse filaments into the lateral element as the lack of a need for full occupancy of all slots is more forgiving towards disturbances. In addition, other factors might be involved in the distribution of transverse filaments within the synaptonemal complex since SC-like structures can even assemble between homologs in spermatocytes that lack lateral elements [65].

A central question surrounding the molecular architecture of the murine SC is whether the complex exhibits a layered organization. Early electron tomograms of insect SCs have revealed a bilayered organization of the central element (CE) in *Drosophila melanogaster* and a multilayered organization in *Blabs cribrosa* (3-4 layer) [129, 130].

As mentioned earlier, due to technical limitations at the time and the rather diffuse organization of the central element in mouse, no tomograms were acquired of the murine SC prior to the work presented here. The layered organization of the central element in mouse has however been investigated by analyzing the protein distribution of the central element proteins SYCE3 and SYCP1-N on the basis of immunoelectron microscopy (immuno-EM) and *d*STORM acquisitions [128, 127]. Using both approaches, SYCP1-N and SYCE3 showed a bimodal distribution in lateral view sections of the SC that infer a bilayered organization of the central element in mouse [128, 127]. While providing nanoscale resolution, the techniques give only a limited view of the organization of the central element. In mouse, 6 CE proteins have been identified thus far (SYCP1-N, SYCE1/2/3, TEX12 and SIX6OS1) [116, 151]. At an extend of 26 nm by 38 nm of the CE, this number of proteins presumably translates into a dense packing of the proteins within the CE. In conventional immunolocalization approaches, the antibody-antibody-label complexes (fluorophore or colloidal gold) localize within a radius of 20-25 nm around the antigen [186, 187, 188, 189]. The antibodies detect peripheral epitopes first, then epitopes at the center of the structure. In case of densely packed structures such as the central element, the peripherally bound antibody-antibody-label complexes thus likely hinder the accessibility of central epitopes which would translate to the detection of two peripheral layers of SYCP1. Additionally, in both immunoelectron microscopy as well as single molecule localization microscopy (such as *d*STORM) the labeling density is limited which further compromises the structural resolution. In this work, MAP-SIM on the other hand provides a high labeling density due to the fact that the epitope is targeted after expansion, which significantly enhances epitope accessibility. As a result, the structural resolution is significantly higher as shown, e.g., by resolving the fraying of the SYCP3 axes which equals the occurrence of sub-lateral elements that could previously only be detected by electron microscopy. Protein distributions of SYCP1-N and SYCE3 of MAP-SIM expanded SCs revealed a far more complex organization of the central element than previously described. Occasionally, the high labeling density enabled even the resolution of individual transverse filaments which is reflected in the respective bi- and multimodal signal distributions. Overall, the N-terminus of SYCP1 shows a monomodal distribution (averaged intensity profiles) in lateral views of the SC. This monolayered organization of the central element of the SC supports the EM findings of this work. Both visual and mathematical analyses of

the EM tomographic 3D model of the SC revealed that the transverse filaments (TFs) are organized into a single large layer. Within this layer the TFs do not follow a rigid organization, but show a far more complex distribution than the previously proposed bilayer.

To conclude, here, a first quantitative 3D model of the murine synaptonemal complex was generated. The improved ultrastructural preservation of electron microscope tomographic samples in this context revealed essential metrics of the transverse filaments and facilitated the tracing of the TFs within the central and lateral element. The analysis of the transverse filament distribution resulted in some unexpected findings. The commonly accepted schematic model of the SC shows the complex as a highly symmetric structure with opposing transverse filaments that are organized into two distinct layers. However, the morphological data obtained in the present work contradicts this model. Instead, it shows that the SC is an asymmetric structure in which the transverse filaments are distributed in a single layer, a configuration that enables adapting to the dynamic changes of the synaptonemal complex during prophase I. These new findings of the SC architecture were integrated in a novel model of the synaptonemal complex (see Figure 36 below).

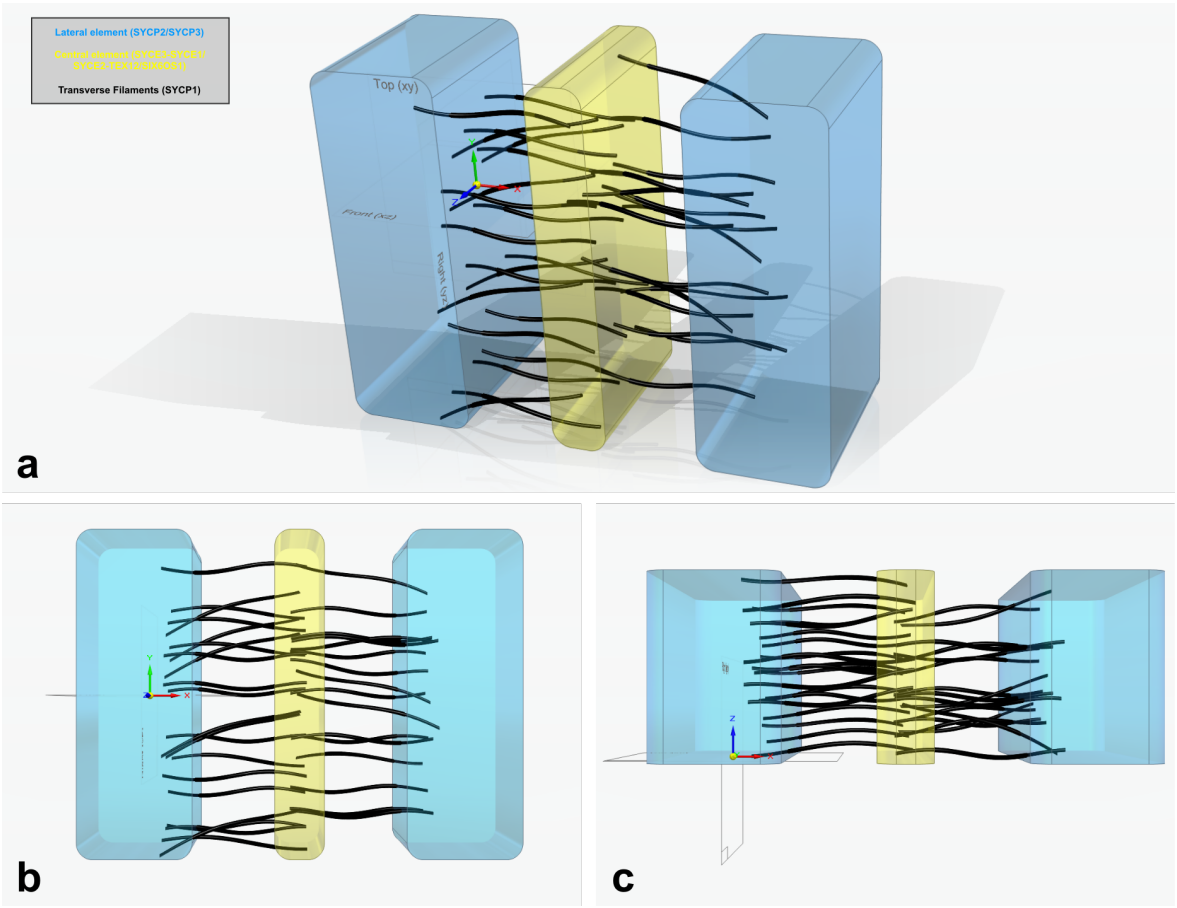


**Figure 36: Updated model of the murine synaptonemal complex.** Schematic model of the synaptonemal complex in mouse encompassing the novel findings of the present work. Note, the random, asymmetric distribution of transverse filaments (roughly 20% difference in transverse filament number between the two sides of the SC), the insertion of the transverse filaments into the lateral and central element and the different types of pairings of neighboring transverse filaments in the central element (parallel/opposite and single pairings). Lateral elements in blue, central element in yellow and transverse filaments in black. a. Perspective view of the SC model, b. frontal view of the SC model, c. top view of the SC model. Figure adapted from [90].

# 5 Chapter III: The molecular architecture of the meiotic telomere attachment site

Prophase I is the longest of the meiotic phases and is characterized by the essential processes of synapsis, recombination and segregation. A multitude of functional and regulatory biomolecules are involved in the successful execution of these processes. The biomolecules are hereby supported in their function by a component of movement. At the onset of meiosis, the meiotic telomeres attach to the nuclear envelope through a meiosis specific shelterin complex and begin to move along its plane. Movement continues throughout prophase I at different rates depending on the prophase stage. The telomeres move fastest in zygotene where pairing and synapsis is administered [190, 32].

The biological relevance of the telomere movements overall has been linked to the regulation of interhomolog interactions during homolog pairing in preparation for segregation. However, a consensus on the function of the telomere movements does not exist to date. A contribution of telomere movement to homolog pairing and the prevention of non-homologous pairing has been proposed. Telomere movements could further be involved in the resolution of chromosome entanglements, direct the entry and exit to bouquet stage and/or monitor the number and location of crossover sites [32].

While their precise functional role remains elusive, prophase telomere movements are essential to the success of meiosis. Mutations that disturb meiotic progression directly affect telomere movement. Accordingly, pharmacological inhibition of prophase telomere movement leads to premeiotic arrest. Mutations in mouse SYCP3 cause a zygotene like arrest due to a lack of axial/lateral element assembly that prevents synapsis and prohibits DNA repair [191]. In these knockout mice telomere movements are significantly reduced in early prophase stages (leptotene, zygotene) [32]. Vice versa also disruptions of the telomere movement affect the progression of meiosis. Pharmacological inhibition of the cellular machinery that moves the homologs during meiosis leads to the reduction of telomere movement to a minimum or even the entire absence of movement while at the same time induces defective chromosome pairing, synapsis and segregation [192, 193].

In most organisms, including mice, the force necessary to generate nuclear telomere movements is generated by dynein running on microtubule tracks. The force is then transduced onto the meiotic telomeres by LINC (Linker of Nucleoskeleton and Cytoskeleton) complexes [81, 194, 131, 123]. The role of LINC complexes as mechanotranductors in meiotic telomere movement is particularly conserved [84]. The protein complexes consist of SUN (Sad-1/UNC-84) domain proteins and KASH (Klarsicht/ANC-1/Syne/homology) domain proteins [195, 196, 46, 85]. In mouse, they are comprised of type II inner nuclear membrane proteins SUN1/2 and germ cell–specific outer nuclear membrane protein KASH5. While the N-terminus of SUN1/2 interacts with the nuclear lamina and the meiotic telomere binding proteins, the N-terminus of KASH5 connects to the microtubule motor system (see Figure 37) or in rare cases such as S. cerevisiae to flowing actin filaments.

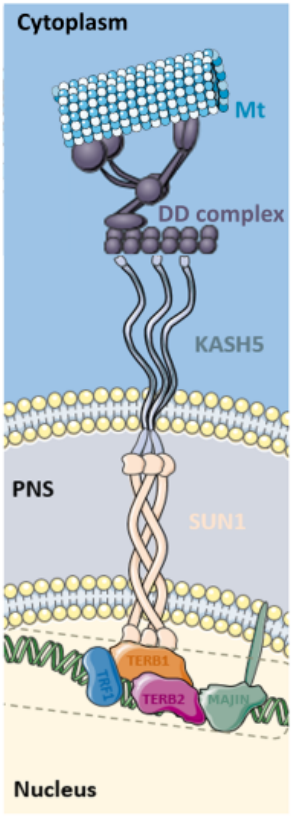


**Figure 37: Schematic illustration of the meiotic LINC complex at telomere attachment sites in mouse.** The murine LINC complex is comprised of SUN1 (and SUN2; not shown) and KASH5. The inner nuclear membrane protein SUN1 interacts with the meiotic lamina and the meiotic shelterin complex. In 2015, Shibuya et al. identified a meiosis specific shelterin complex that consists of TERB1, TERB2 and MAJIN. According to their model, TRF1 of the somatic shelterin complex hands over the telomeres to a meiosis specific telomere binding complex in early prophase. According to their data, in early prophase, during cap exchange, both TRF1 and the meiotic shelterin complex are present in a chimeric complex, which is displayed here. After the meiotic telomere complex has attached, their data supports a release of TRF1 from the tetrameric complex, terminating the telomere transfer from somatic to meiotic shelterin complex. In the perinuclear space, the trimeric SUN1 and three KASH5 proteins form the LINC complex via their eponymous domains. At the cytoplasmic end of the LINC complex which corresponds to the N-terminus of KASH5, the complex connects to the dynein-dynactin-microtubule motor complex. Figure adapted from [72].

As their high degree of conservation suggests, LINC complexes are essential to gametogenesis [194, 131, 85]. Deficiencies in either SUN1 or KASH5 lead to pre-meiotic arrest. Telomere movement is significantly reduced in the absence of SUN1 and completely obsolete in KASH5 knockout mice [32]. The residual movement in the SUN1 knockout mice can be assigned to the redundant function of SUN2 in forming the LINC complex

with KASH5.

Individual LINC complexes are assembled from heterotrimers of SUN1/2 and KASH5 through interaction of their eponymous C-terminal domains in the perinuclear space [75]. The C-terminus of SUN1 that resides in the perinuclear space hereby contains the coiled-coiled domain which enables trimerization [75]. This domain is characteristic for stress-bearing structural proteins, as it provides the molecule with elasticity [197, 198, 199] to withstand mechanical strain such as the shear forces applied to the LINC complexes at telomere attachment sites during prophase chromosome movements. In some cases, multimerization of KASH domain proteins has been described. In the context of meiotic KASH5 a potential multimerization between neighboring KASH5 proteins would lead to a higher order network of LINC complexes [75, 199].

Diffraction limited light microscopic localization of the meiotic LINC complexes on nuclear spreadings reveals focal accumulations of the proteins in close proximity to the ends of the SYCP3 signal. In structured illumination microscopy (SIM) acquisitions with an approximate two-fold resolution increase compared to standard widefield techniques, SUN1 and KASH5 signals appear distributed ring-like [85]. In the present work, the LINC complex components were localized in triple immunolocalizations together with SYCP3 using SIM and the novel super-resolution microscopy technique expansion microscopy (in combination with SIM).

The outer nuclear membrane LINC complex component KASH5 associates with microtubules through the minus-end directed motor dynein. In order to localize dynein and its cofactor dynactin at murine telomere attachment sites, immunogold localizations of the two proteins were conducted in the present work.

3D nanoscale resolution provided by, e.g., EM and super-resolution microscopy is required to increase our knowledge on the distribution and the stoichiometry of the LINC complexes. Unraveling the molecular architecture and stoichiometry of the LINC complexes will eventually lead to uncovering their structure-function relationship.

Opposed to somatic cells, the LINC complexes in meiocytes seem to concentrate lo-

cally at telomere attachment sites instead of being evenly distributed throughout the nuclear envelope. Due to their localization and morphology, accumulations of filamentous proteins emanating from the inner nuclear membrane into the cytoplasm at telomere proteins observed in EM micrographs were considered likely to be LINC complexes [68, 65]. Immunogold localizations of SUN1 and SUN2 have localized the inner nuclear membrane component of the LINC complex to these respective filament assemblies [70, 71]. Respective immuno-EM localizations of KASH5 that would presumably localize the outer nuclear membrane component of the LINC complex to the array of nuclear envelope spanning filaments have not been conducted yet.

In this work, as a first step towards characterizing meiotic LINC complexes in their morphological context, immunogold localizations of both components of the complex were conducted to ensure that the accumulation of filaments at the telomere attachment sites are indeed LINC complexes. Next, to generate quantitative data on the complexes within their morphological context, electron tomograms at telomere attachment sites with and without microtubules were acquired. The tomograms were segmented manually for components of the SC, the LINC complexes and microtubules to generate 3D models of the attachment sites. Based on these models, the amount, length and width of the LINC complexes were quantified. Further analyses were performed on the distribution of the LINC complexes, which ultimately resulted in a first estimation of the forces effective at telomere attachment sites.

## 5.1 Immunolocalization of the LINC and Dynein-Dynactin complex at telomere attachment sites

### 5.1.1 Localization of the LINC complex components SUN1 and KASH5 to meiotic telomere attachment sites

**According to Spindler *et al.* 2019a [72].**

Prior to generating a quantitative 3D model of LINC complexes at telomere attachment sites, the molecular identity of the LINC complexes at these sites has to be confirmed. Therefore, immunogold localizations of the LINC complex components SUN1 and KASH5 have been conducted.

The aim here was to detect the very cytoplasmic end of the LINC complex within its morphological context. Thus, an antibody was designed in the frame of this work that is directed specifically against the N-terminus of KASH5 (aa 71-83 and aa 89-104). Previous widefield acquisitions of KASH5 or SUN1 and SYCP3 have revealed that the proteins localize to the ends of the respective SYCP3 signal on nuclear spreadings. To validate the localization of the newly designed KASH5 N-terminal antibody to the same site, triple immunolocalizations of SUN1 (aa 427-722) [200], KASH5 and SYCP3 as a marker for the axial/lateral elements, were performed on nuclear spreadings and imaged using structured illumination microscopy. In accordance with the previous immunolocalization data [85, 47], both SUN1 and the N-terminus of KASH5 localized to the end of the SYCP3 signal (Figure 38). Depending on the view, it appears that SUN1 localizes distal to the end of the SYCP3 signal and KASH5 distal to SUN1. Overall, SUN1 and KASH5 largely co-localize (Figure 38). In the work presented here, the respective proteins were visualized in four of the prophase stages, leptonema, zygonema, pachynema and diplonema. With the progression of prophase I, the signal of SYCP3, SUN1 and KASH5 appears to condense and the overall signal intensity seems to increase. However, no quantitative measurements of signal intensity were performed here. In order for a robust signal characterization, a quantitative analysis is required. The aim of this work was to validate the localization of KASH5-N to the end of the SYCP3 signal. The following section serves as a brief description of the observation of the SUN1 and KASH5 signals in different prophase stages (Figure 38). In leptotene, SYCP3 appears as short linear stretches of the assembling axes. SUN1 and KASH5 localize to the ends of the SYCP3 signal as small foci that appear slightly elongated. In zygotene, the SUN1 and KASH5 foci seem slightly enlarged. While the signals of the LINC complex components appear marginally elongated in frontal and lateral views, the proteins present round in top views. This notion carries over to the later prophase stages pachytenema and diplonema (Figure 38). Here, the synaptonemal complex is fully assembled between the synapsed homologs. Therefore, the lateral element protein SYCP3 is observed as two strands per homolog pair. Accordingly, two foci of SUN1 and KASH5 localize to the end of the SYCP3 strands, one per strand. In the frontal views the proteins appear as elongated disks that curve slightly around the SYCP3 signal. In this view, the two signals of the individual proteins seemingly fuse to a single plate. In

top view however, it is apparent that two clearly separated foci for each of the LINC complex components localizes to the end of the two SYCP3 strands (Figure 38). In accordance with the earlier prophase stages of leptonema and zygonema, the foci appear round in top view. In lateral views, only one of the SYCP3 strands is visible, the second strand is hidden underneath the signal. Consequently, also only one SUN1 and one KASH5 foci is visualized in this view (Figure 38). Previous SIM images of SUN1 and KASH5 acquired by Horn et al., resolved the signals of both proteins as ring-like shapes in top views of the SC, i.e., at the tips of the SYCP3 signal [85]. In the work presented here, the signal of SUN1 and KASH5 did not display a ring-like shape. It is noteworthy that the targeted epitopes of SUN1 and KASH5 were compatible between the study conducted by Horn et al. and the present work. In case of KASH5, the N-terminus was localized (Horn et al.: human aa 9-24; present work: mouse aa 71-83 and aa 89-104) and for SUN1 larger epitopes oriented towards the C-terminus were targeted (Horn et al.: human aa 470-601; present work: mouse aa 427-722) both in the study of Horn et al., as well as in the present work, only N-terminus of KASH5 were localized. For SUN1, in both studies larger epitopes were detected (Horn et al.: aa 470-601; present work: aa 427-722). Still, in the present work SUN1 and KASH5 foci were detected, while Horn et al. reported ring-like shapes for both proteins. In the present work, smaller fluorophore-conjugated F(ab')2 fragments were used for the detection of the proteins. This can improve the accessibility of central epitopes, that might be blocked when regular IgGs are used. The blockage of central epitopes might cause the ring-shaped signals observed by Horn et al.. Another explanation for the difference in signal appearance might be related to the different reconstruction algorithms used for the generation of the SIM images (Horn: SoftWorX (Applied Precision); present work: SIM module in Zeiss Zen software).

In order to investigate the signal distribution of SUN1 and KASH5 at improved epitope accessibility, the LINC complex components were further visualized together with SYCP3 on expanded nuclear spreadings (MAP protocol) and imaged with SIM. A first respective acquisition of the LINC complex proteins shows the clear separation of the SUN1 and KASH5 signal at the 20-30 nm lateral resolution achieved by Ex-SIM (Figure 39). Also under the improved epitope accessibility provided by ExM, the signal of SUN1 and KASH5 corresponds to a single foci localizing to each of the SYCP3 strands

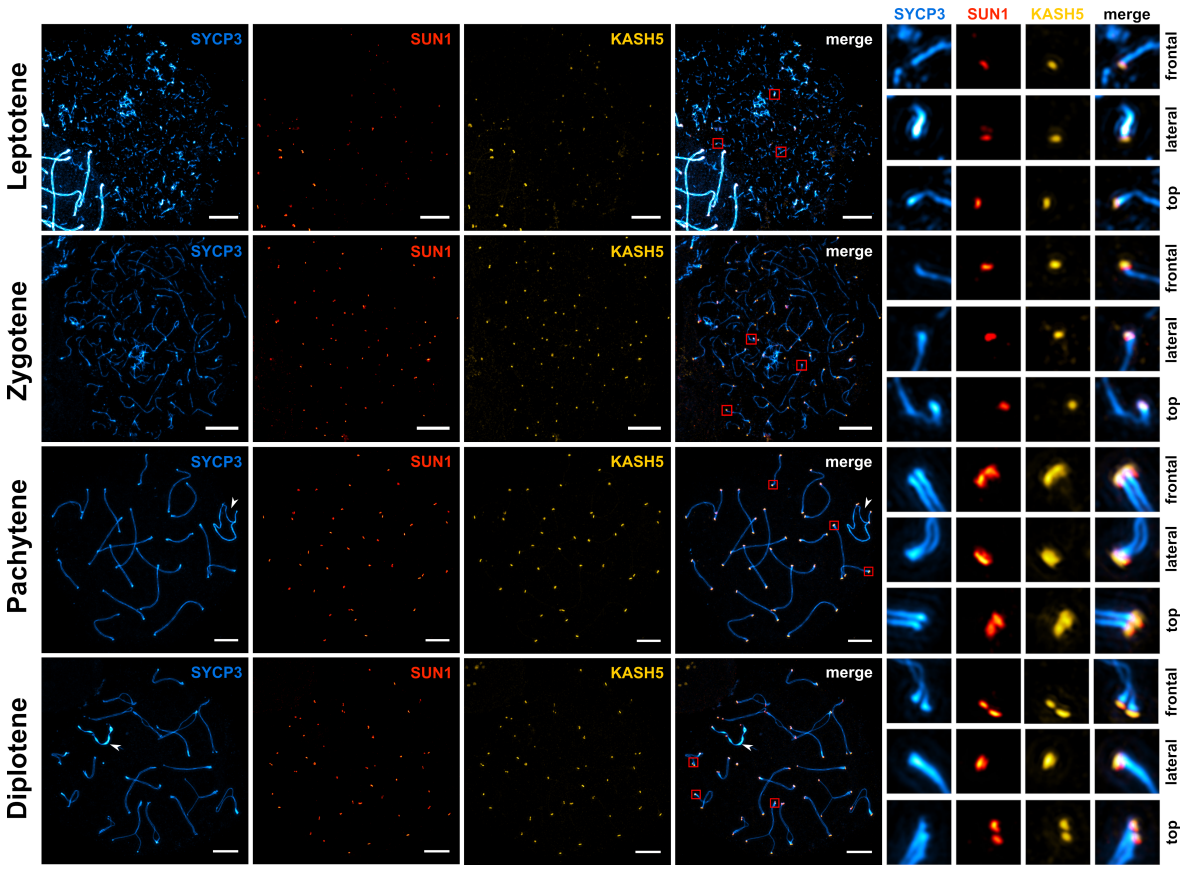


**Figure 38: Localization of LINC complex components SUN1 and KASH5 at meiotic telomere attachment sites in mouse.** SUN1 and the N-terminus of KASH5 were localized to the ends of the SYCP3 signal in four of the five prophase stages (leptonema, zygonema, pachynema and diplonema). Depending on the view, SUN1 localizes more proximal to SYCP3 compared to KASH5, but overall SUN1 and KASH5 co-localize at this magnification. The signals of SYCP3 labeled with SeTau647 (blue), SUN1 labeled with Alexa Fluor 488 (red) and KASH5 labeled with Alexa Fluor 568 (yellow) are shown separately and as a merge (maximum intensity projections). For each stage, frontal, lateral and top views of the SC were selected (red boxes in merge) and displayed as magnified views. In leptotene, SUN1 and KASH5 localize to the ends of short stretches of SYCP3 as slightly elongated foci. In zygotene, the LINC complex components localize to the ends of the unsynapsed single SYCP3 strands. In frontal and lateral views, the foci of SUN1 and KASH5 appear elongated at this stage, in top views round. In pachytene and diplotene, two SYCP3 strands of the fully assembled SC are visualized. Accordingly, two SUN1 and two KASH5 foci localize to the end of the two SYCP3 strands per homolog pair. In frontal views, the signals appear as two disks on the verge of fusion. In top views it is however apparent that two SUN1 and two KASH5 foci localize to the site, one foci per end of a SYCP3 strand each. In lateral views only one SYCP3, SUN1 and KASH5 signal is visualized. The other set of signals is not visible due to superimposition. Scale bars: 5 $\mu$m.

for each protein in pachytene spermatocytes contrary to the previously observed ring-like signals [85].

To confirm that the assemblies of filaments emanating from the inner nuclear membrane at meiotic telomere attachment sites are indeed LINC complexes, molecular mapping of SUN1 and KASH5 to these filaments is required. Former PhD student Johannes Schmitt of the Benavente group performed pre-embedding immunogold localizations

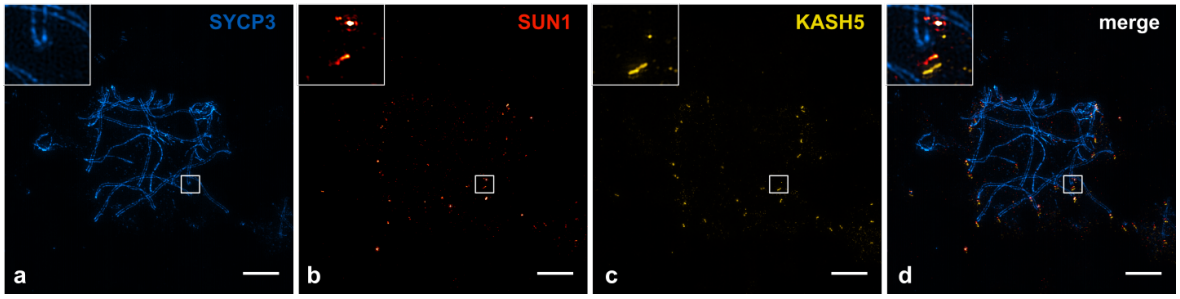


**Figure 39: Expansion microscopy of the LINC complex components SUN1 and KASH5 of murine testis spreadings.** SYCP3 (a) labeled with SeTau, SUN1 (b) labeled with Alexa568 and KASH5 (c) labeled with Alexa488 were triple localized on MAP expanded murine testis spreadings. In this preliminary localization, the potential of ExM to resolve the proteins of the LINC complex was shown. The SUN1 signal appears to reside in between the ends of the SYCP3 signal and the KASH5 signal. However, no channel alignment was performed for this acquisition. The SUN1 and KASH5 signal appear as two foci each that localize to the end of the SYCP3 signal. The insert in the upper left corner shows a magnified view of the boxed regions in a-d. Scale bar: 10 $\mu$m.

to localize SUN1 and SUN2 on murine testis tissue sections [70, 71]. For visualization he used a secondary antibody coupled to 1.4 nm nanogold, which was enhanced by a silver stain. In the respective electron micrographs that he acquired, SUN1/2 localize to and mostly in between the nuclear envelope at the telomere attachment sites. The anti-SUN1 and anti-SUN2 antibody used in these experiments are directed at the coiled-coil region of the proteins which resides in the perinuclear space [70, 71]. The SUN domain itself is globular and therefore not suited as an epitope.

In this work, the immunogold localization of SUN1 on frozen murine testis sections was reproduced using 6 nm colloidal gold as a marker. In accordance with the results of Johannes Schmitt [71], SUN1 localizes predominantly to the perinuclear domain of the filaments emanating from the inner nuclear envelope at meiotic telomere attachment sites (Figure 40). These findings further fit with the data and the models of the literature [85, 47].

The outer nuclear membrane component of the LINC complex, KASH5, has previously not been localized within its morphological context. As mentioned earlier, an antibody specifically directed against the N-terminus of the protein has been derived in the frame of this work to close this gap and detect the very cytoplasmic end of the LINC complex in its morphological context. Immuno-EM localizations of the N-terminal KASH5 antibody on frozen testis sections resulted in the exclusive localization of the gold markers to the cytoplasmic end of the filaments (Figure 40). Pre-embedding immunogold local-

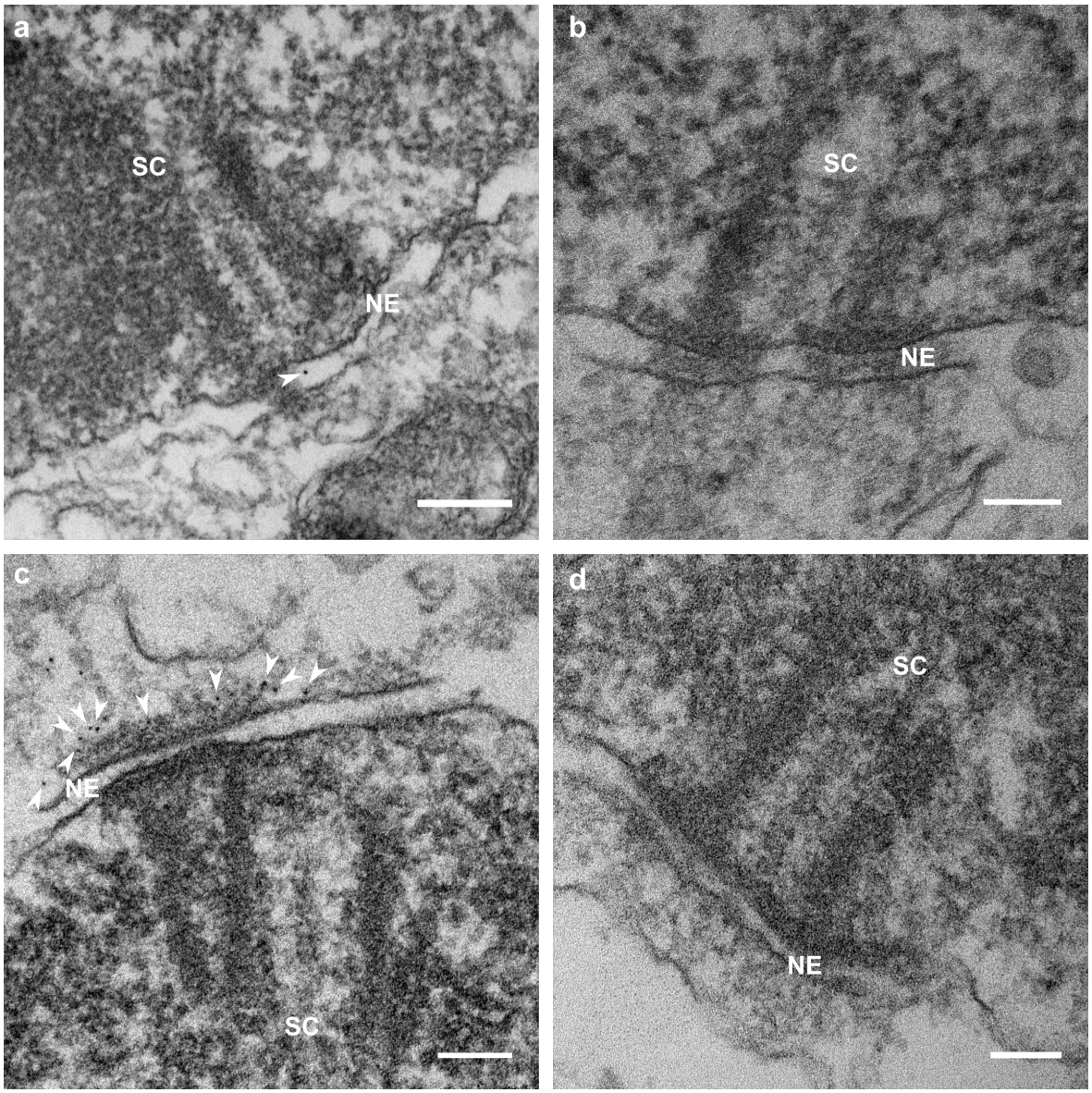


**Figure 40: Immunoelectron microscopic localization of LINC complex components SUN1 and KASH5 at meiotic telomere attachment sites in mouse.** a. Immunogold localization of SUN1 (aa 427-722 [200]) on epoxy embedded frozen sections (6 nm colloidal gold). Arrowheads point to gold markers that localize SUN1 to the perinuclear domain of the nuclear envelope (NE) spanning filaments that concentrate at telomere attachment sites. b. Negative control of SUN1 immunogold localization at telomere attachment site. For the negative control, the sections were only incubated with the gold-conjugated secondary antibody, not with the anti-SUN1 antibody. c. Immuno-EM localization of the N-terminus of KASH5 on frozen testis section (6 nm colloidal gold). The colloidal gold marker localizes exclusively to the cytoplasmic end of the filaments as indicated by arrowheads. d. Negative control of KASH5-N immunogold localization at telomere attachment site. For the negative control, the sections were only incubated with the gold-conjugated secondary antibody, not with the anti-KASH5-N antibody. SC: synaptonemal complex, NE: nuclear envelope. Scale bars: a. 200 nm, b-d. 100 nm. Figure adapted from [72].

izations of KASH5 repeatedly localized the protein to these sites using both colloidal gold and nanogold enhanced with silver (latter not shown) for the detection of KASH5.

Specific binding of the secondary gold-coupled antibody was secured by performing

control experiments applying only the secondary antibody to the sections, skipping the incubation with the primary antibody that targets either the KASH5 or SUN1 epitope (Figure 40). Here, gold particles did not localize to the end of the filaments (KASH5) or the perinuclear space (SUN1) which confirms the specificity of the gold signal for targeted localization of KASH5 and SUN1 (Figure 40).

In summary, this set of results provides clear evidence that the filaments that emanate from the inner nuclear envelope, bridge the perinuclear space and protrude into the cytoplasm at meiotic telomere attachment sites are indeed LINC complexes that connect the nucleo- with the cytoplasm. An interesting complementary experiment to verify the localization of the LINC complexes to telomere attachment sites would have been to acquire tomograms of KASH5 heterozygous mice which show reduced expression of KASH5 [85]. The reduced amount of KASH5 in these mice should show filaments that are shorter by the length of the LINC complex that KASH5 contributes. Unfortunately, these mice were not available for the present work.

### 5.1.2 Localization of cytoplasmic dynein at meiotic telomere attachment sites

In the frame of this work, the mechanotransduction machinery at meiotic telomere attachment sites has been investigated. On the sequence level, the outer nuclear membrane LINC complex component KASH5 possesses an N-terminal dynein-binding domain. Several studies have investigated the interaction between KASH5 and dynein using biochemical approaches [46, 85]. In 2012, Morimoto et al. performed immunoprecipitation experiments using antibodies derived against KASH5 and precipitated the p150Glued subunit of dynein [46]. One year later, Horn et al. co-immunoprecipitated the dynein heavy chain with a soluble form of KASH5 (KASH5$\triangle$K), inferring that KASH5 is an adaptor for dynein [85]. Using immunofluorescence microscopy, dynein has been visualized in the vicinity of meiotic telomere attachment sites. In wildtype zygotene spreads, SUN1 foci colocalized with dynein. On KASH5 null spermatocyte spreads the colocalization was absent from SUN1 foci [85]. In 2015, Lee et al. confirmed the role of dynein as a motor for meiotic chromosome movement through intraperitoneal injection of small molecule dynein inhibitor ciliobrevin A which stalled

chromosome movement [32]. The authors further showed the co-localization of dynein and KASH5 at meiotic telomere attachment sites using confocal microscopy [32]. While these approaches indicate the presence of dynein at telomere attachment sites, they do however lack the morphological context that electron microscopy techniques provide.

To date, the crowded cytoplasm has however thus far prohibited the visualization of cytoplasmic dynein within the morphological context. The large dynein-dynactin complex is highly dynamic and can adopt diverse conformations [201]. These conformations are so heterogeneous that even for a cryo-EM analysis conducted by Grotjahn et al. in 2018 [202] of isolated dynein-dynactin-BICD (DDB) complexes bound firmly to microtubules, common subtomogram averaging strategies were insufficient to resolve the structure of the flexible complex in 3D. The authors had to model parts of the complex by guided subtomogram averaging to reconstruct the whole DDB complex in 3D [202].

Alternatives to localize dynein-dynactin complexes at telomere attachment sites are indirect approaches such as immunoelectron microscopy. However in localizing dynein at these sites, several challenges arise. Firstly, the reliable detection of a protein with immunogold localizations strongly depends on a high copy number of the respective protein. Dynein-dynactin (DD) complexes are highly dynamic structures that are inherently rarely enriched at a certain location in the cell to surpass the detection limit. Dynein is further ubiquitously expressed in the cytoplasm. Even dyneins that would be located at telomere attachment sites by immunoelectron microscopy could therefore potentially also bind to diverse cargo in the crowded cytoplasm and could thus not be allocated unambiguously to the LINC complexes. This remains true even for DD complexes that would be located close to a microtubule which can be identified by eye at these sites as shown earlier in this work. Due to the size of the antibody-antibody complex the localization precision is restricted to a radius of roughly 25 nm from the epitope. Apart from meeting the detection limit and determining the precise localization of the detected epitope, another challenge in localizing dynein results from the decreased accessibility of the protein in the tight dynein-dynactin complex. Despite these challenges, an effort was made in the present work to localize both dynein and dynactin to meiotic telomere attachment sites. Therefore, several attempts were conducted to localize the proteins on 1% PFA fixated frozen sections (pre-embedding

staining; subsequent embedding in epoxy resin) using antibodies against p150Glued or the dynein intermediate chain with the intention to increase the possibility to detect the proteins in an enriched state. For detection, secondary respective secondary antibodies conjugated to either nanogold or 6 nm colloidal gold were used. Neither dynein nor dynactin were localized to the meiotic telomere attachment sites in the present work which can be attributed to the mentioned challenges in localizing dynein-dynactin complexes.

## 5.2 Electron microscope tomography of LINC complexes at meiotic telomere attachment sites

**According to Spindler *et al.* 2019a [72].**

Pachynema is one of the meiotic prophase stages in which telomere movement is relatively slow compared to the fast prophase movement that characterizes other stages, such as zygotene. Still, pachynema is ideally suited to resolve LINC complexes at meiotic telomere attachment sites, as telomeres are motile even if at a slower pace. Additionally, pachytene spermatocytes are easily identifiable in the electron microscope. Here, homologous chromosomes are fully synapsed and synaptonemal complex proteins are highly condensed. Consequently, the attachment sites appear as two electron-dense plates closely associated with the nuclear envelope on the cytoplasmic side and the tripartite synaptonemal complex on the nuclear side. The SC is present as the characteristic two extensive ribbon-like lateral elements which surround the central element. From the attachment plates, assemblies of filamentous LINC complexes span the nuclear envelope and protrude into the cytoplasm.

As mentioned earlier, advanced sample preparation for EM (Chapter 1) results in excellent structural preservation of pachytene spermatocytes for electron microscope tomography (EM tomography) of meiotic telomere attachment sites. Importantly, inner and outer nuclear membranes remain their regular spacing when using the approach established in the frame of this work, which is essential for quantitative measurements of nuclear envelope associated LINC complexes.

In frontal views, telomere attachment sites are about 400 nm wide and up to 200 nm

deep (see below). Thus, in order to acquire the entire structure in a single tomogram, testis tissue sections of 250 nm were used. For this part of the work, 11 of the acquired and reconstructed tomograms were manually segmented for the components of the synaptonemal complex, the nuclear envelope and the LINC complexes to create 3D models of the telomere attachment site (Figure 41). Due to the three-dimensional properties of the LINC complexes, entire filaments are hardly detected in a single virtual (reconstructed) section. However, moving through the stack of virtual sections, their axial trajectory is easily traceable following the criterion of continuity. Generally, supervised segmentation was carried out following strict pre-defined criteria to avoid introducing subjective bias to the data.

An initial visual analysis of the tomogram reconstructions and the corresponding 3D models reveals that the LINC complexes solely emanate from the attachment plates and are absent from other parts of the nuclear envelope as shown in Figure 42. Consequently, also the section of the nuclear envelope in between the attachment plates is virtually devoid of LINC complexes. Hence, each telomere attachment site contains two sets of LINC complexes, one associated with each attachment plate. The LINC complexes are not branching and are apparently also not interconnected with each other.

The initial visual inspection of the tomograms further reveals that only about 50 % of the annotated attachment sites (5/11) are close to a microtubule (Table 15). The microtubules in the analyzed tomograms were hereby oriented either longitudinally or transversally to the attachment sites in frontal views. Attachment sites with a microtubule were likely motile at the time of fixation, while attachment sites without were steady. To detect potential differences between the steady and motile attachments in subsequent quantitative and topological analyses, the tomograms were allocated to two respective groups: with and without microtubule.

### 5.2.1 Stoichiometry of the LINC complexes at meiotic telomere attachment sites

An essential aspect in characterizing a protein and its function within a multiprotein complex is to determine its copy number, size and shape in this context. Due to the

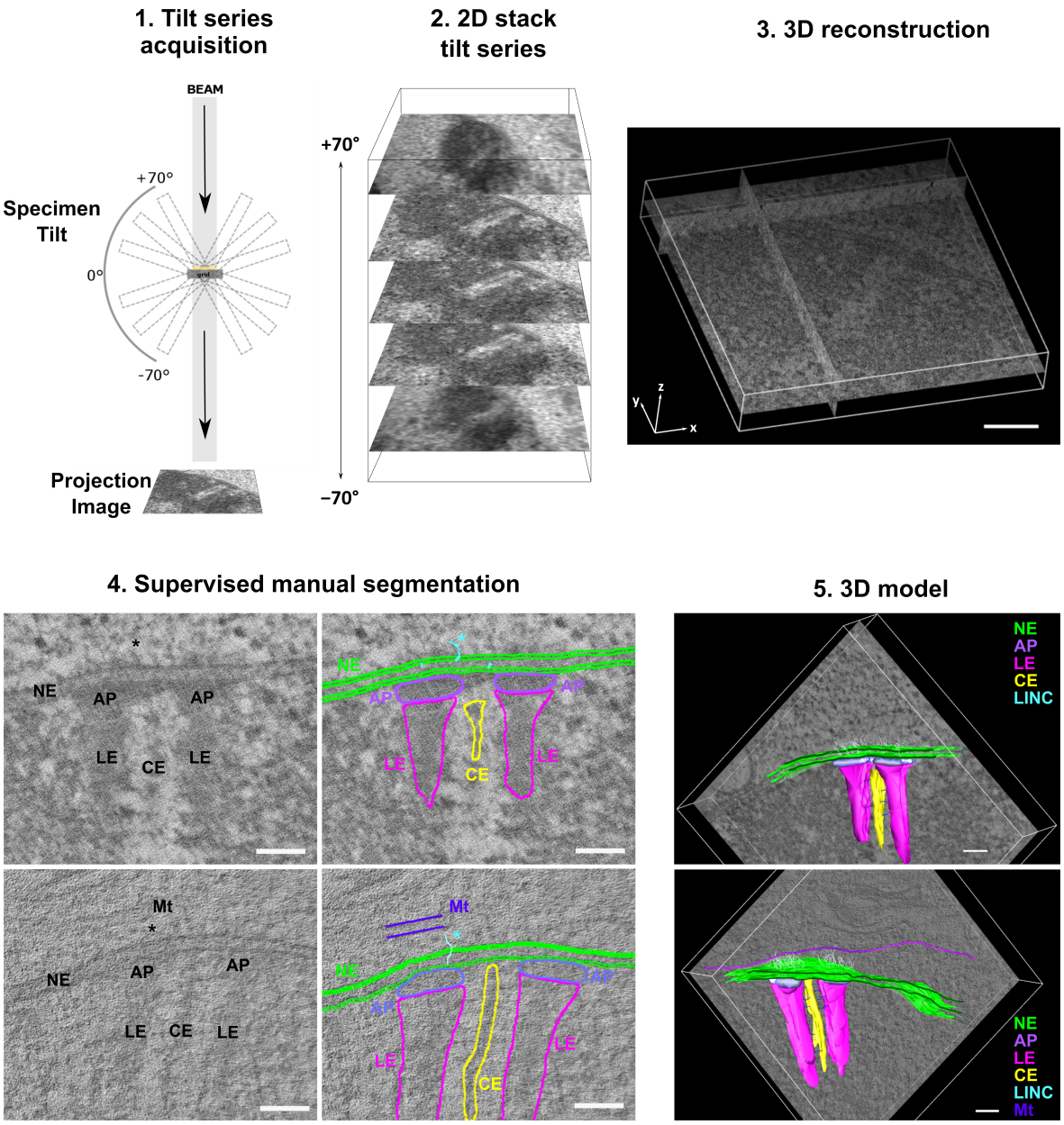


**Figure 41: Generation of 3D electron microscope tomographic model of meiotic telomere attachment sites with and without microtubules.** For the generation of a 3D electron microscope tomographic model of a single meiotic telomere attachment site, a double tilt series of 141 degrees per single tilt (1° increments) was acquired of an epoxy embedded testis tissue section of mouse, resulting in a stack of 282 tilt series projections. The original volume was reconstructed by using unspecific gold particles on the sections as landmarks for a weighted back-projection algorithm. The individual virtual sections of the resulting tomogram were segmented for the morphological components at meiotic telomere attachment sites that are relevant to the present study, such as the nuclear envelope (NE), the attachment plates (AP), the lateral (LE) and central element (CE) of the synaptonemal complex as well as the LINC complexes and depending on their presence at the site microtubules (Mts). The resulting 3D model was used for an in depth subsequent quantitative analysis of the LINC complexes at the site. Scale bars: 100 nm. Figure adapted from [72].

lack of 3D data on LINC complexes at meiotic telomere attachment sites, these key descriptors remained previously unaccounted for. In this work, the gap of the missing 3D model has been filled by supervised segmentation of meiotic telomere attachment sites in electron microscope tomograms of murine pachytene spermatocytes. Based on the

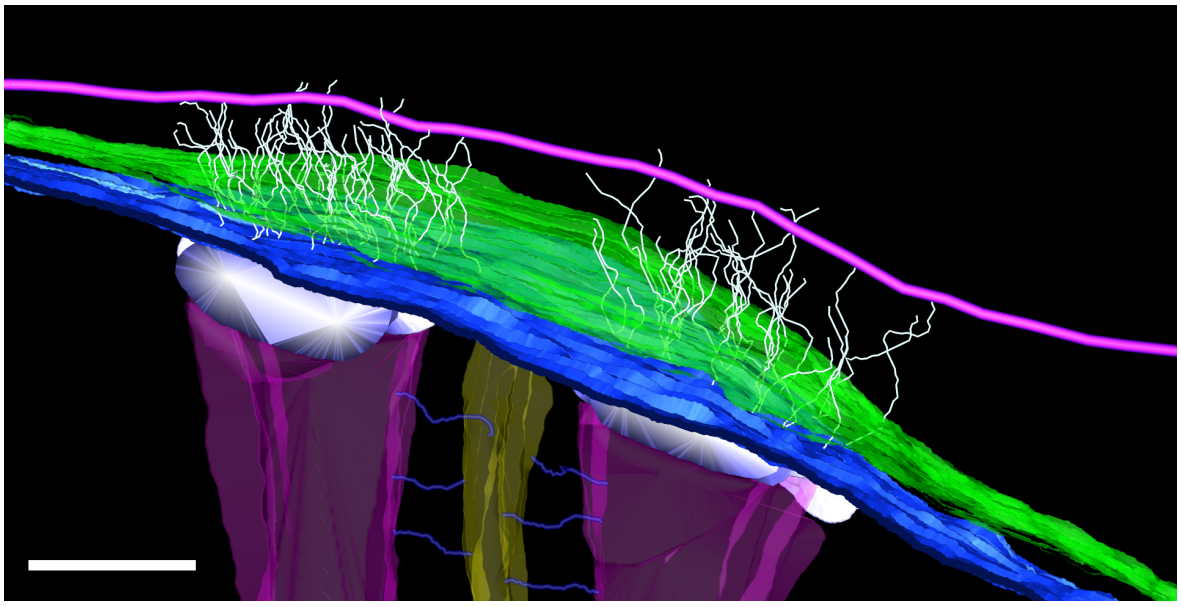

**Figure 42: 3D electron microscope tomography derived model of a murine telomere attachment site.** The model shows the segmented LINC complexes (light cyan), the nuclear envelope (inner nuclear membrane: dark blue, outer nuclear membrane: green), the attachment plates (lilac), the lateral (magenta) and central element (yellow) as well as a few transverse filaments (blue) of the synaptonemal complex and depending on their presence at the site microtubules (purple). The LINC complexes solely emanate from the attachment plates. Only 50 % of the attachment sites are close to a microtubules. Scale bar: 100 nm. Videos of telomere attachment sites with and without a microtubule are available on zenodo[a].

[a] `https://doi.org/10.5281/zenodo.3375530`

3D model, quantitative and topological data on the LINC complexes were extracted. In a first step, the amount and length of the LINC complexes at these sites were extracted using the IMOD console program imodinfo. Table 15 gives an overview of the number of the LINC complexes detected at the analyzed attachment sites as well as whether or not the attachment was associated with a microtubule. An average of 76 LINC complexes concentrate at a single telomere attachment site. This number is indifferent of whether an attachment with or without a microtubule closeby was analyzed, i.e., there was no significant data difference between these two data sets (two-sample Kolmogorov–Smirnov test, p=0.969).

LINC complexes are filamentous proteins, anchored in the inner nuclear envelope where SUN1 interacts with the meiotic lamina and chromatin binding proteins. After passing through the perinuclear space where the eponymous domains of SUN1/2 and KASH5 interact with each other, the outer nuclear envelope component reaches into the cytoplasm with its long N-terminal stretch. Based on the 3D model generated in the frame of this work, the length of the LINC complexes at telomere attachment sites is roughly

**Table 15:** Overview of the number of filaments of each analyzed attachment and closeness of a microtubule

| Attachment | Microtubule | Number of filaments |
|---|---|---|
| 1 | no | 69 |
| 2 | no | 104 |
| 3 | no | 77 |
| 4 | no | 64 |
| 5 | no | 63 |
| 6 | no | 80 |
| 7 | yes | 80 |
| 8 | yes | 67 |
| 9 | yes | 79 |
| 10 | yes | 88 |
| 11 | yes | 61 |

90 nm on average. There is no significant difference between LINC complexes at telomere attachment sites with compared to those without a microtubule (two-sample t-test; p-value=0.078). Filaments at attachment sites with a microtubule are on average 92 ± 20 nm long. In tomograms without a microtubule, LINC complexes are 91 ± 18 nm long. While the mean reflects the central tendency of the LINC complex length distribution, it does not report the potential existence of subpopulations of different lengths of LINC complexes at the attachment sites. To analyze the length data for these potential subgroups, the LINC complex lengths data were plotted as density distributions (Figure 43). The density curves of LINC complexes at attachment sites with and without microtubules reveal that the length data is distributed around a single mean length of 90 nm (Figure 43). The absence of other local maxima shows that the filaments at meiotic telomere attachment sites cannot be grouped into longer and shorter LINC complexes. The coiled-coil of SUN1/2 has been predicted to be 45 nm long [75]. The long N-terminal coiled-coil region of KASH5 consists of 200 amino acids. Consequently, the combined length of the LINC complex components should not exceed 100 nm. Still, the density distributions of the LINC complex lengths show outliers of individual filaments that are up to 160 nm long. The apparent mismatch in LINC complex length for a small number of segmented filaments is likely a result of the annotation criteria. For this study, the common criterion of continuity has been applied to the supervised segmentation. In the crowded cytoplasm of the spermatocytes it is however inevitable that cytoplasmic components appear to be continuous with the LINC complexes on occasion. The segmentation of these cytoplasmic extensions results

in a small subset of longer filaments due to the mistaken continuous progression. Overall, these outliers do not compromise the quality of the quantitative data since both the segmentation and subsequent analysis are statistical approaches. For this study, a total of 832 LINC complexes were analyzed. This large sample size grants a reliable reflection of the mean filament length of 90 nm and the LINC complex properties overall.

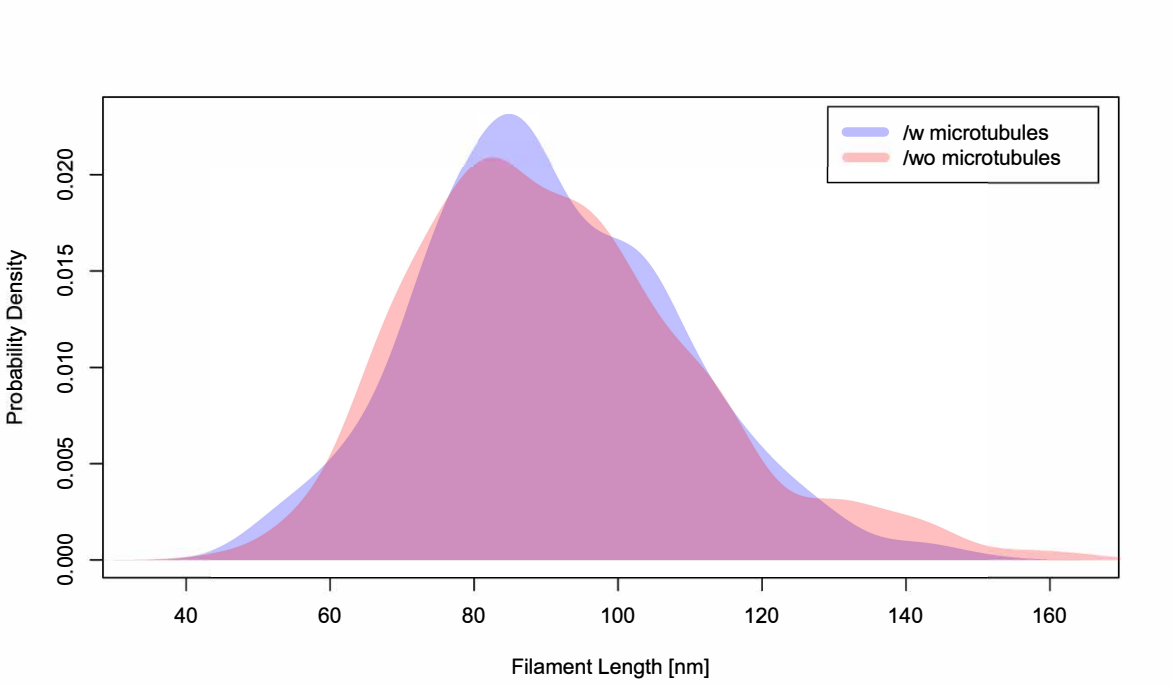


**Figure 43: LINC complex length distribution.** Density curves of LINC complex lengths of tomograms with and without microtubules. Figure adopted from [72].

Another key metric to describe the morphology of a protein is its width. In this work, an overall width of the LINC complexes at telomere attachment sites was determined to be 2 nm (filaments of attachments with microtubule: 1.9 ± 0.3 nm; filaments of attachments without microtubule: 1.9 ± 0.2 nm). To reflect the width of the LINC complexes accurately, the width of each LINC complex was determined at four designated positions. These four measurements were then averaged to calculate an average width of a single LINC complex along its length. The resulting values of the individual LINC complexes were then averaged to determine the overall width of 2 nm for LINC complexes at meiotic telomere attachment sites.

### 5.2.2 LINC complex distribution at meiotic telomere attachment sites

LINC complexes are mechanotransductors that convey the forces generated by cytoplasmic motors to move the meiotic telomeres into the nucleus. Based on their function, they can be classified as load-bearing proteins. As such they are required to provide both tensile mechanical strength to uphold the connection between the telomeres and the cytoplasmic motors, while simultaneously exhibiting enough elasticity to allow for smooth telomere movements. Other load-bearing proteins with similar requirements are e.g. collagen and elastin in bone and tendon as well as actin involved in muscle contraction. A common feature that these proteins share are supercoiled protein motifs such as the collagen triple helix or an alpha helical coiled-coil in case of actin and the LINC complex. Moreover, load-bearing proteins typically show a hierarchical organization as nanocomponents in multiprotein assemblies on the ultrastructural level. To test the hypothesis that the LINC complexes at meiotic telomere attachment sites also follow a specific pattern that facilitates their function, their distribution was analyzed based on the 3D models of the attachment sites in this work.

In a first step, the distribution of the LINC complex origins at the inner nuclear membrane was analyzed. The command line application model2point of the IMOD software suite was used to extract the point coordinates of the individual filaments. The origins of each of the LINC complexes were assigned as the point where they intersect with the inner nuclear membrane. Assuming that the LINC complex origins cluster in subgroups at the inner nuclear envelope following a specific pattern, a cluster analysis using k-means [203] was performed. This analysis did not indicate the existence of any significant clusters (data not shown).

In the absence of filament origin clusters, a regular spacing of the LINC complex origins at the inner nuclear membrane is an intuitive organizational model alternative. Thus, in the next step, the minimum Euclidean distance between the individual filament origins was calculated and plotted as a histogram (Figure 44). A regular spacing of the filament origins would be reflected in a narrow normal distribution indicating a common distance between the filament origins. The curve however resembles an exponential distribution, which means that there is no common distance between neighboring filaments (Figure 44). Interestingly though, the exponential function is

shifted to the right by 5 nm from the origin of the x-axis, which suggests a global minimum distance between neighboring filament origins of 5 nm (Figure 44). There was no significant difference in data behavior between filaments at attachments with a microtubule to those without.

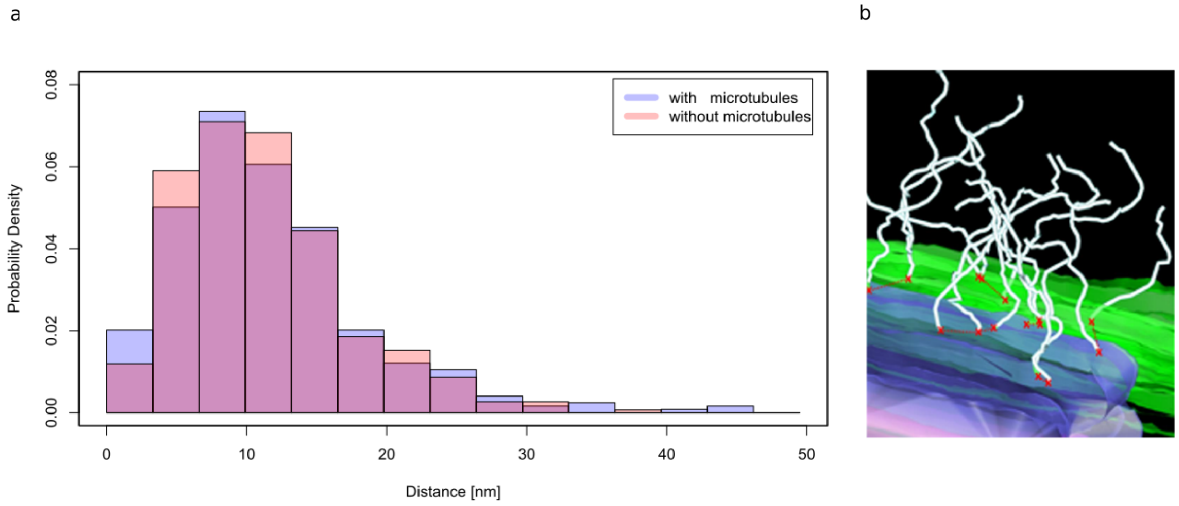


**Figure 44: Histograms of the distribution of LINC complex origin distances at the nuclear envelope of meiotic telomere attachment sites.** a. Minimum distance between neighboring LINC complex origins. The curve resembles an exponential distribution which indicates that there is no common distance between the LINC complex origins. The exponential function is however shifted to the right by 5 nm which highlights a minimum distance between the LINC complex origins of 5 nm. b. Magnified view of the 3D model of a telomere attachment site. The red crosses reflect the LINC complex origins while the red dashed lines reflect the minimum distances between neighboring LINC complex origins. Inner nuclear membrane (green), attachment plate (purple), LINC complexes (light cyan). Figure adapted from [72].

Since the LINC complexes are rippled structures, the distance between neighboring filaments differs along their course. Therefore, as mentioned earlier, the organization of LINC complexes into higher-order complexes has been proposed. The three KASH domain peptides that form a single LINC complex through interaction with a SUN trimer hereby do not interact with each other since they are separated by roughly 50 angstrom. A potential multimerization would instead manifest between KASH peptides of neighboring filaments. A common distance between neighboring LINC complexes could hint at a higher-order organization of the LINC complexes. Therefore, the minimum Euclidean distances between all point coordinates of the respective neighboring filaments were calculated and plotted as a histogram (Figure 45). The corresponding probability density curve progresses exponentially, indicating there is no common minimum distance between neighboring LINC complexes. The curve is however shifted right by 2 nm from the x-axis origin. This global minimum indicates that neighboring

filaments do not get closer to each other than 2 nm (Figure 45).

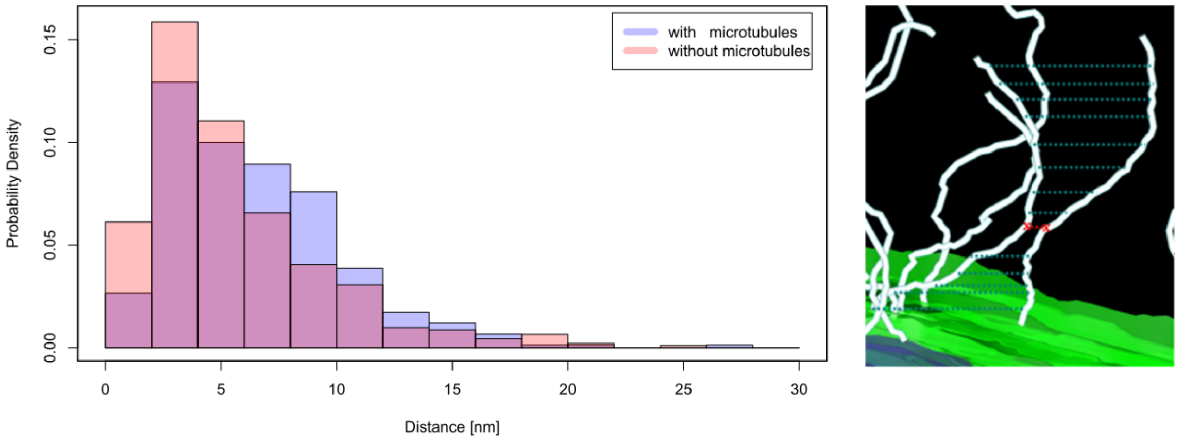


**Figure 45: Histograms of the distribution of distances between neighboring LINC complexes at meiotic telomere attachment sites.** a. Minimum interfilamentous distance between neighboring LINC complexes. The curve resembles an exponential distribution which indicates that there is no common distance between the neighboring LINC complexes. The exponential function is however shifted to the right by 2 nm which highlights a minimum distance between neighboring LINC complexes of 2 nm. b. Magnified view of the 3D model of a telomere attachment site. The respective distances are indicated by red crosses and blue dashed lines. Inner nuclear membrane (green), attachment plate (purple), LINC complexes (light cyan). Figure adapted from [72].

Interestingly, the average minimum distance between neighboring LINC complexes is significantly larger for LINC complexes at attachment sites with a microtubule closeby (two-sample Kolmogorov–Smirnov test for equality, $p = 2.66 \cdot 10^{-5}$). The larger interfilamentous distance could be explained by a lesser degree of curvature of these filaments. The stretch factor of a filament is defined as the linear distance between its end points divided by the overall length of the filament. In the present work it was determined that the stretch factor is indeed larger for LINC complexes at telomere attachment sites with a microtubule which means that these LINC complexes are less rippled compared to those at telomere attachment sites without a microtubule closeby (Figure 46a). The average linear distance between the end points of the LINC complexes is accordingly 3.5% greater for filaments at attachment sites with a microtubules (LINC conplexes close to a microtubule: 72.6 nm; LINC complexes at attachment sites without a microtubule: 70.1 nm) (Figure 46a).

A visual analysis of the population of LINC complexes at attachment sites with a microtubule revealed that a subset of the LINC complexes at these sites are particularly close to the microtubule, while others are further away from the microtubule. Assum-

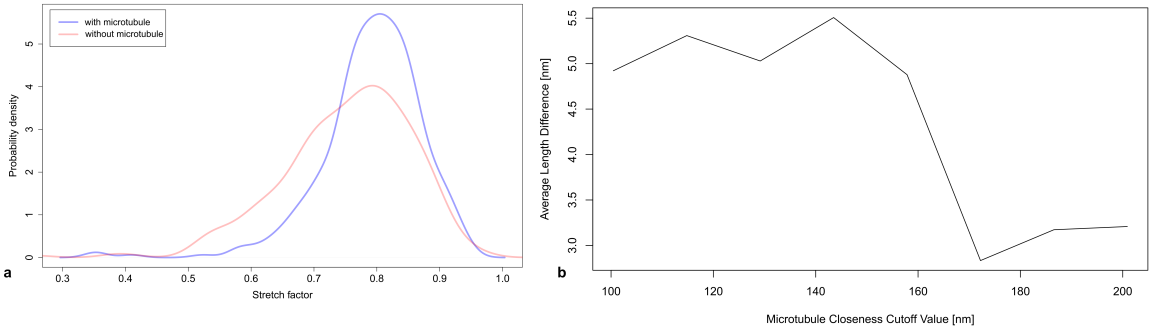


**Figure 46: Impact of microtubules on the rippledness of LINC complexes at telomere attachment sites.** a. Density plot of the stretch factor (linear distance/length) of LINC complexes at attachment sites close to a microtubule and at attachment sites without a microtubule. b. Average linear distance of LINC complexes close to a microtubule compared to LINC complexes far from the microtuble for varying cutoff values. LINC complexes within 160 nm of the microtubule are less rippled and therefore stretch further from the nuclear envelope. Figure adapted from [72].

ing that the less rippled state of LINC complexes close to a microtubule is linked to the direct interaction between the LINC complexes and the microtubule motor system, the filaments with a particularly close relation to the microtubule should be less rippled than ones that are further away. At a certain distance between the LINC complex and the microtubule motor system, the curvature of the filament might not even be affected by the presence of the microtubule motor system. To address this hypothesis, the filaments at attachment sites with a microtubule were divided into two groups: filaments close to the microtuble and filaments far from the microtubule according to varying cutoff values. The linear distance between the filament end points was plotted in relation to these cutoff values (Figure 46b). LINC complexes that are less than 100 nm away from the microtubule are significantly longer (roughly 4 nm; Wilcoxon rank-sum test) than filaments above this cutoff value. This difference in length persists up to 158 nm before it decreases gradually. Consequently, LINC complexes within 160 nm of the microtubule are less rippled and therefore stretch further from the nuclear envelope (NE) (Figure 46).

In EM micrographs, LINC complexes appear to originate from the attachment plates, pass through both nuclear membranes and emanate into the cytoplasm. Telomere repeat sequences have been localized to the electron-dense attachment plates by EM in situ hybridization assays. The telomeres are protected by a meiotic shelterin complex consisting of TERB1/2 and MAJIN. TERB1 connects the shelterin complex to SUN1.

The meiotic shelterin complex is further anchored within the inner nuclear membrane via a putative transmembrane subunit of MAJIN. Due to the tight association between the telomeric DNA and the shelterin complex, TERB1/2 and MAJIN might localize to the attachment plate as well. However, little to nothing is known yet about the proteinaceous or membranous components that make up the attachment plates.

In this work, the area of the inner nuclear membrane in which the LINC complexes concentrate has been determined using principal component analysis. Therefore, a plane that is parallel to the nuclear envelope was fitted to each of the two groups of LINC complex origins associated with the attachment plates. The origins of the LINC complexes were projected onto this plane and the smallest area that contains all LINC complex origins was determined. The longer side of this (rectangular) area which runs parallel to the nuclear envelope is approximately 150 nm long. This length can be equated to the length on a microtubule that LINC complexes interact with. Knowing the size of the dynein-dynactin complex and the force one of the motor complexes generates, the active force at a telomere attachment site can be estimated. In 2015, Chowdhury et al. resolved the dimensions of the isolated dynein-dynactin-microtubule-complex with cryo-EM. The complex extends 17 nm by 43 nm by 33 nm [204]. Taking the longest side into account, a maximum of about 6-8 complexes could accommodate a single meiotic telomere attachment site. A single dynein-dynactin complex exerts a force of roughly 5 pN [205]. Consequently, the force necessary to move a single telomere attachment site would add up to $\sim$40 pN.

The stability of a dynein-dynactin complex is mediated through the binding of a dynein cargo adaptor protein to the complex. The adaptor protein further regulates the in vivo processivity rate of the dynein-dynactin complex (DD complex) [202]. Depending on the cargo or function, different adaptors stabilize the complex. In a recent cryo-EM study of microtubule-bound DD-BICD2N (DDB) complexes (isolated from murine brain tissue), two dynein dimers were resolved in a complex [202]. The N-terminus of BICD2 (BICD2N) had been shown to be sufficient for DDB processivity while facilitating the binding of the adaptor protein to the complex compared to the full length version [206, 207]. Previous motility assays and structural studies had however led to the conclusion that BICD2 forms only a tripartite complex with dynein and dy-

nactin [208, 207, 209, 210]. Another recent cryo-EM study showed that BICD2 can recruit either one or two dyneins to the complex depending on the position of the adaptor within the complex [211]. In mammals, BICD2 facilitates vesicle transport and has a role in positioning the nucleus. For the latter, the nucleoporin RanBP2 directs BICD2 to the nuclear envelope (NE). BICD2 is the only membrane associated adaptor protein, which puts it at the focus when studying its relation to other membrane associated proteins such as the LINC complexes in this work [206]. The relation of BIC2D to the LINC complex component KASH5 at meiotic telomere attachment sites has been investigated intensively in the PhD thesis of Anna Salter of the University of Manchester ("Investigating the interaction between the nuclear envelope protein KASH5 and dynein", 2016) [212]. When she used KASH5 as bait in co-immunoprecipitations, it did not pull down. Vice versa, BICD2 did not co-immunoprecipitate KASH5. It was further shown, that both KASH5 and BICD2 bind to the same region on the light intermediate chain 1/2 (LIC 1/2) of dynein [212]. A common domain that mediates the interaction between the LICs of dynein and KASH5 or BICD2 was however not identified. Overall, these findings suggest that KASH5 and BICD2 compete for the binding to dynein and infer the role of KASH5 as a dynein adaptor protein [212]. Under the assumption that KASH5 truly acts as a dynein adaptor, it still remains elusive how many dynein complexes are recruited to the dynein-dynactin-KASH5 complex at murine meiotic telomere attachment sites. Since the recruitment of two dyneins to these sites cannot be excluded, it is also possible that a maximum of 80 pN would be required to move a single telomere attachment site in mouse meiocytes.

## 5.3 Discussion

Recombination between the homologous chromosomes is at the heart of prophase I. In preparation for recombination, pairing and synapsis of the homologs is required [51]. In the premeiotic nucleus, the homologous chromosomes are far from each other. In order for the homologs to pair and synapse, they have to get close. At the onset of prophase I, the telomeres of the homologs therefore attach to the nuclear envelope via the meiosis specific shelterin complex [66]. The attached yet dispersed telomeres then start to move across the plane of the inner nuclear envelope for the homologs to find each other, so that they can pair and synapse. Even after pairing and synapsis have occurred, the telomere-led movements persist until the end of prophase I [32]. They are essential to

meiosis, as mutations that affect the force generating machinery behind the movements lead to a pre-meiotic arrest [32]. The present work contributes to the understanding of the meiotic telomere-led movement by providing quantitative and topological data on this force generating machinery, predominantly the mechanotransduction component that is the LINC complex.

As mentioned earlier, the force that is required for the telomere-led chromosome movements in prophase I is predominantly generated by the microtubule-dependent dynein-dynactin complex. The outer nuclear membrane protein KASH5 of the meiotic LINC complex connects the motor complex via the inner nuclear LINC complex component SUN1/2 to the meiotic shelterin complex (TERB1/2-MAJIN) that caps the telomeres [32, 194, 46, 85, 66]. The dynein-dynactin (DD) motor complex is highly dynamic which makes it challenging to visualize, especially in the crowded cytoplasm [201]. In the frame of this work, dynein and dynactin visualization at telomere attachment sites was attempted using immunoelectron microscopy. Neither of the proteins could be localized successfully using this approach. Their tight association and dynamic nature *in situ* demand for existing approaches to be refined accordingly or the development of novel imaging technologies as suggested in a recent review [201].

In EM micrographs of murine telomere attachment sites, assemblies of filaments have been repeatedly observed that seemingly originate from the attachment plates, breach the nuclear envelope and emanate into the cytoplasm. Based on their location, these filaments have been presumed to be LINC complexes. To test this hypothesis, SUN1 and SUN2 have been localized on frozen tissue sections of murine testes tissue in the past. In these experiments, SUN1/2 were detected at the perinuclear part of the filament assembly [70, 71]. The localization of SUN1 was reproduced in the frame of the present work. However, the cytoplasmic part of the filament assemblies had so far not been probed to be KASH5. To fill this gap, an antibody against the N-terminus of KASH5 was designed in the present work and used for immuno-EM localizations on murine frozen testes sections accordingly. Here, KASH5-N localized to the ends of the filament assemblies at telomere attachment sites. Consequently, both components of the LINC components have been localized to the assembly of filaments that seemingly originate from the attachment plates of the meiotic telomeres.

SUN1 and KASH5 were further localized using structured illumination microscopy (SIM) and Ex-SIM (MAP expansion protocol). In triple localizations, the LINC complex proteins were visualized at the ends of the signal of the lateral element protein SYCP3. In the SIM acquisitions, SUN1 and KASH5 predominantly colocalized in all prophase stages. At the higher resolution provided by Ex-SIM, an initial acquisition of a pachytene spermatocyte showed that the proteins could be resolved separately with SUN1 residing between the ends of the SYCP3 signal and KASH5. Indifferent of the microscopic application, both LINC complex proteins were resolved as pairs of clearly separated foci, each of which associated with a single strand of SYCP3. A previously described ring-shaped signal [85] of SUN1 or KASH5 was not observed here. The cause for the ring-like appearance could be attributed to antigen masking or comprised antigen accessibility at the center of the LINC complex assemblies.

In order to collect quantitative and topological data of the meiotic LINC complexes, electron microscope tomograms of murine telomere attachment sites were acquired. Post-acquisition, tomograms were initially visually inspected. Interestingly, only roughly 50% of the tomograms showed telomere attachment sites with a microtubule. This was surprising since nearly 100% of SUN1 and tubulin foci co-localized in confocal images of pachytene spermatocytes as shown by Lee et al. in 2015 [32], which implies that every attachment site should be associated with microtubules. As a diffraction limited technique, the lateral resolution of confocal microscopy is however limited in locating tubulin precisely to the LINC complexes at a telomere attachment site. Since pachynema is one of the prophase stages that is characterized by slower telomere-led movements, the attachment sites without a microtubule acquired with nanometer precision by electron microscope tomography in the present work, were likely stationary, while the attachments with a microtubule were motile at the time of fixation for ET. This explanation fits nicely with the observation that telomeres are not consistently moving but rest in between movements as observed in live-cell and confocal acquisitions of murine prophase nuclei [213, 32, 51]. The microtubules in the tomograms were oriented predominantly longitudinal to the attachments. Initially, the tomograms with and without a microtubule were analyzed separately to detect potential differences between motile and steady attachments. There were however no significant differences

between the two data sets based on the analyzed parameters. Interestingly, indifferent of the presence of a microtubule, the same number of LINC complexes populate an attachment site. Thus, LINC complexes are constitutive components of the telomere attachment sites in mouse meiocytes.

For the quantitative and topological analysis of the LINC complexes, the tomograms were segmented manually for the nuclear envelope and the LINC complexes, as well as the attachment plates and components of the synaptonemal complex at the telomere attachment sites. These supervised segmentations resulted in the generation of the first 3D model of telomere attachment sites based on actual morphological data. The 3D models revealed that on average almost 80 LINC complexes are divided into two patches based on allocation to either of the two attachment plates with a length of approximately 90 nm and a diameter in the scale of a few nanometers reside at the meiotic attachment sites in mouse. For the 40 telomere pairs of a diploid murine spermatocyte, this would add up to roughly 3000 LINC complexes. Translated to the number of SUN1/2 and KASH5 molecules, this scales to the range of 10,000 molecules for the trimeric proteins [75] per meiotic nucleus.

Aside from the stoichiometric analysis of the LINC complex, the 3D model of the telomere attachment sites further allowed for a topological analysis of the complexes at these sites. An initial cluster analysis did not reveal the local concentration of LINC complexes within the two patches of LINC complexes associated with the attachment plates. In the absence of clusters, an even spacing of the proteins at a mean distance lends itself as an attractive model for the organization of the complexes. While there was no common distance quantifiable and the data supports a rather random organization, a global minimum distance between neighboring filaments was revealed. At the LINC complex origins on the plane of the inner nuclear membrane, this distance is 5 nm, along the entire course of the filaments, LINC complexes can get as close as 2 nm to each other. Surprisingly, at attachment sites with a microtubule, the average distance between neighboring LINC complexes was larger. This observation led to the hypothesis that the association with the microtubule motor system might cause the LINC complexes to stretch further from the nuclear envelope, or in other words be less rippled. A larger stretch factor of the LINC complexes at telomere attachment sites

with a microtubule supported this hypothesis. LINC complexes at telomere attachment sites with a microtubule are further significantly longer when they are within 160 nm of the microtubules compared to filaments that are further away from the microtubule at these sites. The latter of which do not differ in length compared to LINC complexes at telomere attachment sites without a microtubule. Thus the microtubule-dependent motor system likely influences the rippledness of the meiotic LINC complexes.

The 3D ET derived model of telomere attachment sites generated in the frame of the present work finally allowed for a first estimation of the maximum force that would be required to actively move the telomeres of said attachment. Using principle component analysis, the area in which the LINC complexes that are associated with one of the attachment plates concentrate was determined. The longer side of this area, that is roughly parallel to the nuclear envelope is approximately 150 nm long. Assuming that this is equal to the length on a microtubules with which the LINC complexes interact and knowing the dimensions [204] and force [205] generated by a single dynein-dynactin (DD) complex, the upper limit of the active force at a telomere attachment site could be determined. Depending on whether one or two dyneins [202] are forming the DD complex at the murine attachment sites, $\sim$40 or $\sim$80 pN would be sufficient to move the telomeres of a single pair of homologs.

# 6 General discussion and outlook

This thesis investigates the molecular architecture of two essential meiotic multiprotein complexes, the synaptonemal complex (SC) and the LINC complex. The functions of both complexes are tightly linked to their structure. Consequently, in order to truly understand the functions of the SC and the LINC complex, their respective structure has to be investigated. Key metrics that define the structure of a multiprotein complex such as the stoichiometry of its components and their topology within the complex were unknown both for complexes. The present work lays the foundation for future investigation of the structure-function relationship of the SC and the meiotic LINC complex by providing these missing quantitative and topological data based on 3D electron microscope tomographic (ET) models complemented by super-resolution light microscopic data.

Based on the 3D model of the LINC complexes, the present work further determines the first estimation of an upper limit of forces required to move a telomere attachment site in the murine meiotic nucleus. The estimated 40 pN to 80 pN provide the order of magnitude of molecular forces to be considered in future research. An interesting route to increase our understanding of the mechanisms behind the mechanotransduction at telomere attachment sites could be to study force transduction in artificial membranes. Artificial nuclear membranes (ANMs) have been recently established as a synthetic bottom-up system to study the LINC complex assembly [214]. In the future, this system could be combined with a microtubule gliding assay to study the kinetics of the LINC complex mediated movement. The controlled manipulation of this artificial system could further our understanding of the mechanisms behind force transduction via LINC complexes. Moreover, artificial nuclear membranes would also open up the study of meiotic LINC complexes to single-molecule force spectroscopy techniques such as atomic force microscopy (AFM), and optical or magnetic tweezers for force-related studies and mechanistic insight. Another advantage of artificial membranes is their ability to be gradually increased in complexity. This allows the controlled introduction of additional components that have been shown or are suspected to influence the mechanotransduction process, e.g., the meiotic lamina [214]. Artificial nuclear membranes may even be expanded towards entire synthetic nuclear envelopes by fusing a

supported lipid bilayer with a vesicle that differs in composition to recreate the varying nature of the inner and outer nuclear membrane [214].

According to the 3D model derived in this work, the distribution of the LINC complexes at telomere attachment sites does not follow a distinct organizational pattern. The model also revealed a minimum distance between the LINC complexes. At their origin, this minimum distance might be predetermined by the underlying organization of the telomere binding proteins. SUN1/2 are recruited to the murine telomere attachment sites through the interaction of the telomere binding protein TERB1 and the shelterin component TRF1 [215]. Therefore, the distribution of the chimeric telomere binding complex could define the minimum distance of the LINC complexes at the inner nuclear envelope. To test this hypothesis, the organization of the telomere binding proteins would have to be investigated at nanoscale resolution. The detection of telomere repeat sequences at murine telomere attachment plates in electron micrographs [65] suggests that the telomere binding proteins likely also localize to these sites. Light microscopic approaches have shown the co-localization of the telomere binding proteins at the ends of the SYCP3 signal which is topologically roughly equivalent to the former telomere attachment sites [66, 216]. The lateral resolution provided by single-molecule localization microscopy approaches has the potential to resolve the hierarchy of the telomere binding complexes. The foreseeable development of imaging platforms and sophisticated imaging approaches towards even higher resolution could eventually be used to determine stoichiometry and distribution of the telomere binding proteins and the influence of their topology on the organization of the LINC complexes.

Like the LINC complexes, the transverse filaments of the synaptonemal complex also show a scattered organization as revealed in the present work. The 3D ET derived model of the SC reflects their asymmetric distribution in a monolayer, contrary to the previously assumed bilayered organization. Over the course of prophase I, the synaptonemal complex is required to change dynamically, e.g., in response to inversion loops or deletions [217]. Beyond assembly and disassembly, components of the SC are thus incorporated and disassociated from the complex in a dynamic state as observed in budding yeast [117]. With the progression of prophase I the number of proteins that are incorporated into the SC exceeds the number of proteins leaving the

complex [117]. Consequently, the dynamic structure needs to meet the requirements of telomere movements throughout prophase I by being flexible yet resistant. The less orderly, asymmetric organization of the SC uncovered in the present work, supports the dynamic, robust, yet flexible properties of the SC.

The macromolecular complexes that mediate meiotic telomere attachment and movement on the one hand and the synapsis and recombination of homologous chromosomes on the other hand are interdependent as they drive meiotic progression in a timely, inseparable manner. Both the LINC complexes and the transverse filaments of the SC are subjected to the forces that are required for the telomere-led movements throughout prophase I. Similar to other load-bearing proteins, the rippled filaments largely consist of coiled-coil domains. The reaction of filamentous proteins to mechanical strain is commonly explained with the worm-like chain (WLC) model of polymer elasticity [218, 219, 220], which models the proteins as elastic, irregularly curved, semi-flexible rods. Applying the WLC model to the meiotic filamentous proteins could describe their behavior and allow the calculation of many force related properties, such as the force required to stretch the polypeptide chain in the future.

In the present work, the analysis of the meiosis-specific multiprotein complexes is limited to pachynema. An interesting avenue for future investigations would be to model and analyze their properties in the other stages of prophase I to monitor their behavior in relation to the processes that characterize meiotic progression. Striving towards a holistic understanding of meiotic prophase mechanisms, the structure of other large meiotic multiprotein complexes, such as the cohesin complexes or the recombination machinery, has to be investigated and integrated into the current understanding of prophase processes. Furthermore, the influence of other biomolecules on these processes, above all the chromatin of the homologous chromosomes, should be considered. There are still many interesting details left to uncover about the complex and intriguing interaction between the biomolecules that drive haploidization and recombination at the heart of meiosis. In this regard, the present work provides the quantitative and topological basis to build upon in future studies.

# List of Figures

# List of Tables

# References


[1] Oscar Hertwig. *Beitraege zur Kenntniss der Bildung, Befruchtung und Theilung des thierischen eies*, volume 1. W. Engelmann, 1875.

[2] Edouard Van Beneden. *Recherches sur la maturation de l'oeuf, la fécondation, et la division cellulaire*. Librairie Clemm, 1883.

[3] G Hamoir. The discovery of meiosis by e. van beneden, a breakthrough in the morphological phase of heredity. *Int J Dev Biol.*, 36:9–15, 1992.

[4] August Weismann. Prof. weismann's theory of heredity. *Nature*, 41(1058):317–323, 1890.

[5] Walter S Sutton. On the morphology of the chromoso group in brachystola magna. *The Biological Bulletin*, 4(1):24–39, 1902.

[6] Walter S Sutton. The chromosomes in heredity. *The Biological Bulletin*, 4(5):231–250, 1903.

[7] Theodor Boveri. *Ergebnisse über die Konstitution der chromatischen Substanz des Zellkerns*. G. Fischer, 1904.

[8] J Bretland Farmer and JES Moore. Memoirs: On the maiotic phase (reduction divisions) in animals and plants. *Journal of Cell Science*, 2(192):489–558, 1905.

[9] Emilio Battaglia. Meiosis and mitosis: a terminological criticism. *Annali di Botanica*, 43:101–140, 1985.

[10] Thomas Hunt Morgan. The origin of nine wing mutations in drosophila. *Science*, 33(848):496–499, 1911.

[11] Harriet B Creighton and Barbara McClintock. A correlation of cytological and genetical crossing-over in zea mays. *Proceedings of the National Academy of Sciences of the United States of America*, 17(8):492, 1931.

[12] Richard Egel and David Penny. On the origin of meiosis in eukaryotic evolution: coevolution of meiosis and mitosis from feeble beginnings. In *Recombination and meiosis*, pages 249–288. Springer, 2007.

[13] Marilee A Ramesh, Shehre-Banoo Malik, and John M Logsdon Jr. A phylogenomic inventory of meiotic genes: evidence for sex in giardia and an early eukaryotic origin of meiosis. *Current biology*, 15(2):185–191, 2005.

[14] Dave Speijer, Julius Lukeš, and Marek Eliáš. Sex is a ubiquitous, ancient, and inherent attribute of eukaryotic life. *Proceedings of the National Academy of Sciences*, 112(29):8827–8834, 2015.

[15] Ashok Agarwal, Aditi Mulgund, Alaa Hamada, and Michelle Renee Chyatte. A unique

view on male infertility around the globe. *Reproductive biology and endocrinology*, 13(1):37, 2015.

[16] E Leifke and E Nieschlag. Male infertility treatment in the light of evidence-based medicine. *Andrologia*, 28:23–30, 1996.

[17] Martin M Matzuk and Dolores J Lamb. The biology of infertility: research advances and clinical challenges. *Nature medicine*, 14(11):1197, 2008.

[18] Katherine LO'Flynn O'Brien, Alex C Varghese, and Ashok Agarwal. The genetic causes of male factor infertility: a review. *Fertility and sterility*, 93(1):1–12, 2010.

[19] Renee Reijo, Tien-Yi Lee, Pia Salo, Raaji Alagappan, Laura G Brown, Michael Rosenberg, Steve Rozen, Tom Jaffe, Donald Straus, Outi Hovatta, et al. Diverse spermatogenic defects in humans caused by y chromosome deletions encompassing a novel rna–binding protein gene. *Nature genetics*, 10(4):383–393, 1995.

[20] Randy S Morris and Norbert Gleicher. Genetic abnormalities, male infertility, and icsi. *Lancet*, 347(9011):1277, 1996.

[21] BFJ Thielemans, Carl Spiessens, Thomas D'Hooghe, Dirk Vanderschueren, and Eric Legius. Genetic abnormalities and male infertility. a comprehensive review. *European Journal of Obstetrics & Gynecology and Reproductive Biology*, 81(2):217–225, 1998.

[22] Arzu Vicdan, Kubilay Vicdan, Serdar Günalp, Aykut Kence, Cem Akarsu, Ahmet Zeki Işık, and Eran Sözen. Genetic aspects of human male infertility: the frequency of chromosomal abnormalities and y chromosome microdeletions in severe male factor infertility. *European Journal of Obstetrics & Gynecology and Reproductive Biology*, 117(1):49–54, 2004.

[23] Maria Rosa Maduro and Dolores J Lamb. Understanding new genetics of male infertility. *The Journal of urology*, 168(5):2197–2205, 2002.

[24] Robert I McLachlan and Moira K O'Bryan. State of the art for genetic testing of infertile men. *The Journal of Clinical Endocrinology & Metabolism*, 95(3):1013–1024, 2010.

[25] Michael C Hann, Patricio E Lau, and Helen G Tempest. Meiotic recombination and male infertility: from basic science to clinical reality? *Asian journal of andrology*, 13(2):212, 2011.

[26] Duangporn Jamsai and Moira K O'bryan. Mouse models in male fertility research. *Asian journal of andrology*, 13(1):139, 2011.

[27] Stephan Gruber, Christian H Haering, and Kim Nasmyth. Chromosomal cohesin forms a ring. *Cell*, 112(6):765–777, 2003.

[28] Maureen Eijpe, Hildo Offenberg, Rolf Jessberger, Ekaterina Revenkova, and Christa

Heyting. Meiotic cohesin rec8 marks the axial elements of rat synaptonemal complexes before cohesins smc1$\beta$ and smc3. *The Journal of cell biology*, 160(5):657–670, 2003.

[29] EMECHBG Revenkova, M Eijpe, C Heyting, B Gross, and R Jessberger. Novel meiosis-specific isoform of mammalian smc1. *Molecular and cellular biology*, 21(20):6984–6998, 2001.

[30] Josef Loidl. The initiation of meiotic chromosome pairing: the cytological view. *Genome*, 33(6):759–778, 1990.

[31] D Zickler and N Kleckner. The leptotene-zygotene transition of meiosis. *Annual review of genetics*, 32(1):619–697, 1998.

[32] Chih-Ying Lee, Henning F Horn, Colin L Stewart, Brian Burke, Ewelina Bolcun-Filas, John C Schimenti, Michael E Dresser, and Roberto J Pezza. Mechanism and regulation of rapid telomere prophase movements in mouse meiotic chromosomes. *Cell reports*, 11(4):551–563, 2015.

[33] Neil Hunter. Meiotic recombination: the essence of heredity. *Cold Spring Harbor perspectives in biology*, 7(12):a016618, 2015.

[34] Martin P Kracklauer, Jana Link, and Manfred Alsheimer. Lincing the nuclear envelope to gametogenesis. In *Current topics in developmental biology*, volume 102, pages 127–157. Elsevier, 2013.

[35] Martti Parvinen and Karl-Ove Söderström. Chromosome rotation and formation of synapsis. *Nature*, 260(5551):534–535, 1976.

[36] Yuji Chikashige, Da-Qiao Ding, Hironori Funabiki, Tokuko Haraguchi, Shinro Mashiko, Mitsuhiro Yanagida, and Yasushi Hiraoka. Telomere-led premeiotic chromosome movement in fission yeast. *Science*, 264(5156):270–273, 1994.

[37] Michael N Conrad, Chih-Ying Lee, Gene Chao, M Shinohara, H Kosaka, A Shinohara, J-A Conchello, and Michael E Dresser. Rapid telomere movement in meiotic prophase is promoted by ndj1, mps3, and csm4 and is modulated by recombination. *Cell*, 133(7):1175–1187, 2008.

[38] Da-Qiao Ding, Yuji Chikashige, Tokuko Haraguchi, and Yasushi Hiraoka. Oscillatory nuclear movement in fission yeast meiotic prophase is driven by astral microtubules, as revealed by continuous observation of chromosomes and microtubules in living cells. *Journal of cell science*, 111(6):701–712, 1998.

[39] R Koszul, KP Kim, M Prentiss, N Kleckner, and S Kameoka. Meiotic chromosomes move by linkage to dynamic actin cables with transduction of force through the nuclear envelope. *Cell*, 133(7):1188–1201, 2008.

[40] Leticia Labrador, Consuelo Barroso, James Lightfoot, Thomas Müller-Reichert,

Stephane Flibotte, Jon Taylor, Donald G Moerman, Anne M Villeneuve, and Enrique Martinez-Perez. Chromosome movements promoted by the mitochondrial protein spd-3 are required for homology search during caenorhabditis elegans meiosis. *PLoS genetics*, 9(5), 2013.

[41] Geoffrey K Rickards. Prophase chromosome movements in living house cricket spermatocytes and their relationship to prometaphase, anaphase and granule movements. *Chromosoma*, 49(4):407–455, 1975.

[42] Harry Scherthan, Hailin Wang, Caroline Adelfalk, Eric J White, Carrie Cowan, W Zacheus Cande, and David B Kaback. Chromosome mobility during meiotic prophase in saccharomyces cerevisiae. *Proceedings of the National Academy of Sciences*, 104(43):16934–16939, 2007.

[43] Moira J Sheehan and Wojciech P Pawlowski. Live imaging of rapid chromosome movements in meiotic prophase i in maize. *Proceedings of the National Academy of Sciences*, 106(49):20989–20994, 2009.

[44] David J Wynne, Ofer Rog, Peter M Carlton, and Abby F Dernburg. Dynein-dependent processive chromosome motions promote homologous pairing in c. elegans meiosis. *Journal of Cell Biology*, 196(1):47–64, 2012.

[45] Meisha A Morelli, Uwe Werling, Winfried Edelmann, Mark S Roberson, and Paula E Cohen. Analysis of meiotic prophase i in live mouse spermatocytes. *Chromosome research*, 16(5):743–760, 2008.

[46] Akihiro Morimoto, Hiroki Shibuya, Xiaoqiang Zhu, Jihye Kim, Kei-ichiro Ishiguro, Min Han, and Yoshinori Watanabe. A conserved kash domain protein associates with telomeres, sun1, and dynactin during mammalian meiosismammalian meiotic kash domain protein kash5. *The Journal of cell biology*, 198(2):165–172, 2012.

[47] Hiroki Shibuya, Akihiro Morimoto, and Yoshinori Watanabe. The dissection of meiotic chromosome movement in mice using an in vivo electroporation technique. *PLoS genetics*, 10(12), 2014.

[48] Hiroki Shibuya, Kei-ichiro Ishiguro, and Yoshinori Watanabe. The trf1-binding protein terb1 promotes chromosome movement and telomere rigidity in meiosis. *Nature cell biology*, 16(2):145–156, 2014.

[49] KTS Yao and DJ Ellingson. Observations on nuclear rotation and oscillation in chinese hamster germinal cells in vitro. *Experimental cell research*, 55(1):39–42, 1969.

[50] Josef Loidl. Conservation and variability of meiosis across the eukaryotes. *Annual review of genetics*, 50:293–316, 2016.

[51] Benjamin Alleva and Sarit Smolikove. Moving and stopping: Regulation of chromosome

movement to promote meiotic chromosome pairing and synapsis. *Nucleus*, 8(6):613–624, 2017.

[52] Jun Liu, Tom Rolef Ben-Shahar, Dieter Riemer, Millet Treinin, Perah Spann, Klaus Weber, Andrew Fire, and Yosef Gruenbaum. Essential roles for caenorhabditis elegans lamin gene in nuclear organization, cell cycle progression, and spatial organization of nuclear pore complexes. *Molecular biology of the cell*, 11(11):3937–3947, 2000.

[53] Kazuhiro Furukawa, Hidehito Inagaki, and Yasuo Hotta. Identification and cloning of an mrna coding for a germ cell-specific a-type lamin in mice. *Experimental cell research*, 212(2):426–430, 1994.

[54] Manfred Alsheimer and Ricardo Benavente. Change of karyoskeleton during mammalian spermatogenesis: expression pattern of nuclear lamin c2 and its regulation. *Experimental cell research*, 228(2):181–188, 1996.

[55] Jana Link, Daniel Jahn, and Manfred Alsheimer. Structural and functional adaptations of the mammalian nuclear envelope to meet the meiotic requirements. *Nucleus*, 6(2):93–101, 2015.

[56] Jana Link, Daniel Jahn, Johannes Schmitt, Eva Göb, Johannes Baar, Sagrario Ortega, Ricardo Benavente, and Manfred Alsheimer. The meiotic nuclear lamina regulates chromosome dynamics and promotes efficient homologous recombination in the mouse. *PLoS genetics*, 9(1), 2013.

[57] Daniel Jahn, Sabine Schramm, Ricardo Benavente, and Manfred Alsheimer. Dynamic properties of meiosis-specific lamin c2 and its impact on nuclear envelope integrity. *Nucleus*, 1(3):273–283, 2010.

[58] G Krohne. Lamin assembly in vivo. *Sub-cellular biochemistry*, 31:563–586, 1998.

[59] Nico Stuurman, Susanne Heins, and Ueli Aebi. Nuclear lamins: their structure, assembly, and interactions. *Journal of structural biology*, 122(1-2):42–66, 1998.

[60] Manfred Alsheimer, Elisabeth von Glasenapp, Robert Hock, and Ricardo Benavente. Architecture of the nuclear periphery of rat pachytene spermatocytes: distribution of nuclear envelope proteins in relation to synaptonemal complex attachment sites. *Molecular biology of the cell*, 10(4):1235–1245, 1999.

[61] Hiroki Shibuya and Yoshinori Watanabe. The meiosis-specific modification of mammalian telomeres. *Cell Cycle*, 13(13):2024–2028, 2014.

[62] Ewelina Bolcun-Filas and John C Schimenti. Genetics of meiosis and recombination in mice. In *International review of cell and molecular biology*, volume 298, pages 179–227. Elsevier, 2012.

[63] Montrose J Moses. Chromosomal structures in crayfish spermatocytes. *The Journal of biophysical and biochemical cytology*, 2(2):215, 1956.

[64] Montrose J Moses. Studies on nuclei using correlated cytochemical, light, and electron microscope techniques. *The Journal of Cell Biology*, 2(4):397–406, 1956.

[65] Bodo Liebe, Manfred Alsheimer, Christer Hoog, Ricardo Benavente, and Harry Scherthan. Telomere attachment, meiotic chromosome condensation, pairing, and bouquet stage duration are modified in spermatocytes lacking axial elements. *Molecular biology of the cell*, 15(2):827–837, 2004.

[66] Hiroki Shibuya, Abrahan Hernández-Hernández, Akihiro Morimoto, Lumi Negishi, Christer Höög, and Yoshinori Watanabe. Majin links telomeric dna to the nuclear membrane by exchanging telomere cap. *Cell*, 163(5):1252–1266, 2015.

[67] DHM Woollam and EHR Ford. The fine structure of the mammalian chromosome in meiotic prophase with special reference to the synaptinemal complex. *Journal of anatomy*, 98(Pt 2):163, 1964.

[68] P Esponda and G Gimenez-Martin. The attachment of the synaptonemal complex to the nuclear envelope. *Chromosoma*, 38(4):405–417, 1972.

[69] Preben Bach Holm and Søren Wilken Rasmussen. Human meiosis i. the human pachytene karyotype analyzed by three dimensional reconstruction of the synaptonemal complex. *Carlsberg Research Communications*, 42(4):283, 1977.

[70] Johannes Schmitt, Ricardo Benavente, Didier Hodzic, Christer Höög, Colin L Stewart, and Manfred Alsheimer. Transmembrane protein sun2 is involved in tethering mammalian meiotic telomeres to the nuclear envelope. *Proceedings of the National Academy of Sciences*, 104(18):7426–7431, 2007.

[71] Johannes Schmitt. *Proteine der Kernhülle und deren Rolle bei der Umgestaltung des Zellkerns meiotischer und postmeiotischer Zellen von Säugern.* doctoralthesis, Universität Würzburg, 2008.

[72] Marie-Christin Spindler, Josef Redolfi, Frederik Helmprobst, Philip Kollmannsberger, Christian Stigloher, and Ricardo Benavente. Electron tomography of mouse linc complexes at meiotic telomere attachment sites with and without microtubules. *Communications biology*, 2, 2019.

[73] Gregg G Gundersen and Howard J Worman. Nuclear positioning. *Cell*, 152(6):1376–1389, 2013.

[74] Melissa Crisp, Qian Liu, Kyle Roux, JB Rattner, Catherine Shanahan, Brian Burke, Phillip D Stahl, and Didier Hodzic. Coupling of the nucleus and cytoplasm: role of the linc complex. *The Journal of cell biology*, 172(1):41–53, 2006.

[75] Brian A Sosa, Andrea Rothballer, Ulrike Kutay, and Thomas U Schwartz. Linc complexes form by binding of three kash peptides to domain interfaces of trimeric sun proteins. *Cell*, 149(5):1035–1047, 2012.

[76] Wenjia Wang, Zhubing Shi, Shi Jiao, Cuicui Chen, Huizhen Wang, Guoguang Liu, Qiang Wang, Yun Zhao, Mark I Greene, and Zhaocai Zhou. Structural insights into sun-kash complexes across the nuclear envelope. *Cell research*, 22(10):1440–1452, 2012.

[77] Si Nie, Huimin Ke, Feng Gao, Jinqi Ren, Mingzhu Wang, Lin Huo, Weimin Gong, and Wei Feng. Coiled-coil domains of sun proteins as intrinsic dynamic regulators. *Structure*, 24(1):80–91, 2016.

[78] Zeinab Jahed, Darya Fadavi, Uyen T Vu, Ehsaneddin Asgari, GW Gant Luxton, and Mohammad RK Mofrad. Molecular insights into the mechanisms of sun1 oligomerization in the nuclear envelope. *Biophysical journal*, 114(5):1190–1203, 2018.

[79] Mirjam Ketema, Kevin Wilhelmsen, Ingrid Kuikman, Hans Janssen, Didier Hodzic, and Arnoud Sonnenberg. Requirements for the localization of nesprin-3 at the nuclear envelope and its interaction with plectin. *Journal of cell science*, 120(19):3384–3394, 2007.

[80] Berend Mans, Vivek Anantharaman, L Aravind, and Eugene V Koonin. Comparative genomics, evolution and origins of the nuclear envelope and nuclear pore complex. *Cell cycle*, 3(12):1625–1650, 2004.

[81] Yuji Chikashige, Chihiro Tsutsumi, Miho Yamane, Kasumi Okamasa, Tokuko Haraguchi, and Yasushi Hiraoka. Meiotic proteins bqt1 and bqt2 tether telomeres to form the bouquet arrangement of chromosomes. *Cell*, 125(1):59–69, 2006.

[82] Manickam Gurusaran and Owen R Davies. A molecular mechanism for linc complex branching by structurally diverse sun-kash 6: 6 assemblies. *BioRxiv*, 2020.

[83] Jana Link, Monika Leubner, Johannes Schmitt, Eva Göb, Ricardo Benavente, Kuan-Teh Jeang, Rener Xu, and Manfred Alsheimer. Analysis of meiosis in sun1 deficient mice reveals a distinct role of sun2 in mammalian meiotic linc complex formation and function. *PLoS genetics*, 10(2), 2014.

[84] Wakam Chang, Howard J Worman, and Gregg G Gundersen. Accessorizing and anchoring the linc complex for multifunctionality. *Journal of Cell Biology*, 208(1):11–22, 2015.

[85] Henning F Horn, Dae In Kim, Graham D Wright, Esther Sook Miin Wong, Colin L Stewart, Brian Burke, and Kyle J Roux. A mammalian kash domain protein coupling meiotic chromosomes to the cytoskeletonthe linc complex in mammalian meiosis. *The Journal of cell biology*, 202(7):1023–1039, 2013.

[86] Don W Fawcett. The fine structure of chromosomes in the meiotic prophase of vertebrate spermatocytes. *The Journal of Cell Biology*, 2(4):403–406, 1956.

[87] DITER von Wettstein, SW Rasmussen, and PB Holm. The synaptonemal complex in genetic segregation. *Annual review of genetics*, 18(1):331–411, 1984.

[88] Scott L Page and R Scott Hawley. The genetics and molecular biology of the synaptonemal complex. *Annu. Rev. Cell Dev. Biol.*, 20:525–558, 2004.

[89] Jinmin Gao and Monica P Colaiácovo. Zipping and unzipping: protein modifications regulating synaptonemal complex dynamics. *Trends in Genetics*, 34(3):232–245, 2018.

[90] Marie-Christin Spindler, Sebastian Filbeck, Christian Stigloher, and Ricardo Benavente. Quantitative basis of meiotic chromosome synapsis analyzed by electron tomography. *Scientific reports*, 9, 2019.

[91] GG Gorach, VV Safronov, OL Kolomiets, SIa Dadashev, and IuF Bogdanov. Biochemical and ultrastructural analyses of the synaptonemal complex in mammalian spermatocytes. *Tsitologiia*, 27(12):1347–1352, 1985.

[92] Tatiana M Grishaeva and Yuri F Bogdanov. Conservation and variability of synaptonemal complex proteins in phylogenesis of eukaryotes. *International journal of evolutionary biology*, 2014, 2014.

[93] Johanna Fraune, Céline Brochier-Armanet, Manfred Alsheimer, Jean-Nicolas Volff, Katharina Schücker, and Ricardo Benavente. Evolutionary history of the mammalian synaptonemal complex. *Chromosoma*, 125(3):355–360, 2016.

[94] Yu F Bogdanov, TM Grishaeva, and S Ya Dadashev. Similarity of the domain structure of proteins as a basis for the conservation of meiosis. *International review of cytology*, 257:83–142, 2007.

[95] Josef Loidl. S. pombe linear elements: the modest cousins of synaptonemal complexes. *Chromosoma*, 115(3):260, 2006.

[96] C Heyting, AJJ Dietrich, PB Moens, RJ Dettmers, HH Offenberg, EJW Redeker, and ACG Vink. Synaptonemal complex proteins. *Genome*, 31(1):81–87, 1989.

[97] RL Meuwissen, Hildo H Offenberg, AJ Dietrich, Anne Riesewijk, Martijn van Iersel, and Christa Heyting. A coiled-coil related protein specific for synapsed regions of meiotic prophase chromosomes. *The EMBO journal*, 11(13):5091–5100, 1992.

[98] Hildo H Offenberg, Johanna AC Schalk, Ralph LJ Meuwissen, Mirjam van Aalderen, Henri A Kester, Axel JJ Dietrich, and Christa Heyting. Scp2: a major protein component of the axial elements of synaptonemal complexes of the rat. *Nucleic acids research*, 26(11):2572–2579, 1998.

[99] Yael Costa, Robert Speed, Rupert Öllinger, Manfred Alsheimer, Colin A Semple,

Philippe Gautier, Klio Maratou, Ivana Novak, Christer Höög, Ricardo Benavente, et al. Two novel proteins recruited by synaptonemal complex protein 1 (sycp1) are at the centre of meiosis. *Journal of cell science*, 118(12):2755–2762, 2005.

[100] Geert Hamer, Katarina Gell, Anna Kouznetsova, Ivana Novak, Ricardo Benavente, and Christer Höög. Characterization of a novel meiosis-specific protein within the central element of the synaptonemal complex. *Journal of cell science*, 119(19):4025–4032, 2006.

[101] Sabine Schramm, Johanna Fraune, Ronald Naumann, Abrahan Hernandez-Hernandez, Christer Höög, Howard J Cooke, Manfred Alsheimer, and Ricardo Benavente. A novel mouse synaptonemal complex protein is essential for loading of central element proteins, recombination, and fertility. *PLoS genetics*, 7(5):e1002088, 2011.

[102] Laura Gómez-h, Natalia Felipe-Medina, Manuel Sánchez-Martín, Owen R Davies, Isabel Ramos, Ignacio García-Tuñón, Dirk G De Rooij, Ihsan Dereli, Attila Tóth, José Luis Barbero, et al. C14orf39/six6os1 is a constituent of the synaptonemal complex and is essential for mouse fertility. *Nature communications*, 7:13298, 2016.

[103] Li Yuan, Jeanette Pelttari, Eva Brundell, Birgitta Björkroth, Jian Zhao, Jian-Guo Liu, Hjalmar Brismar, Bertil Daneholt, and Christer Höög. The synaptonemal complex protein scp3 can form multistranded, cross-striated fibers in vivo. *The Journal of cell biology*, 142(2):331–339, 1998.

[104] M Tarsounas, RE Pearlman, PJ Gasser, MS Park, and PB Moens. Protein-protein interactions in the synaptonemal complex. *Molecular biology of the cell*, 8(8):1405–1414, 1997.

[105] Fang Yang, Rabindranath De La Fuente, N Adrian Leu, Claudia Baumann, K John McLaughlin, and P Jeremy Wang. Mouse sycp2 is required for synaptonemal complex assembly and chromosomal synapsis during male meiosis. *The Journal of cell biology*, 173(4):497–507, 2006.

[106] Johanna Liinamaria Syrjänen, Luca Pellegrini, and Owen Richard Davies. A molecular model for the role of sycp3 in meiotic chromosome organisation. *Elife*, 3:e02963, 2014.

[107] Yuxuan Xiao, Daniel Pollack, Miriam Andrusier, Avi Levy, Myrasol Callaway, Edward Nieves, Prabhakara Reddi, and Margarita Vigodner. Identification of cell-specific targets of sumoylation during mouse spermatogenesis. *Reproduction*, 151(2):149–66, 2016.

[108] Li Yuan, Jian-Guo Liu, Jian Zhao, Eva Brundell, Bertil Daneholt, and Christer Höög. The murine scp3 gene is required for synaptonemal complex assembly, chromosome synapsis, and male fertility. *Molecular cell*, 5(1):73–83, 2000.

[109] Toshinobu Miyamoto, Shiga Hasuike, Leah Yogev, Maria R Maduro, Mutsuo Ishikawa,

Heiner Westphal, and Dolores J Lamb. Azoospermia in patients heterozygous for a mutation in sycp3. *The Lancet*, 362(9397):1714–1719, 2003.

[110] Jian-Guo Liu, Li Yuan, Eva Brundell, Birgitta Björkroth, Bertil Daneholt, and Christer Höög. Localization of the n-terminus of scp1 to the central element of the synaptonemal complex and evidence for direct interactions between the n-termini of scp1 molecules organized head-to-head. *Experimental cell research*, 226(1):11–19, 1996.

[111] K Schmekel, RLJ Meuwissen, AJJ Dietrich, ACG Vink, J Van Marle, H Van Veen, and C Heyting. Organization of scp1 protein molecules within synaptonemal complexes of the rat. *Experimental cell research*, 226(1):20–30, 1996.

[112] Rupert Ollinger, Manfred Alsheimer, and Ricardo Benavente. Mammalian protein scp1 forms synaptonemal complex-like structures in the absence of meiotic chromosomes. *Molecular biology of the cell*, 16(1):212–217, 2005.

[113] James M Dunce, Orla M Dunne, Matthew Ratcliff, Claudia Millan, Suzanne Madgwick, Isabel Uson, and Owen R Davies. Structural basis of meiotic chromosome synapsis through sycp1 self-assembly. *Nature structural & molecular biology*, 25(7):557–569, 2018.

[114] Karoline Winkel, Manfred Alsheimer, Rupert Öllinger, and Ricardo Benavente. Protein sycp2 provides a link between transverse filaments and lateral elements of mammalian synaptonemal complexes. *Chromosoma*, 118(2):259–267, 2009.

[115] Femke AT de Vries, Esther de Boer, Mike van den Bosch, Willy M Baarends, Marja Ooms, Li Yuan, Jian-Guo Liu, Albert A van Zeeland, Christa Heyting, and Albert Pastink. Mouse sycp1 functions in synaptonemal complex assembly, meiotic recombination, and xy body formation. *Genes & development*, 19(11):1376–1389, 2005.

[116] Johanna Fraune, Sabine Schramm, Manfred Alsheimer, and Ricardo Benavente. The mammalian synaptonemal complex: protein components, assembly and role in meiotic recombination. *Experimental cell research*, 318(12):1340–1346, 2012.

[117] Karen Voelkel-Meiman, Sarah S Moustafa, Philippe Lefrançois, Anne M Villeneuve, and Amy J MacQueen. Full-length synaptonemal complex grows continuously during meiotic prophase in budding yeast. *PLoS genetics*, 8(10), 2012.

[118] Aaron Kershner, Sarah L Crittenden, Kyle Friend, Erika B Sorensen, Douglas F Porter, and Judith Kimble. Germline stem cells and their regulation in the nematode caenorhabditis elegans. In *Transcriptional and Translational Regulation of Stem Cells*, pages 29–46. Springer, 2013.

[119] Saul M Honigberg and Kedar Purnapatre. Signal pathway integration in the switch from the mitotic cell cycle to meiosis in yeast. *Journal of cell science*, 116(11):2137–2147, 2003.

[120] Christopher Merritt and Geraldine Seydoux. The puf rna-binding proteins fbf-1 and fbf-2 inhibit the expression of synaptonemal complex proteins in germline stem cells. *Development*, 137(11):1787–1798, 2010.

[121] Jasvinder S Ahuja, Rima Sandhu, Rana Mainpal, Crystal Lawson, Hanna Henley, Patricia A Hunt, Judith L Yanowitz, and G Valentin Börner. Control of meiotic pairing and recombination by chromosomally tethered 26s proteasome. *Science*, 355(6323):408–411, 2017.

[122] HBD Prasada Rao, Huanyu Qiao, Shubhang K Bhatt, Logan RJ Bailey, Hung D Tran, Sarah L Bourne, Wendy Qiu, Anusha Deshpande, Ajay N Sharma, Connor J Beebout, et al. A sumo-ubiquitin relay recruits proteasomes to chromosome axes to regulate meiotic recombination. *Science*, 355(6323):403–407, 2017.

[123] Aya Sato, Berith Isaac, Carolyn M Phillips, Regina Rillo, Peter M Carlton, David J Wynne, Roshni A Kasad, and Abby F Dernburg. Cytoskeletal forces span the nuclear envelope to coordinate meiotic chromosome pairing and synapsis. *Cell*, 139(5):907–919, 2009.

[124] Nicolas Christophorou, Thomas Rubin, Isabelle Bonnet, Tristan Piolot, Marion Arnaud, and Jean-René Huynh. Microtubule-driven nuclear rotations promote meiotic chromosome dynamics. *Nature cell biology*, 17(11):1388–1400, 2015.

[125] T. H. E. Meuwissen, B. J. Hayes, and M. E. Goddard. Prediction of total genetic value using genome-wide dense marker maps. *Genetics*, 157(4):1819–1829, 2001.

[126] Philip W Jordan, Jesse Karppinen, and Mary A Handel. Polo-like kinase is required for synaptonemal complex disassembly and phosphorylation in mouse spermatocytes. *J Cell Sci*, 125(21):5061–5072, 2012.

[127] Katharina Schücker, Thorge Holm, Christian Franke, Markus Sauer, and Ricardo Benavente. Elucidation of synaptonemal complex organization by super-resolution imaging with isotropic resolution. *Proceedings of the National Academy of Sciences*, 112(7):2029–2033, 2015.

[128] Abrahan Hernández-Hernández, Sergej Masich, Tomoyuki Fukuda, Anna Kouznetsova, Sara Sandin, Bertil Daneholt, and Christer Höög. The central element of the synaptonemal complex in mice is organized as a bilayered junction structure. *J Cell Sci*, 129(11):2239–2249, 2016.

[129] Karin Schmekel, Jacob Wahrman, Ulf Skoglund, and Bertil Daneholt. The central region of the synaptonemal complex inblaps cribrosa studied by electron microscope tomography. *Chromosoma*, 102(10):669–681, 1993.

[130] Karin Schmekel, Ulf Skoglund, and Bertil Daneholt. The three-dimensional structure

of the central region in a synaptonemal complex: a comparison between rat and two insect species, drosophila melanogaster andblaps cribrosa. *Chromosoma*, 102(10):682–692, 1993.

[131] Ya-Hui Chi, Lily I Cheng, Tim Myers, Jerrold M Ward, Elizabeth Williams, Qin Su, Larry Faucette, Jing-Ya Wang, and Kuan-Teh Jeang. Requirement for sun1 in the expression of meiotic reproductive genes and pirna. *Development*, 136(6):965–973, 2009.

[132] Elisabeth Pasch, Jana Link, Carolin Beck, Stefanie Scheuerle, and Manfred Alsheimer. The linc complex component sun4 plays a crucial role in sperm head formation and fertility. *Biology open*, 4(12):1792–1802, 2015.

[133] Esther de Boer, Franck GP Lhuissier, and Christa Heyting. Cytological analysis of interference in mouse meiosis. In *Meiosis*, pages 355–382. Springer, 2009.

[134] Fei Chen, Paul W Tillberg, and Edward S Boyden. Expansion microscopy. *Science*, 347(6221):543–548, 2015.

[135] David N Mastronarde. Automated electron microscope tomography using robust prediction of specimen movements. *Journal of structural biology*, 152(1):36–51, 2005.

[136] A Leygue. Plane fit. `https://de.mathworks.com/matlabcentral/fileexchange/43305-plane-ft`, 2014. Last accessed: 30.08.2019. (2014).

[137] Marie-Christin Spindler, Frederik Helmprobst, Christian Stigloher, and Ricardo Benavente. Em tomography of meiotic linc complexes. In *Methods in molecular biology*, pages 3–15. Springer, 2018.

[138] Lonnie D Russell, Robert A Ettlin, Amiya P Sinha Hikim, and Eric D Clegg. Histological and histopathological evaluation of the testis. *International journal of andrology*, 16(1):83–83, 1993.

[139] Christian Stigloher, Hong Zhan, Mei Zhen, Janet Richmond, and Jean-Louis Bessereau. The presynaptic dense projection of the caenorhabiditis elegans cholinergic neuromuscular junction localizes synaptic vesicles at the active zone through syd-2/liprin and unc-10/rim-dependent interactions. *Journal of Neuroscience*, 31(12):4388–4396, 2011.

[140] Robby M Weimer. Preservation of c. elegans tissue via high-pressure freezing and freeze-substitution for ultrastructural analysis and immunocytochemistry. In *C. elegans*, pages 203–221. Springer, 2006.

[141] Sebastian M Markert, Vivien Bauer, Thomas S Muenz, Nicola G Jones, Frederik Helmprobst, Sebastian Britz, Markus Sauer, Wolfgang Rössler, Markus Engstler, and Christian Stigloher. 3d subcellular localization with superresolution array tomography on ultrathin sections of various species. In *Methods in cell biology*, volume 140, pages 21–47. Elsevier, 2017.

[142] Rasmani Hazra, Lisa Corcoran, Mat Robson, Kirsten J McTavish, Dannielle Upton, David J Handelsman, and Charles M Allan. Temporal role of sertoli cell androgen receptor expression in spermatogenic development. *Molecular Endocrinology*, 27(1):12–24, 2013.

[143] RR Tuck, BP Setchell, GMH Waites, and JA Young. The composition of fluid collected by micropuncture and catheterization from the seminiferous tubules and rete testis of rats. *Pflügers Archiv*, 318(3):225–243, 1970.

[144] Frederik Helmprobst, Miriam Frank, and Christian Stigloher. Presynaptic architecture of the larval zebrafish neuromuscular junction. *Journal of Comparative Neurology*, 523(13):1984–1997, 2015.

[145] Gina E Sosinsky, John Crum, Ying Z Jones, Jason Lanman, Benjamin Smarr, Masako Terada, Maryann E Martone, Thomas J Deerinck, John E Johnson, and Mark H Ellisman. The combination of chemical fixation procedures with high pressure freezing and freeze substitution preserves highly labile tissue ultrastructure for electron tomography applications. *Journal of structural biology*, 161(3):359–371, 2008.

[146] Tin Ki Tsang, Eric A Bushong, Daniela Boassa, Junru Hu, Benedetto Romoli, Sebastien Phan, Davide Dulcis, Chih-Ying Su, and Mark H Ellisman. High-quality ultrastructural preservation using cryofixation for 3d electron microscopy of genetically labeled tissues. *Elife*, 7, 2018.

[147] Nagaraju Dhanyasi, Dagan Segal, Eyal Shimoni, Vera Shinder, Ben-Zion Shilo, K VijayRaghavan, and Eyal D Schejter. Surface apposition and multiple cell contacts promote myoblast fusion in drosophila flight muscles. *Journal of Cell Biology*, 211(1):191–203, 2015.

[148] Kristin Verena Kaltdorf, Maria Theiss, Sebastian Matthias Markert, Mei Zhen, Thomas Dandekar, Christian Stigloher, and Philip Kollmannsberger. Automated classification of synaptic vesicles in electron tomograms of c. elegans using machine learning. *PloS one*, 13(10):e0205348, 2018.

[149] Rui Yan, Singanallur V Venkatakrishnan, Jun Liu, Charles A Bouman, and Wen Jiang. Mbir: A cryo-et 3d reconstruction method that effectively minimizes missing wedge artifacts and restores missing information. *Journal of structural biology*, 206(2):183–192, 2019.

[150] Kazuhiro Aoyama, Tomoko Takagi, Ai Hirase, and Atsuo Miyazawa. Stem tomography for thick biological specimens. *Ultramicroscopy*, 109(1):70–80, 2008.

[151] Ewelina Bolcun-Filas and Mary Ann Handel. Meiosis: the chromosomal foundation of reproduction. *Biology of reproduction*, 99(1):112–126, 2018.

[152] Li Yuan, Jian-Guo Liu, Mary-Rose Hoja, Johannes Wilbertz, Katarina Nordqvist, and Christer Höög. Female germ cell aneuploidy and embryo death in mice lacking the meiosis-specific protein scp3. *Science*, 296(5570):1115–1118, 2002.

[153] Ewelina Bolcun-Filas, Yael Costa, Robert Speed, Mary Taggart, Ricardo Benavente, Dirk G De Rooij, and Howard J Cooke. Syce2 is required for synaptonemal complex assembly, double strand break repair, and homologous recombination. *The Journal of cell biology*, 176(6):741–747, 2007.

[154] Hong Wang and Christer Höög. Structural damage to meiotic chromosomes impairs dna recombination and checkpoint control in mammalian oocytes. *The Journal of cell biology*, 173(4):485–495, 2006.

[155] Montrose J Moses. Synaptinemal complex. *Annual review of genetics*, 2(1):363–412, 1968.

[156] JR Sotelo. Ultrastructure of the chromosomes at meiosis. *Handbook of molecular cytology (A. Lima-de-Faria, ed.)*, pages 412–434, 1969.

[157] M Westergaard and D Von Wettstein. The synaptinemal complex. *Annual review of genetics*, 6(1):71–110, 1972.

[158] Karin Schmekel and Bertil Daneholt. The central region of the synaptonemal complex revealed in three dimensions. *Trends in cell biology*, 5(6):239–242, 1995.

[159] Peter B Møens and Ronald E Pearlman. Chromatin organization at meiosis. *Bioessays*, 9(5):151–153, 1988.

[160] Melanie J Dobson, Ronald E Pearlman, Angelo Karaiskakis, Barbara Spyropoulos, and Peter B Moens. Synaptonemal complex proteins: occurrence, epitope mapping and chromosome disjunction. *Journal of cell science*, 107(10):2749–2760, 1994.

[161] JH Lammers, HH Offenberg, M Van Aalderen, AC Vink, AJ Dietrich, and C Heyting. The gene encoding a major component of the lateral elements of synaptonemal complexes of the rat is related to x-linked lymphocyte-regulated genes. *Molecular and cellular biology*, 14(2):1137–1146, 1994.

[162] P Jeremy Wang, John R McCarrey, Fang Yang, and David C Page. An abundance of x-linked genes expressed in spermatogonia. *Nature genetics*, 27(4):422, 2001.

[163] Cori K Cahoon, Zulin Yu, Yongfu Wang, Fengli Guo, Jay R Unruh, Brian D Slaughter, and R Scott Hawley. Superresolution expansion microscopy reveals the three-dimensional organization of the drosophila synaptonemal complex. *Proceedings of the National Academy of Sciences*, 114(33):E6857–E6866, 2017.

[164] Fabian U Zwettler, Marie-Christin Spindler, Sebastian Reinhard, Teresa Klein, Andreas Kurz, Ricardo Benavente, and Markus Sauer. Tracking down the molecular architec-

ture of the synaptonemal complex by expansion microscopy. *Nature Communications*, 11(1):1–11, 2020.

[165] Alberto J Solari and Montrose J Moses. The structure of the central region in the synaptonemal complexes of hamster and cricket spermatocytes. *The Journal of cell biology*, 56(1):145–152, 1973.

[166] Davide Gambarotto, Fabian U Zwettler, Maeva Le Guennec, Marketa Schmidt-Cernohorska, Denis Fortun, Susanne Borgers, Jörn Heine, Jan-Gero Schloetel, Matthias Reuss, Michael Unser, et al. Imaging cellular ultrastructures using expansion microscopy (u-exm). *Nature methods*, 16(1):71, 2019.

[167] Paul W Tillberg, Fei Chen, Kiryl D Piatkevich, Yongxin Zhao, Chih-Chieh Jay Yu, Brian P English, Linyi Gao, Anthony Martorell, Ho-Jun Suk, Fumiaki Yoshida, et al. Protein-retention expansion microscopy of cells and tissues labeled using standard fluorescent proteins and antibodies. *Nature biotechnology*, 34(9):987–992, 2016.

[168] Rosario Ortiz, Anna Kouznetsova, Olga M Echeverría-Martínez, Gerardo H Vázquez-Nin, and Abrahan Hernández-Hernández. The width of the lateral element of the synaptonemal complex is determined by a multilayered organization of its components. *Experimental cell research*, 344(1):22–29, 2016.

[169] Klaus Weber, Peter C Rathke, and Mary Osborn. Cytoplasmic microtubular images in glutaraldehyde-fixed tissue culture cells by electron microscopy and by immunofluorescence microscopy. *Proceedings of the National Academy of Sciences*, 75(4):1820–1824, 1978.

[170] Fabian U Zwettler, Sebastian Reinhard, Davide Gambarotto, Toby DM Bell, Virginie Hamel, Paul Guichard, and Markus Sauer. Molecular resolution imaging by post-labeling expansion single molecule localization microscopy (ex-smlm). *bioRxiv*, 2020.

[171] BR Nebel and EM Coulon. The fine structure of chromosomes in pigeon spermatocytes. *Chromosoma*, 13(3):272–291, 1962.

[172] DE Comings and TA Okada. Fine structure of the synaptonemal complex: Regular and stereo electron microscopy of deoxyribonuclease-treated whole mount preparations. *Experimental cell research*, 65(1):104–116, 1971.

[173] SJ Counce and GF Meyer. Differentiation of the synaptonemal complex and the kinetochore in locusta spermatocytes studied by whole mount electron microscopy. *Chromosoma*, 44(2):231–253, 1973.

[174] M Eetal Dresser and MJ Moses. Synaptonemal complex karyotyping in spermatocytes of the chinese hamster (cricetulus griseus). *Chromosoma*, 76(1):1–22, 1980.

[175] J Wahrman. Synaptonemal complexes-origin and fate. *Chromosomes today*, 7:105–113, 1981.

[176] C Heyting, AJ Dietrich, EJW Redeker, and AC Vink. Structure and composition of synaptonemal complexes, isolated from rat spermatocytes. *European journal of cell biology*, 36(2):307–314, 1985.

[177] J Del Mazo and LG Gil-Alberdi. Multistranded organization of the lateral elements of the synaptonemal complex in the rat and mouse. *Cytogenetic and Genome Research*, 41(4):219–224, 1986.

[178] MJ Franco, RB Sciurano, and AJ Solari. Protein immunolocalization supports the presence of identical mechanisms of xy body formation in eutherians and marsupials. *Chromosome research*, 15(6):815–824, 2007.

[179] Alberto J Solari. *Sex chromosomes and sex determination in vertebrates*. CRC Press, 1993.

[180] Roberta B Sciurano, Geraldine De Luca, I Mónica Rahn, and Alberto J Solari. The xy body of the cat (felis catus): Structural differentiations and protein immunolocalization. *Cytogenetic and genome research*, 152(3):137–147, 2017.

[181] Huizhong Xu, Zhisong Tong, Qing Ye, Tengqian Sun, Zhenmin Hong, Lunfeng Zhang, Alexandra Bortnick, Sunglim Cho, Paolo Beuzer, Joshua Axelrod, et al. Molecular organization of mammalian meiotic chromosome axis revealed by expansion storm microscopy. *Proceedings of the National Academy of Sciences*, 116(37):18423–18428, 2019.

[182] Sebastian Van de Linde, Anna Löschberger, Teresa Klein, Meike Heidbreder, Steve Wolter, Mike Heilemann, and Markus Sauer. Direct stochastic optical reconstruction microscopy with standard fluorescent probes. *Nature protocols*, 6(7):991, 2011.

[183] Graham T Dempsey, Joshua C Vaughan, Kok Hao Chen, Mark Bates, and Xiaowei Zhuang. Evaluation of fluorophores for optimal performance in localization-based super-resolution imaging. *Nature methods*, 8(12):1027, 2011.

[184] D Von Wettstein. The synaptinemal complex and four-strand crossing over. *Proceedings of the National Academy of Sciences*, 68(4):851–855, 1971.

[185] Alan MV West, Scott C Rosenberg, Sarah N Ur, Madison K Lehmer, Qiaozhen Ye, Götz Hagemann, Iracema Caballero, Isabel Uson, Amy J MacQueen, Franz Herzog, et al. A conserved filamentous assembly underlies the structure of the meiotic chromosome axis. *Elife*, 8:e40372, 2019.

[186] Lisa J Harris, Eileen Skaletsky, and Alexander McPherson. Crystallographic structure of an intact igg1 monoclonal antibody. *Journal of molecular biology*, 275(5):861–872, 1998.

[187] Jacomine Krijnse Locker and Sandra L Schmid. Integrated electron microscopy: super-duper resolution. *PLoS Biol*, 11(8):e1001639, 2013.

[188] Kenneth H Roux. Immunoglobulin structure and function as revealed by electron microscopy. *International archives of allergy and immunology*, 120(2):85–99, 1999.

[189] Elmar Wolf, Berthold Kastner, and Reinhard Lührmann. Antisense-targeted immuno-em localization of the pre-mrna path in the spliceosomal c complex. *rna*, 18(7):1347–1357, 2012.

[190] Harry Scherthan, Susanne Weich, Herbert Schwegler, Christa Heyting, Michael Härle, and Thomas Cremer. Centromere and telomere movements during early meiotic prophase of mouse and man are associated with the onset of chromosome pairing. *The Journal of Cell Biology*, 134(5):1109–1125, 1996.

[191] Li Yuan, Jian-Guo Liu, Jian Zhao, Eva Brundell, Bertil Daneholt, and Christer Höög. The murine scp3 gene is required for synaptonemal complex assembly, chromosome synapsis, and male fertility. *Molecular cell*, 5(1):73–83, 2000.

[192] JH Tepperberg, MJ Moses, and J Nath. Colchicine effects on meiosis in the male mouse. *Chromosoma*, 106(3):183–192, 1997.

[193] JH Tepperberg, MJ Moses, and J Nath. Colchicine effects on meiosis in the male mouse: Ii. inhibition of synapsis and induction of nondisjunction. *Mutation Research/Fundamental and Molecular Mechanisms of Mutagenesis*, 429(1):93–105, 1999.

[194] Xu Ding, Rener Xu, Juehua Yu, Tian Xu, Yuan Zhuang, and Min Han. Sun1 is required for telomere attachment to nuclear envelope and gametogenesis in mice. *Developmental cell*, 12(6):863–872, 2007.

[195] Daniel A Starr and Min Han. Anchors away: an actin based mechanism of nuclear positioning. *Journal of cell science*, 116(2):211–216, 2003.

[196] Daniel A Starr. A nuclear-envelope bridge positions nuclei and moves chromosomes. *Journal of cell science*, 122(5):577–586, 2009.

[197] Charles W Wolgemuth and Sean X Sun. Elasticity of $\alpha$-helical coiled coils. *Physical review letters*, 97(24):248101, 2006.

[198] Paul T Arsenovic, Iswarya Ramachandran, Kranthidhar Bathula, Ruijun Zhu, Jiten D Narang, Natalie A Noll, Christopher A Lemmon, Gregg G Gundersen, and Daniel E Conway. Nesprin-2g, a component of the nuclear linc complex, is subject to myosin-dependent tension. *Biophysical journal*, 110(1):34–43, 2016.

[199] Miki Hieda. Implications for diverse functions of the linc complexes based on the structure. *Cells*, 6(1):3, 2017.

[200] Eva Göb, Johannes Schmitt, Ricardo Benavente, and Manfred Alsheimer. Mammalian

sperm head formation involves different polarization of two novel linc complexes. *PloS one*, 5(8), 2010.

[201] Danielle A Grotjahn and Gabriel C Lander. Setting the dynein motor in motion: New insights from electron tomography. *Journal of Biological Chemistry*, 294(36):13202–13217, 2019.

[202] Danielle A Grotjahn, Saikat Chowdhury, Yiru Xu, Richard J McKenney, Trina A Schroer, and Gabriel C Lander. Cryo-electron tomography reveals that dynactin recruits a team of dyneins for processive motility. *Nature structural & molecular biology*, 25(3):203–207, 2018.

[203] Aristidis Likas, Nikos Vlassis, and Jakob J Verbeek. The global k-means clustering algorithm. *Pattern recognition*, 36(2):451–461, 2003.

[204] Saikat Chowdhury, Stephanie A Ketcham, Trina A Schroer, and Gabriel C Lander. Structural organization of the dynein–dynactin complex bound to microtubules. *Nature structural & molecular biology*, 22(4):345–347, 2015.

[205] Vladislav Belyy, Max A Schlager, Helen Foster, Armando E Reimer, Andrew P Carter, and Ahmet Yildiz. The mammalian dynein–dynactin complex is a strong opponent to kinesin in a tug-of-war competition. *Nature cell biology*, 18(9):1018–1024, 2016.

[206] Daniël Splinter, David S Razafsky, Max A Schlager, Andrea Serra-Marques, Ilya Grigoriev, Jeroen Demmers, Nanda Keijzer, Kai Jiang, Ina Poser, Anthony A Hyman, et al. Bicd2, dynactin, and lis1 cooperate in regulating dynein recruitment to cellular structures. *Molecular biology of the cell*, 23(21):4226–4241, 2012.

[207] Max A Schlager, Ha Thi Hoang, Linas Urnavicius, Simon L Bullock, and Andrew P Carter. In vitro reconstitution of a highly processive recombinant human dynein complex. *The EMBO journal*, 33(17):1855–1868, 2014.

[208] Kai Zhang, Helen E Foster, Arnaud Rondelet, Samuel E Lacey, Nadia Bahi-Buisson, Alexander W Bird, and Andrew P Carter. Cryo-em reveals how human cytoplasmic dynein is auto-inhibited and activated. *Cell*, 169(7):1303–1314, 2017.

[209] Richard J McKenney, Walter Huynh, Marvin E Tanenbaum, Gira Bhabha, and Ronald D Vale. Activation of cytoplasmic dynein motility by dynactin-cargo adapter complexes. *Science*, 345(6194):337–341, 2014.

[210] Linas Urnavicius, Kai Zhang, Aristides G Diamant, Carina Motz, Max A Schlager, Minmin Yu, Nisha A Patel, Carol V Robinson, and Andrew P Carter. The structure of the dynactin complex and its interaction with dynein. *Science*, 347(6229):1441–1446, 2015.

[211] Linas Urnavicius, Clinton K Lau, Mohamed M Elshenawy, Edgar Morales-Rios, Carina

Motz, Ahmet Yildiz, and Andrew P Carter. Cryo-em shows how dynactin recruits two dyneins for faster movement. *Nature*, 554(7691):202–206, 2018.

[212] Anna Salter. *Investigating the Interaction between the Nuclear Envelope Protein KASH5 and Dynein*. PhD thesis, The University of Manchester (United Kingdom), 2017.

[213] Andrea Enguita-Marruedo, Wiggert A Van Cappellen, Jos W Hoogerbrugge, Fabrizia Carofiglio, Evelyne Wassenaar, Johan A Slotman, Adriaan Houtsmuller, and Willy M Baarends. Live cell analyses of synaptonemal complex dynamics and chromosome movements in cultured mouse testis tubules and embryonic ovaries. *Chromosoma*, 127(3):341–359, 2018.

[214] Sagardip Majumder, Patrick T Willey, Maxwell S DeNies, Allen P Liu, and GW Gant Luxton. A synthetic biology platform for the reconstitution and mechanistic dissection of linc complex assembly. *J Cell Sci*, 132(4):jcs219451, 2019.

[215] Juanjuan Long, Chenhui Huang, Yanyan Chen, Ying Zhang, Shaohua Shi, Ligang Wu, Yie Liu, Chengyu Liu, Jian Wu, and Ming Lei. Telomeric terb1–trf1 interaction is crucial for male meiosis. *Nature structural & molecular biology*, 24(12):1073, 2017.

[216] James M Dunce, Amy E Milburn, Manickam Gurusaran, Irene da Cruz, Lee T Sen, Ricardo Benavente, and Owen R Davies. Structural basis of meiotic telomere attachment to the nuclear envelope by majin-terb2-terb1. *Nature communications*, 9(1):1–18, 2018.

[217] Peter M Carlton. Application of advanced fluorescence microscopy to the structure of meiotic chromosomes. *Biophysical reviews*, 5(4):313–322, 2013.

[218] Aimee J Marko, Simon S Smith, Eric D Siggia, Juan C Bustamante, and James Mussell. Entropic elasticity of lambda-phage dna. *Science (New York, NY)*, 1994.

[219] Matthias Rief, Mathias Gautel, Filipp Oesterhelt, Julio M Fernandez, and Hermann E Gaub. Reversible unfolding of individual titin immunoglobulin domains by afm. *science*, 276(5315):1109–1112, 1997.

[220] Guillaume Stirnemann, David Giganti, Julio M Fernandez, and BJ Berne. Elasticity, structure, and relaxation of extended proteins under force. *Proceedings of the National Academy of Sciences*, 110(10):3847–3852, 2013.

# Publication list

Parts of this work were published in the following peer-reviewed journal articles:

Zwettler, F. U.*, **Spindler, M. C.***, Reinhard, S., Klein, T., Kurz, A., Benavente, R., & Sauer, M. (2020). Tracking down the molecular architecture of the synaptonemal complex by expansion microscopy. *Nature Communications*, 11, 3222. ***Shared first-authors**

**Spindler, M. C.**, Redolfi, J., Helmprobst, F., Kollmannsberger, P., Stigloher, C., & Benavente, R. (2019). Electron tomography of mouse LINC complexes at meiotic telomere attachment sites with and without microtubules. *Communications biology*, 2, 376.

**Spindler, M. C.**, Filbeck, S., Stigloher, C., & Benavente, R. (2019). Quantitative basis of meiotic chromosome synapsis analyzed by electron tomography. *Scientific reports*, 9, 16102.

**Spindler, M. C.**, Helmprobst, F., Stigloher, C., & Benavente, R. (2018). EM Tomography of Meiotic LINC Complexes. *Methods in molecular biology*, 1840, 3-15.

Other peer-reviewed journal articles:

Glogger, M., Stichler, S., Subota, I., Bertlein, S., **Spindler, M. C.**, Teßmar, J., Groll, J., Engstler, M., & Fenz, S. F. (2017). Live-cell super-resolution imaging of intrinsically fast moving flagellates. *Journal of Physics D: Applied Physics*, 50(7), 074004.

# Acknowledgements

# Eidesstattliche Erklärung

Hiermit erkläre ich an Eides statt, die Dissertation: "Molecular architecture of meiotic multiprotein complexes", eigenständig, d.h. insbesondere selbständig und ohne Hilfe eines kommerziellen Promotionsberaters, angefertigt und keine anderen, als die von mir angegebenen Quellen und Hilfsmittel verwendet zu haben.

Ich erkläre außerdem, dass die Dissertation weder in gleicher noch in ähnlicher Form bereits in einem anderen Prüfungsverfahren vorgelegen hat.

Weiterhin erkläre ich, dass bei allen Abbildungen und Texten bei denen die Verwertungsrechte nicht bei mir liegen, diese von den Rechtsinhabern eingeholt wurden und die Textstellen bzw. Abbildungen entsprechend den rechtlichen Vorgaben gekennzeichnet sind sowie bei Abbbildungen, die dem Internet entnommen wurden, der entsprechende Hypertextlink angegeben wurde.

Datum: _____ Unterschrift _____

# Affidavit

I hereby declare that my thesis entitled: "Molecular architecture of meiotic multiprotein complexes" is the result of my own work. I did not receive any help or support from commercial consultants. All sources and / or materials applied are listed and specified in the thesis.

Furthermore I verify that the thesis has not been submitted as part of another examination process neither in identical nor in similar form.

Besides I declare that if I do not hold the copyright for figures and paragraphs, I obtained it from the rights holder and that paragraphs and figures have been marked accordingly to law or for figures taken from the internet the hyperlink has been added accordingly.

Date: _____ Signature _____